Article

Targeting thalamic circuits rescues motor and mood deficits in PD mice

https://doi.org/10.1038/s41586-022-04806-x

Received: 18 March 2021

Accepted: 26 April 2022

Published online: 08 June 2022

Check for updates

Ying Zhang[1,10]✉, Dheeraj S. Roy[2,10]✉, Yi Zhu[3], Yefei Chen[4,5], Tomomi Aida[1], Yuanyuan Hou[1], Chenjie Shen[1], Nicholas E. Lea[1], Margaret E. Schroeder[1], Keith M. Skaggs[1], Heather A. Sullivan[1], Kyle B. Fischer[6,7], Edward M. Callaway[6,7], Ian R. Wickersham[1], Ji Dai[4,5], Xiao-Ming Li[3,8,9], Zhonghua Lu[4,5] & Guoping Feng[1,2]✉

Although bradykinesia, tremor and rigidity are the hallmark motor defects in patients with Parkinson's disease (PD), patients also experience motor learning impairments and non-motor symptoms such as depression[1]. The neural circuit basis for these different symptoms of PD are not well understood. Although current treatments are effective for locomotion deficits in PD[2,3], therapeutic strategies targeting motor learning deficits and non-motor symptoms are lacking[4–6]. Here we found that distinct parafascicular (PF) thalamic subpopulations project to caudate putamen (CPu), subthalamic nucleus (STN) and nucleus accumbens (NAc). Whereas PF→CPu and PF→STN circuits are critical for locomotion and motor learning, respectively, inhibition of the PF→NAc circuit induced a depression-like state. Whereas chemogenetically manipulating CPu-projecting PF neurons led to a long-term restoration of locomotion, optogenetic long-term potentiation (LTP) at PF→STN synapses restored motor learning behaviour in an acute mouse model of PD. Furthermore, activation of NAc-projecting PF neurons rescued depression-like phenotypes. Further, we identified nicotinic acetylcholine receptors capable of modulating PF circuits to rescue different PD phenotypes. Thus, targeting PF thalamic circuits may be an effective strategy for treating motor and non-motor deficits in PD.

PD is a neurodegenerative disorder characterized by the loss of dopamine neurons from substantia nigra pars compacta (SNc), abnormal activity in the basal ganglia network and severe motor dysfunction[1]. PD motor symptoms such as rigor, tremor and bradykinesia are treated by levodopa administration[2] or high-frequency deep brain stimulation (DBS) targeting the STN region[3]. Patients with PD also have motor learning impairments, specifically slower learning rates and retention deficits[4], which cannot be treated effectively[5]. In addition to motor symptoms, patients commonly experience debilitating non-motor phenotypes, including depression and anxiety[6], which have received limited attention. Identifying neural circuit mechanisms responsible for both motor and non-motor deficits in PD could lead to the development of novel therapeutic approaches. PF has extensive connectivity with the basal ganglia[7,8], critically contributes to motor behaviours[9,10], and PF DBS can modulate pathophysiological changes relevant to PD[11]. On the basis of these observations and the fact that PF thalamus projects to NAc[12]—a key structure involved in reward processing and depression-like behaviours[13]—we systematically investigated the connectivity and function of PF inputs to basal ganglia nuclei as well as their relevance to motor and non-motor phenotypes using male mice in a mouse model of PD.

Distinct subpopulations in PF thalamus

PF sends major projections to dorsal striatum (that is, CPu), STN and ventral striatum[12,14–16] (that is, NAc). The physiological properties of these PF subpopulations and their circuits have not been extensively examined. We used both anterograde (Extended Data Fig. 1a,b) and retrograde (Extended Data Fig. 1c–f) tracing to confirm these three major projections. We found that retrograde cholera toxin subunit B (CTB)-labelled CPu- or STN-projecting PF neurons (PF_{CPu} or PF_{STN}, respectively) were intermingled in lateral PF, whereas NAc-projecting PF neurons (PF_{NAc}) were localized to medial PF (Fig. 1a). To determine whether the different PF subpopulations, in particular PF_{CPu} and PF_{STN} neurons, were part of the same ensemble or represent distinct ensembles, we performed triple retrograde CTB tracing. Notably, there was minimal overlap between the three PF populations (Fig. 1b and Extended Data Fig. 1g–k).

[1]McGovern Institute for Brain Research, Department of Brain and Cognitive Sciences, Massachusetts Institute of Technology, Cambridge, MA, USA. [2]Stanley Center for Psychiatric Research, Broad Institute of MIT and Harvard, Cambridge, MA, USA. [3]Center for Neuroscience and Department of Neurology of Second Affiliated Hospital, Zhejiang University School of Medicine, Hangzhou, China. [4]Shenzhen Key Laboratory for Molecular Biology of Neural Development, The Brain Cognition and Brain Disease Institute, Shenzhen Institutes of Advanced Technology, Chinese Academy of Sciences, Shenzhen, China. [5]Shenzhen–Hong Kong Institute of Brain Science, Shenzhen, China. [6]Systems Neurobiology Laboratories, Salk Institute for Biological Studies, La Jolla, CA, USA. [7]Department of Neurosciences, University of California San Diego, La Jolla, CA, USA. [8]NHC and CAMS Key Laboratory of Medical Neurobiology, Center for Brain Science and Brain-Inspired Intelligence, Guangdong–Hong Kong–Macao Greater Bay Area, Zhejiang University, Hangzhou, China. [9]Joint Institute for Genetics and Genome Medicine between Zhejiang University and University of Toronto, Zhejiang University, Hangzhou, China. [10]These authors contributed equally: Ying Zhang, Dheeraj S. Roy. ✉e-mail: zhangyin@mit.edu; droy@broadinstitute.org; fengg@mit.edu

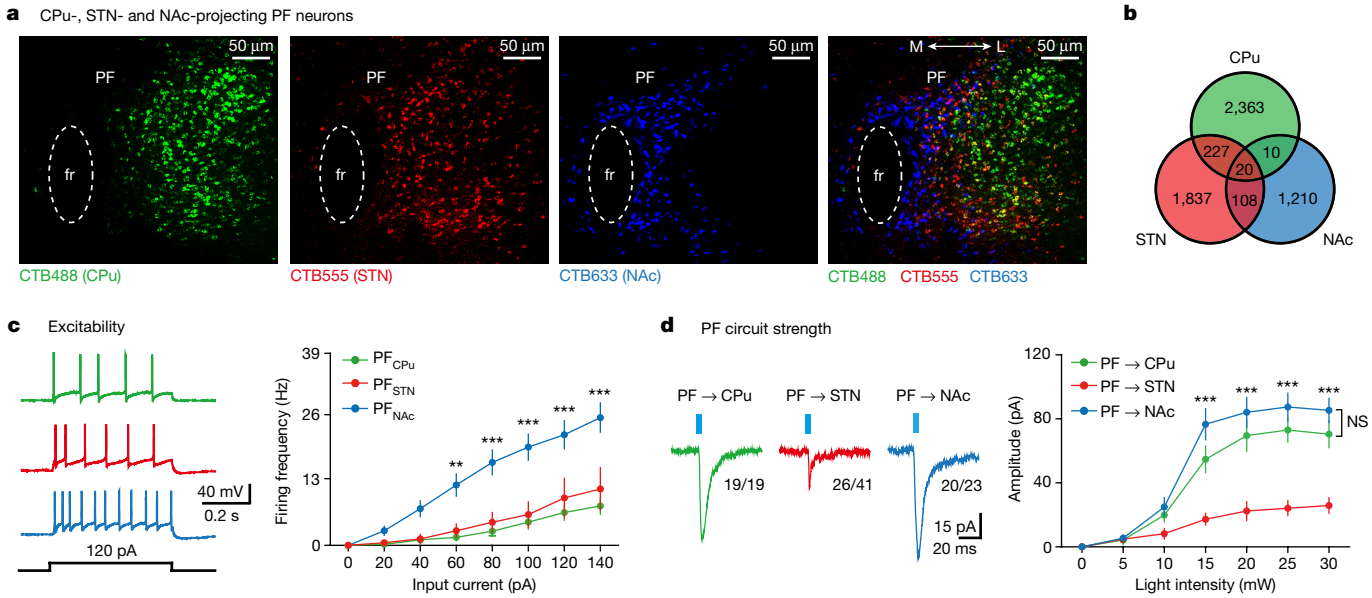

Fig. 1 | Three distinct projection-specific subpopulations in PF thalamus. **a**, Retrograde labelling of PF by injecting CTB into CPu, STN, or NAc. M, medial; L, lateral; fr, fasciculus retroflexus. **b**, A Venn diagram reflecting the overlap between CPu-, STN- and NAc-projecting PF neurons ($n = 4$ mice); 0.35% of all retrogradely-labelled cells in PF send collaterals to the three downstream targets. **c**, Representative traces (left) and ex vivo current frequency recordings (right) of PF_{CPu}, PF_{NAc} and PF_{STN} neurons, which were labelled using retrograde rabies virus (RV) injected into CPu, NAc or STN, respectively (PF_{CPu}: $n = 19$ neurons (5, 7 and 7 from 3 mice); PF_{STN}: $n = 15$ neurons (6, 5 and 4 from 3 mice); PF_{NAc}: $n = 17$ neurons (6, 7 and 4 from 3 mice)). **d**, ChR2-eYFP virus was injected in PF and ex vivo recordings were performed from CPu, STN and NAc. Representative traces (left, 20 mW light intensity) and quantification (right) of evoked excitatory postsynaptic current (EPSC) amplitudes in response to graded light intensity stimulation (PF→CPu: $n = 15$ neurons (5, 5 and 5 from 3 mice); PF→STN: $n = 15$ neurons (4, 6 and 5 from 3 mice); PF→NAc: $n = 15$ neurons (5, 5 and 5 from 3 mice)). Data are mean ± s.e.m. Two-sided two-way ANOVA with repeated measures followed by Bonferroni post hoc test (**c**, **d**). $F = 12.87$, degrees of freedom in the numerator (DFn) = 2, degrees of freedom in the denominator (DFd) = 336, $P < 0.0001$ (**c**), $F = 31.54$, DFn = 2, DFd = 252, $P < 0.0001$ (**d**). In all figures, $^{*}P < 0.05$, $^{**}P < 0.01$ and $^{***}P < 0.001$. NS, not significant.

Ex vivo electrophysiological recordings from retrograde rabies virus[17] (dG–GFP)-labelled PF neurons exhibited similar basic electrophysiological properties between PF_{CPu} and PF_{STN} neurons, which were distinct from those of PF_{NAc} neurons (Fig. 1c and Extended Data Fig. 1l–p). Light-evoked currents were larger in the PF→CPu and PF→NAc circuits compared with PF→STN (Fig. 1d and Extended Data Figs. 1q–s and 2a–c) and these circuits had different short-term plasticities (Extended Data Fig. 2d). Weaker currents of the PF→STN circuit were not owing to a smaller ensemble size as compared with PF_{CPu} and PF_{NAc} neurons (Extended Data Fig. 1k) or any difference in the reliability across PF subpopulations (Extended Data Fig. 1r). These observations demonstrate that PF neurons projecting to CPu, STN and NAc are distinct subpopulations.

PF subpopulations mediate motor behaviour

We first examined the role of PF subpopulations projecting to motor structures (that is, CPu or STN). Using a retrograde rabies virus-based approach[18], we observed robust projection-specific labelling (Fig. 2a). Compound 21[19] (C21) reversibly inhibited PF neurons expressing a mutated human M4 muscarinic receptor (hM4Di) ex vivo (Extended Data Fig. 2e). Although inhibition of PF_{STN} neurons had no effect on locomotion, inhibition of PF_{CPu} neurons resulted in a significant increase in motor activity (22.81% increase in PF_{CPu} compared with mCherry controls) (Fig. 2b). The latter differs from a previous report[20] in which chemogenetics was used to inhibit the entire PF and which reported no significant change in behaviour, suggesting that projection-specific PF manipulations may be more effective at revealing specific behavioural contributions. We next examined whether these PF subpopulations are involved in motor learning using a rotarod assay[21]. Consistent with the open field, PF_{CPu}-inhibited mice had a longer latency to fall on day 1 of rotarod training compared with control mice and PF_{STN}-inhibited mice (Extended Data Fig. 2f). Nevertheless, mCherry and PF_{CPu}-inhibited mice showed significant enhancements in performance across days (30.36% and 17.75% increase in mCherry and PF_{CPu}, respectively) (Fig. 2c), indicating effective motor learning. Although PF_{STN} inhibited mice exhibited similar performance on day 1 to control mice (Extended Data Fig. 2f), they lacked a learning-induced increase in performance across days (4.46% increase) (Fig. 2c). We measured the strength of distinct PF circuits before and after rotarod (Extended Data Fig. 2g). Rotarod training correlated with an increase in the 2-amino-3-(3-hydroxy-5-methyl-isoxazol-4-yl)propanoic acid (AMPA)/*N*-methyl-D-aspartate (NMDA) ratio of the PF→STN, but not PF→CPu, circuit (Fig. 2d,e). Optogenetic terminal inhibition in STN led to a decrease in rotarod-induced cFos in STN and showed that the PF→STN circuit is necessary for motor learning (Extended Data Fig. 2h–j). Therefore, whereas PF_{CPu} neurons contribute to general motor activity, PF_{STN} neurons are critical for motor learning, revealing differential functional roles of these two PF subpopulations.

To characterize the connectivity between PF and neurons expressing D1 or D2 dopamine receptors in CPu[22], we used a Cre-dependent rabies virus[23] system (Extended Data Fig. 2k,l). D1 and D2 neurons in CPu receive PF inputs (Extended Data Fig. 2m). D1 and D2 neurons in CPu show different neuronal excitability (Extended Data Fig. 2n) and light-evoked currents were larger in D1 compared with D2 neurons (Fig. 2f). It is widely accepted that the major cell type in STN expresses a glutamatergic marker, VGLUT2[24,25] (encoded by *Slc17a6* (also known as *Vglut2*)) However, STN also contains a parvalbumin (PV, encoded by the *Pvalb* gene)-positive subpopulation[26,27], which remains understudied (Fig. 2g and Extended Data Fig. 2o). We found that a larger population of PF neurons projected to *Pvalb*$^{+}$ STN neurons than to *Vglut2*$^{+}$ STN neurons (Fig. 2h and Extended Data Fig. 3a–c), which was confirmed using ex vivo recordings (Fig. 2i).

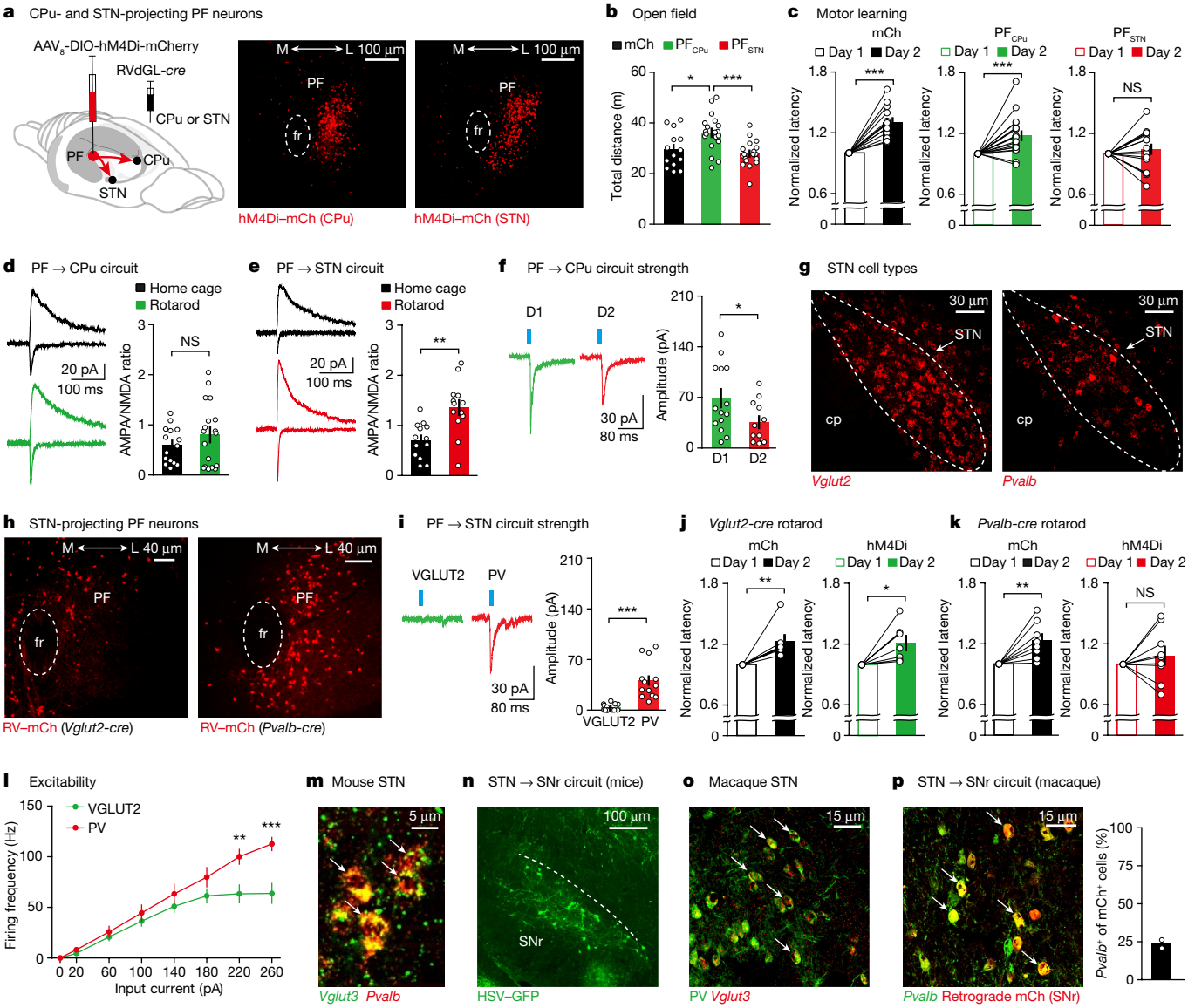

Fig. 2 | CPu- and STN-projecting PF neurons mediate different motor behaviours. a, hM4Di expression in PF. mCh, mCherry. **b**,**c**, Distance moved by mice in open field (**b**) and normalized latency to fall during rotarod training (**c**) with mCherry control or inhibition of indicated neurons (mCherry: $n = 14$ mice; PF_{CPu}: $n = 19$ mice; PF_{STN}: $n = 18$ mice). **d**,**e**, AMPA/NMDA ratio in the PF→CPu circuit of mice in home cage ($n = 15$ neurons (5, 5 and 5 neurons from 3 mice)) and following rotarod training ($n = 18$ neurons (6, 6 and 6 neurons from 3 mice)) (**d**), and in the PF→STN circuit of mice in home cage ($n = 13$ neurons (5, 4 and 4 neurons from 3 mice)) and following rotarod training ($n = 13$ neurons (4, 4 and 5 neurons from 3 mice)) (**e**). **f**, EPSCs in D1 ($n = 14$ neurons (4, 4, 3 and 3 neurons from 4 mice)) and D2 ($n = 12$ neurons (3, 2, 4 and 3 neurons from 4 mice)) neurons in the PF→CPu circuit. **g**, Fluorescence in situ hybridization (FISH) analysis of *Vglut2* and *Pvalb* expression in STN. cp, cerebral peduncle. **h**, Rabies virus tracing of PF_{STN} neurons. **i**, EPSCs evoked by PF neurons in *Vglut2*$^+$ and *Pvalb*$^+$ STN neurons (*Vglut2*$^+$: $n = 15$ neurons (4, 4, 3 and 4 neurons from 4 mice); *Pvalb*$^+$: $n = 13$ neurons (3, 3, 4 and 3 neurons from 4 mice)). **j**,**k**, Normalized latency to fall in mice with Cre-mediated inhibition of *Vglut2*$^+$ ($n = 7$ mice per condition) (**j**) or *Pvalb*$^+$ ($n = 8$ mCherry mice and $n = 9$ hM4Di mice) (**k**) STN neurons. **l**, Recordings of VGLUT2 ($n = 13$ neurons (4, 5 and 4 neurons from 3 mice)) and PV ($n = 12$ neurons (4, 3 and 5 neurons from 3 mice)) neurons from mouse STN. **m**, FISH analysis of *Vglut3* and *Pvalb* expression in STN. **n**, Anterograde tracing from STN_{PV} in mouse. **o**, FISH analysis of *Vglut3* and PV immunostaining in macaque STN; 97.6% of PV neurons expressed *Vglut3* ($n = 3$ monkeys). **p**, Of the STN neurons retrogradely labelled by injection into macaque substantia nigra pars reticulata (SNr), 23.5% also expressed *Pvalb* ($n = 2$ monkeys). Data are mean ± s.e.m. One-way ANOVA with Bonferroni correction (**b**), paired *t*-test (**c**,**j**,**k**), unpaired *t*-test (**d**–**f**,**i**), or two-way repeated ANOVA with Bonferroni correction (**l**). Two-sided tests. **b**, $F = 6.47$, $P = 0.0007$; mCherry vs PF_{CPu}: $t = 3.04$, PF_{CPu} vs PF_{STN}: $t = 4.02$. **c**, mCherry: $P < 0.0001$, PF_{CPu}: $P < 0.0001$, PF_{STN}: $P = 0.33$. **d**, $P = 0.26$. **e**, $P = 0.0012$. **f**, $P = 0.043$. **i**, $P < 0.0001$. **j**, mCherry: $P = 0.012$, hM4Di: $P = 0.022$. **k**, mCherry: $P = 0.008$, hM4Di: $P = 0.35$. **l**, $F = 5.56$, DFn = 1, DFd = 161, $P = 0.03$.

We hypothesized that *Pvalb*$^+$ STN neurons may be crucial for motor learning. Inhibition of *Pvalb*$^+$ or *Vglut2*$^+$ STN neurons showed that only the *Pvalb*$^+$-inhibited group was impaired in motor learning (Fig. 2j,k and Extended Data Fig. 3d,e). The role of *Pvalb*$^+$ STN neurons in motor learning was further supported by experiments in which *Vglut2*$^-$ neurons were inhibited during behaviour (Extended Data Fig. 3f) and by inhibition of *Pvalb*$^+$ STN neurons that receive PF inputs (Extended Data Fig. 3g).

We next compared the two STN cell types using ex vivo recordings (Extended Data Fig. 3h,i). Compared with *Vglut2*$^+$ neurons, *Pvalb*$^+$ neurons had action potentials with shorter half widths, resulting in higher excitability (Fig. 2l and Extended Data Fig. 3j). Both STN populations had comparable spontaneous firing (Extended Data Fig. 3k), input resistance (R_{in}), membrane time constant (τ), membrane capacitance (C_m) and action potential amplitude (Extended Data Fig. 3l). *Pvalb*$^+$ neurons

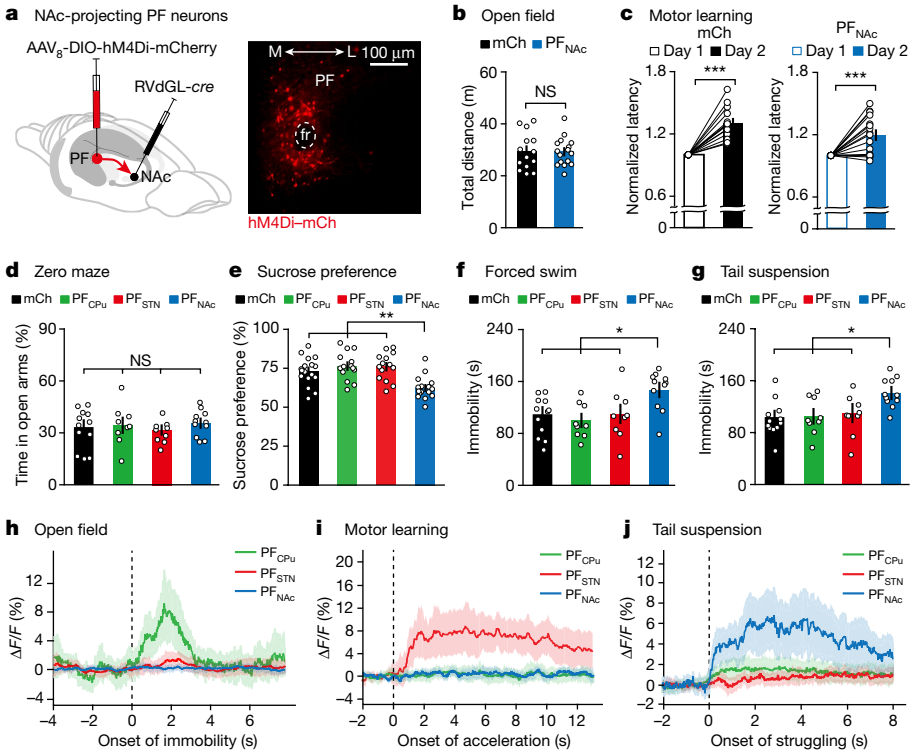

Fig. 3 | NAc-projecting PF neurons mediate depression-like behaviours. **a**, Inhibitory hM4Di expression in PF_{NAc} neurons by injection of RVdGL-cre in NAc and Cre-dependent hM4Di–mCherry in PF. **b**,**c**, Effect of inhibiting PF_{NAc} neurons in open field (**b**) and during rotarod training (**c**) ($n = 14$ and $n = 16$ PF_{NAc} mice). mCherry data are from Fig. 2b,c. **d**–**g**, Effect of inhibiting PF_{CPu}, PF_{STN} or PF_{NAc} neurons during zero maze (**d**), sucrose preference (**e**), forced swim (**f**) and tail suspension (**g**) tests (in **d**,**f**,**g**, mCherry: $n = 12$ mice; PF_{CPu}: $n = 9$ mice; PF_{STN}: $n = 9$ mice; PF_{NAc}: $n = 11$ mice; in **e**, mCherry: $n = 17$ mice; PF_{CPu}: $n = 14$ mice; PF_{STN}: $n = 14$ mice; PF_{NAc}: $n = 16$ mice). **h**–**j**, In vivo fibre photometry recordings from PF_{CPu}, PF_{STN} or PF_{NAc} neurons following injection of a retrograde AAV expressing Cre in CPu, STN or NAc and Cre-dependent GCaMP6s in PF ($n = 5$ mice per group). Fluorescence change is aligned ($t = 0$) to the onset of immobility during open field (**h**), the onset of acceleration of the rod during rotarod (**i**) or the onset of struggling during tail suspension (**j**). Data are mean ± s.e.m. Unpaired *t*-test (**b**), paired *t*-test (**c**) and one-way ANOVA with Bonferroni correction (**d**–**g**). Two-sided tests. **b**, $P = 0.94$. **c**, mCherry: $P < 0.0001$, PF_{NAc}: $P = 0.0005$. **d**, $F = 0.55$, $P = 0.65$. **e**, $F = 9.30$, $P < 0.0001$; mCherry vs PF_{NAc}: $t = 3.66$, PF_{CPu} vs PF_{NAc}: $t = 4.53$, PF_{STN} vs PF_{NAc}: $t = 4.41$. **f**, $F = 5.04$, $P = 0.005$; mCherry vs PF_{NAc}: $t = 3.09$, PF_{CPu} vs PF_{NAc}: $t = 3.41$, PF_{STN} vs PF_{NAc}: $t = 2.79$. **g**, $F = 5.20$, $P = 0.0042$; mCherry vs PF_{NAc}: $t = 3.56$, PF_{CPu} vs PF_{NAc}: $t = 2.97$, PF_{STN} vs PF_{NAc}: $t = 2.87$.

in the mammalian brain are usually inhibitory interneurons that regulate the output of neighbouring excitatory neurons[28]. However, it has been shown that STN is devoid of the inhibitory neurotransmitter GABA[29] (γ-aminobutyric acid). We found that the majority of *Pvalb*$^+$ STN neurons expressed the excitatory glutamate transporter VGLUT3 (encoded by *Slc17a8* (also known as *Vglut3*)) (Fig. 2m and Extended Data Fig. 3m). Recordings showed that *Pvalb*$^+$ neurons did not exhibit local connectivity within STN (Extended Data Fig. 3n), which led to the hypothesis that these neurons are *Pvalb*$^+$ excitatory, projection neurons. Indeed, anterograde tracing using a Cre-dependent herpes simplex virus (HSV) system (Fig. 2n and Extended Data Fig. 4a) or Cre-dependent channelrhodopsin-2 (ChR2)–eYFP-expressing terminal labelling (Extended Data Fig. 4b,c), retrograde tracing (Extended Data Fig. 4d,e), and ex vivo recordings (Extended Data Fig. 4f–j) showed that these *Pvalb*$^+$ STN neurons projected to GP and SNr[30]. Furthermore, using STN sections from macaques, we found that *Pvalb*$^+$ neurons co-expressed *Vglut3*, but not *Gad1* or *Gad2* (Fig. 2o and Extended Data Fig. 4k). A retrograde virus injected in macaque SNr resulted in dense labelling in STN, many of which were *Pvalb*$^+$ neurons (Fig. 2p). These experiments indicate that the excitatory projection *Pvalb*$^+$ STN cell type is conserved from rodents to primates.

PF→NAc neurons mediate depression

Using chemogenetics to inhibit PF_{NAc} neurons (Fig. 3a), we found that this subpopulation does not have a critical role in the two motor assays that we used (Fig. 3b,c and Extended Data Fig. 4l). Given that NAc has a critical role in anxiety and depression[13], we tested PF_{NAc}-inhibited mice in the elevated zero maze (an anxiety assay) and three assays commonly used to detect depression-like states: sucrose preference test, forced swim test and tail suspension test. Although none of the three PF subpopulations played a role in anxiety (Fig. 3d), inhibition of PF_{NAc} neurons led to a decrease in sucrose preference in sucrose preference tests and an increase in immobility in both forced swim test and tail suspension test, suggesting that this manipulation induces a depression-like state (14.75% decrease in sucrose preference test, 38.28% increase in forced swim test and 39.83% increase in tail suspension test of PF_{NAc} relative to mCherry) (Fig. 3e–g). Further supporting the role of PF_{NAc} neurons in reward processing, we found that optogenetic activation of these neurons induced real-time place preference, and that this population is necessary for cocaine-induced conditioned place preference but not a negative-valence contextual fear conditioning behaviour[31] (Extended Data Fig. 4m–p). These experiments revealed a crucial role for the PF_{NAc} subpopulation in non-motor behaviours.

To strengthen the behavioural observations regarding distinct PF subpopulations, we performed in vivo physiological analyses using fibre photometry (Extended Data Fig. 4q). We observed an increase in the activity of PF_{CPu} neurons, but not the other subpopulations, that started immediately before the onset of an immobility epoch in the open field—which was not the case before the end of immobility epochs (Fig. 3h and Extended Data Fig. 5a–f). Similarly, we observed a selective increase in the activity of PF_{STN} neurons during the onset, but not the end, of the acceleration phase in the rotarod (Fig. 3i and Extended Data Figs. 5g–j and 6a–c). These observations were not a

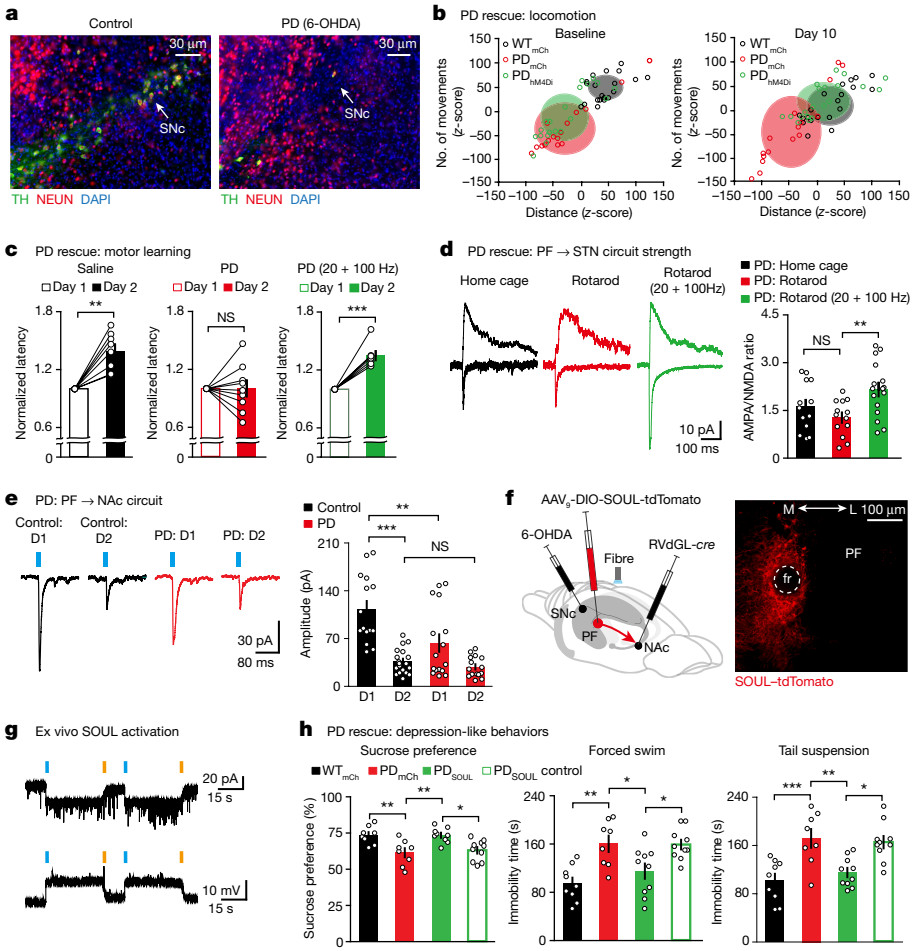

Fig. 4 | Targeting PF rescues motor deficits and depression-like behaviours in PD mice. a, Immunostaining. **b**, PF_{CPu} inhibition rescues locomotion defects in PD mice (wild-type mouse + mCherry (WT_{mCh}): $n = 20$ mice; PD mouse + mCherry (PD_{mCh}): $n = 16$ mice; PD mouse + hM4Di (PD_{hM4Di}): $n = 20$ mice). **c**, PF→STN activation during rotarod behaviour (saline: $n = 8$; PD mice: $n = 9$; PD mice, stimulation at 20 and 100 Hz: $n = 7$ mice). **d**, Recordings from the PF→STN circuit (home cage: $n = 13$ neurons (4, 4 and 5 neurons from 3 mice); rotarod: 13 neurons (5, 4 and 4 neurons from 3 mice); rotarod (stimulation at 20 and 100 Hz): 16 neurons (5, 5 and 6 neurons from 3 mice)). **e**, PF→NAc circuit recordings in control (D1: $n = 15$ neurons (3, 3, 4, 2 and 3 neurons from 5 mice); D2: 19 (5, 4, 3, 4 and 3 neurons from 5 mice)); PD (D1: $n = 16$ neurons (4, 3, 4, 3 and 2 neurons from 5 mice); D2: 15 neurons (3, 3, 3, 3 and 3 neurons from 5 mice)). **f**, PF→NAc manipulation using SOUL. **g**, Current and voltage traces from a SOUL-expressing PF_{NAc} neuron. **h**, PF_{NAc} stimulation in PD mice, sucrose (WT_{mCh}: $n = 8$ mice; PD_{mCh}: $n = 8$ mice; PD mouse + SOUL (PD_{SOUL}): $n = 9$ mice; PD mouse + SOUL + control light delivery (PD_{SOUL} control): $n = 10$ mice); forced swim or tail suspension (WT_{mCh}: $n = 9$ mice; PD_{mCh}: $n = 8$ mice; PD_{SOUL}: $n = 9$ mice; PD_{SOUL} control: $n = 10$ mice). Data are mean ± s.e.m. Paired t-test (**c**), one-way ANOVA with Bonferroni correction (**d**,**e**,**h**). Two-sided tests. **c**, Saline: $P = 0.0007$, PD mouse: $P = 0.98$, PD mouse with stimulation at 20 and 100 Hz: $P = 0.0003$. **d**, $F = 5.07$, $P = 0.011$; home cage vs rotarod: $t = 1.18$, rotarod vs rotarod with stimulation at 20 and 100 Hz: $t = 3.14$. **e**, $F = 16.24$, $P < 0.0001$; control D1 vs PD D1: $t = 3.67$, control D1 vs control D2: $t = 5.95$, control D2 vs PD D2: $t = 0.60$. **h**, Sucrose: $F = 7.72$, $P = 0.0005$; WT_{mCh} vs PD_{mCh}: $t = 3.50$, PD_{mCh} vs PD_{SOUL}: $t = 3.61$, PD_{SOUL} vs PD_{SOUL} control: $t = 3.29$; forced swim: $F = 8.67$, $P = 0.0002$; WT_{mCh} vs PD_{mCh}: $t = 4.04$, PD_{mCh} vs PD_{SOUL}: $t = 2.84$, PD_{SOUL} vs PD_{SOUL} control: $t = 2.93$; tail suspension: $F = 9.87$, $P < 0.0001$; WT_{mCh} vs PD_{mCh}: $t = 4.28$, PD_{mCh} vs PD_{SOUL}: $t = 3.54$, PD_{SOUL} vs PD_{SOUL} control: $t = 3.33$.

reflection of overall locomotion (Extended Data Figs. 5f,i,j and 6c). We also noted a selective increase in the activity of PF_{NAc} neurons during the onset of struggling epochs in the tail suspension test along with a decrease in their activity before the end of struggling epochs (Fig. 3j and Extended Data Fig. 6d–f). The specificity of these observations was confirmed by imaging from the different PF subpopulations while simultaneously performing chemogenetic inhibition of the target subpopulation during behaviour (Extended Data Fig. 6g–i). These experiments support the idea that PF contains at least three distinct functional subpopulations.

Rescue of motor and non-motor PD defects

Because both motor and non-motor deficits are widely reported in PD[1,6], we tested whether manipulating PF circuits might have multiple therapeutic effects. An acute mouse model of PD (hereafter PD mice) was created by bilateral injections of 6-hydroxydopamine in SNc[32], which led to the loss of dopaminergic cell bodies in SNc (Fig. 4a) and their terminals in CPu (Extended Data Fig. 7a). As expected[33], PD mice exhibited a decrease in locomotion (Extended Data Fig. 7b). Inhibition of PF_{CPu} neurons in wild-type mice caused an increase in locomotion (Fig. 2b), suggesting that the physiological role of PF inputs to CPu is to decrease locomotion. The strength of the PF→CPu circuit was enhanced in PD mice (Extended Data Fig. 7c), which we hypothesized may be responsible for the decreased locomotion in these mice. Inhibition of PF_{CPu} neurons improved locomotion of PD mice, which was similar to the level of control mice when tested within an hour after C21 injections[20] (Extended Data Fig. 7d–f). However, 3 days later, PD mice once again showed lower levels of locomotion compared with controls. We found that prolonged inhibition of PF_{CPu} neurons for 3 days (Extended Data Fig. 7e) resulted in similar levels of locomotion between control and PD mice 7 days and 10 days later (Fig. 4b and Extended Data

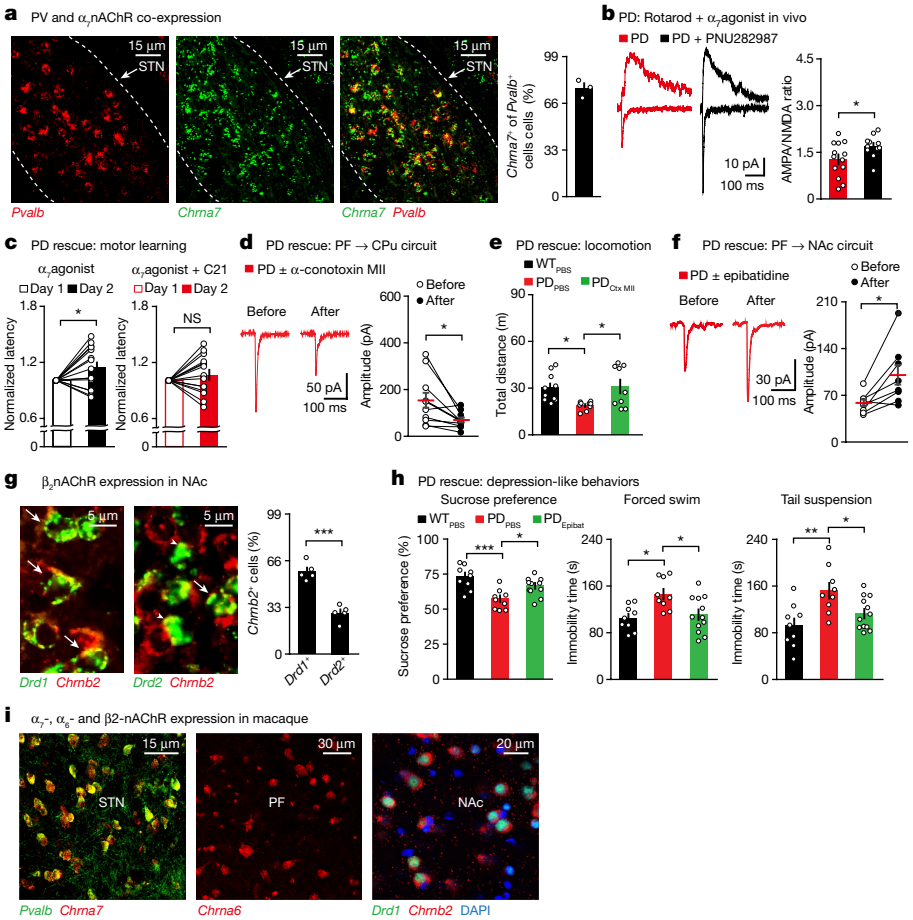

Fig. 5 | Modulating nAChRs in PF circuits rescues PD phenotypes. a, FISH analysis of *Pvalb* and α7-nAChR (encoded by *Chrna7*) expression ($n = 3$ mice). **b**, PF→STN circuit recordings (PD data are from Fig. 4d; PD + PNU282987: $n = 11$ neurons (4, 4 and 3 neurons from 3 mice)). **c**, Normalized latency with α7-nAChR activation and STN_{PV} inhibition ($n = 15$ mice). **d**, PF→CPu circuit recordings ($n = 10$ neurons (2, 2, 2, 2 and 2 neurons from 5 mice)). **e**, α-conotoxin (α-Ctx) MII infusion (1 µl) into CPu (WT mouse + PBS (WT_{PBS}): $n = 10$ mice; PD mouse + PBS (PD_{PBS}): $n = 9$ mice; PD mouse + α-Ctx MII ($PD_{Ctx\,MII}$): $n = 9$ mice). **f**, Recordings from D1 neurons in NAc that receive PF input ($n = 8$ neurons (2, 2, 2, 1 and 1 neurons from 5 mice)). **g**, FISH analysis of β2-nAChR (encoded by *Chrnb2*), and dopamine D1 (encoded by *Drd1*) and D2 (encoded by *Drd2*) receptor ($n = 5$ mice) expression. **h**, Epibatidine infusion (250 nl) into NAc, sucrose (WT_{PBS}: $n = 9$ mice; PD_{PBS}: $n = 9$ mice; PD mouse + epibatidine (PD_{Epibat}): $n = 11$ mice); forced swim (WT_{PBS}: $n = 9$ mice; PD_{PBS}: $n = 9$ mice; PD_{Epibat}: $n = 12$ mice); tail suspension (WT_{PBS}: $n = 9$ mice; PD_{PBS}: $n = 9$ mice; PD_{Epibat}: $n = 12$ mice). **i**, FISH analysis of α7-nAChR, α6-nAChR (encoded by *Chrna6*) and β2-nAChR expression with PV immunofluorescence. Blue, DAPI. Data are mean ± s.e.m. Unpaired *t*-test (**b**,**g**), paired *t*-test (**c**,**d**,**f**), one-way ANOVA with Bonferroni correction (**e**,**h**). Two-sided tests. **b**, $P = 0.042$. **c**, Agonist: $P = 0.035$, agonist + C21: $P = 0.27$. **d**, $P = 0.018$. **e**, $F = 4.91$, $P = 0.016$; WT_{PBS} vs PD_{PBS}: $t = 2.64$, PD_{PBS} vs $PD_{Ctx\,MII}$: $t = 2.80$. **f**, $P = 0.012$. **g**, $P < 0.0001$. **h**, Sucrose: $F = 10.53$, $P = 0.0004$ (WT_{PBS} vs PD_{PBS}: $t = 4.57$, PD_{PBS} vs PD_{Epibat}: $t = 2.79$), forced swim: $F = 6.19$, $P = 0.0061$ (WT_{PBS} vs PD_{PBS}: $t = 3.20$, PD_{PBS} vs PD_{Epibat} $t = 2.95$), tail suspension: $F = 7.00$, $P = 0.0035$ (WT_{PBS} vs PD_{PBS} $t = 3.68$, PD_{PBS} vs PD_{Epibat}: $t = 2.56$).

Fig. 7g–j). Therefore, inhibition of PF_{CPu} neurons offers an approach for the long-term rescue of locomotion defects in PD mice.

In addition to the locomotion phenotype in PD mice, we observed impairments in their motor learning[33] (Fig. 4c). In contrast to wild-type mice (Fig. 2e), PD mice lacked a learning-induced enhancement in the strength of the PF→STN circuit (Fig. 4d and Extended Data Fig. 8a), which correlated with the lack of rotarod-induced cFos in STN (Extended Data Fig. 8b). We proposed that strengthening the PF→STN circuit might rescue this phenotype. To test this idea, we employed an in vivo optical LTP approach for circuit strengthening, which activated neurons at 100 Hz using oChIEF[34,35]. We activated PF terminals in STN using three different protocols (Extended Data Fig. 8c,d). To determine whether increasing PF→STN activity during rotarod trials or strengthening the PF→STN circuit between trials is sufficient to rescue motor learning, we tested 20 Hz stimulation during rotarod or 100 Hz stimulation between trials. Since neither improved motor learning in PD mice (Extended Data Fig. 8e), we activated the PF→STN circuit using a combination of 20 Hz and 100 Hz protocols (20 + 100 Hz, hereafter referred to as optical LTP). Optical LTP applied to the PF→STN circuit rescued motor learning (Fig. 4c), and led to a learning-induced circuit strengthening (Fig. 4d) together with significant STN cFos accumulation (Extended Data Fig. 8f). Inhibition of *Pvalb*$^+$ STN neurons prevented this LTP-based rescue (Extended Data Fig. 8g,h), which directly demonstrated the crucial role of *Pvalb*$^+$ STN neurons in this rescue approach.

We next investigated a common non-motor deficit in PD, specifically depression[6]. PD mice showed decreased preference in sucrose preference tests (Extended Data Fig. 8i), along with increased immobility in both forced swim test and tail suspension test (Extended Data Fig. 8j), indicating a depression-like state. Similar to the PF→CPu circuit, both D1 and D2 neurons in NAc receive PF inputs (Extended Data Fig. 8k–m), D1 and D2 neurons in NAc showed distinct excitability (Extended Data Fig. 8n), and light-evoked currents ex vivo were larger in D1 neurons (Fig. 4e). PD mice showed a decrease in the response of D1 neurons to PF inputs ex vivo, whereas D2 responses were unaffected (Fig. 4e). We speculated that increasing PF_{NAc} activity during behaviour might be sufficient to rescue PD phenotypes. Given the forced swim test and tail suspension test protocols, a minimally invasive neuronal

manipulation method would be preferred; we therefore used the stable step-function opsin SOUL[36]. When expressed in the mouse brain, this opsin can be activated by a brief light stimulation from outside the skull[36]. We generated a Cre-dependent SOUL virus and verified PF_{NAc} labelling (Fig. 4f), and validated our ability to depolarize these neurons (Fig. 4g and Extended Data Fig. 8o). Activating PF_{NAc} neurons in PD mice improved performance in all three assays used to detect depression-like states (Fig. 4h). Therefore, modulating PF circuits is an effective approach to rescue motor and non-motor deficits in PD mice.

Targeting PF nAChRs rescues PD defects

Since strengthening PF inputs to *Pvalb*$^+$ STN neurons optogenetically was sufficient for behavioural rescue in PD mice, we tested whether a similar effect might be achieved using a molecular target. We used two criteria to identify candidate molecular targets: (1) molecules that are capable of modulating synaptic plasticity in multiple brain regions based on the literature, and (2) molecules that are expressed in STN[37] (Extended Data Fig. 9a). Using these criteria, we narrowed the list of targets down to α7 nicotinic acetylcholine receptors[38] (nAChRs), the nitric oxide receptor GUCD1[39], the ERBB4 receptor[40] and the μ-opioid receptor OPRM1[41]. We tested whether modulating these candidate molecular targets ex vivo could enhance synaptic plasticity in the PF→STN circuit of PD mice. We established a baseline condition in which the PF→STN circuit from PD mice did not exhibit an increase in synaptic strength following optical high-frequency stimulation (HFS) (Extended Data Fig. 9b). Although a nitric oxide receptor agonist, an ERBB4 receptor antagonist and a μ-opioid receptor agonist did not strengthen this circuit (Extended Data Fig. 9c), the α7-nAChR agonist PNU282987[42] caused an increase in the AMPA/NMDA ratio after HFS (Extended Data Fig. 9d). We demonstrated directly that *Pvalb*$^+$ STN neurons expressed high levels of α7-nAChRs (Fig. 5a). When we performed rotarod training in PD mice injected with PNU282987, we detected an increase in the synaptic strength of PF inputs to *Pvalb*$^+$ STN neurons ex vivo (Fig. 5b), which was accompanied by a significant improvement in motor learning (Fig. 5c and Extended Data Fig. 9e). This PNU282987-induced rescue of motor learning was blocked by simultaneous chemogenetic inhibition of *Pvalb*$^+$ STN neurons, suggesting that activation of α7-nAChRs specifically in *Pvalb*$^+$ STN neurons is necessary for behavioural rescue in PD mice (Fig. 5c). This idea was supported by performing a CRISPR–Cas9-based in vivo knockdown[43] of α7-nAChRs from *Pvalb*$^+$ STN neurons specifically, which blocked the motor learning rescue effect of PNU282987 in PD mice (Extended Data Fig. 9f,g).

The knockdown of α6-nAChR in PF alleviates certain motor phenotypes in PD mice[44]. Consistent with this study, an α6-nAChR antagonist[45] reduces the strength of the PF→CPu circuit in PD mice ex vivo (Fig. 5d). We observed that α6-nAChRs are enriched in PF_{CPu} neurons but are not expressed by D1 or D2 medium spiny neurons (MSNs) in CPu (Extended Data Fig. 9h), suggesting that α6-nAChRs modulate the PF→CPu circuit using a presynaptic mechanism. Local infusions of the α6-nAChR antagonist in CPu of PD mice rescued their locomotion deficit (Fig. 5e and Extended Data Fig. 9i). Similarly, when we performed a circuit-based in vivo knockdown[43] of α6-nAChRs selectively from PF_{CPu} neurons in PD mice, we rescued their locomotion deficit (Extended Data Fig. 9j,k). These findings suggested that targeting nAChRs in different PF circuits is sufficient to rescue motor phenotypes in PD mice. To extend this approach to the PF→NAc circuit, we identified several nAChRs (α3, α6, α7 and β2) that are expressed in PF and NAc according to the Allen Brain Atlas in situ hybridization database[37]. Using agonists for each of these nAChRs, recordings showed that modulating β2-nAChRs increases the strength of PF inputs to D1 neurons in NAc (Fig. 5f and Extended Data Fig. 10a). Complementing this observation, β2-nAChRs are enriched in D1 NAc neurons compared with D2 NAc neurons (Fig. 5g). Local infusions of the β2-nAChR agonist in NAc of PD mice led to improved performance in all three assays of depression-like behaviours (Fig. 5h and Extended Data Fig. 10b). Also, selective knockdown of β2-nAChRs in D1$^+$ NAc neurons blocked the rescue effect of the β2-nAChR agonist, further strengthening our observations (Extended Data Fig. 10c,d). Similar to mice, α7-nAChRs are highly expressed in *Pvalb*$^+$ STN neurons, α6-nAChRs are expressed in PF neurons, and β2-nAChRs are highly expressed in D1$^+$ NAc neurons in macaque (Fig. 5i). Together, these data suggest that targeting different nAChRs in PF circuits may offer a potential therapeutic approach to alleviate both motor and non-motor deficits in PD.

Discussion

The interest in PF thalamus originated from anatomical studies showing extensive connectivity with the basal ganglia network[7,8]. It has since been shown that PF contributes to motor tasks such as reversal learning and movement sequences, which is thought to arise from its projections to CPu[9,10]. Although heterogeneity within PF has been suggested[46,47], whether distinct circuits underlie different motor behaviours remains understudied. Also, the potential role of PF projections to NAc[12] has not been revealed. Here we have shown that PF neurons projecting to CPu, STN and NAc are distinct subpopulations and have differential functional relevance: motor behaviours (PF→CPu and PF→STN) versus non-motor behaviours (PF→NAc). Whereas NAc-projecting neurons are restricted to medial PF, CPu- and STN-projecting neurons can be found intermingled mostly in lateral PF, indicating differences in the spatial localization of PF subpopulations. Among these three subpopulations, NAc-projecting PF neurons exhibit the most unique electrophysiological profile. We noted that both D1 and D2 neurons in NAc receive PF inputs, similar to D1 and D2 neurons in CPu. Notably, in both NAc and CPu, D2 neurons exhibited higher ex vivo excitability compared with D1. Classical models suggest that these cell types support differential functions in NAc[48] (D1 for reward and D2 for aversion) and CPu[49] (D1 to promote movement and D2 to inhibit movement). Because D2 neurons are recruited to regulate reward or movement behaviour in both NAc and CPu, it may be essential for this cell type to be more excitable and thus be more responsive to small changes in incoming synaptic inputs.

Similar to patients with PD[1,4], mouse models of PD have impairments in both locomotion and motor learning, which we rescued by manipulating CPu- and STN-projecting PF subpopulations in the same mice (Extended Data Fig. 10e–g). With regards to the rescue of locomotion in PD model mice, acute manipulations of PF_{CPu} neurons improved behavioural performance immediately, consistent with a previous report[20]. However, we found that this rescue was not long lasting, which was not examined by the previous study. We made a surprising finding that a prolonged manipulation protocol resulted in a long-lasting rescue of locomotion in PD model mice (up to 10 days later). A recent study showed that distinct PF subpopulations project to CPu versus STN[50], consistent with our results, and found that the activation of the PF→STN circuit, but not the PF→CPu circuit, increases locomotion. Although these behavioural observations suggest differential functions of these PF circuits, the function of the PF→CPu circuit was not revealed, and importantly, different from our study, the authors of the other study did not use loss-of-function manipulations to identify the physiological role of these circuits in behaviour. Our work using loss-of-function experiments led to the identification of new functions for the different PF circuits. This recent study[50] also showed that the activation (using 5-40 Hz stimulation protocols) of the PF→STN circuit in PD mice is sufficient to rescue locomotion and a variety of natural behaviours. In the present study, because we found that the PF→STN circuit is necessary for motor learning, but not locomotion, and that this circuit is weakened in PD model mice, we employed an optical LTP protocol (approximately 100 Hz) to strengthen this circuit and restore motor learning behaviour. Together, these observations suggest that

the activation of the PF→STN circuit, depending on the stimulation parameters used, may alleviate both locomotion and motor learning deficits in PD.

In addition to motor phenotypes, patients with PD experience severe non-motor symptoms, including depression[6], which can also be observed in PD mice. Using a minimally invasive optogenetic approach[36] to modulate PF_{NAc} neurons, we demonstrated that activating this specific PF subpopulation in PD mice is sufficient to alleviate depression-like behaviours. Because these findings are based exclusively on male mice and sex differences are well documented in PD, future research is needed to determine whether these circuit manipulations are equally effective in female mice. This is particularly important for the rescue of depression-like behaviours, which is a severe mood disorder that is approximately twice as prevalent in women than in men. Nevertheless, our observations highlight the importance of heterogeneous PF neurons to behaviour, in both normal and disease states, and suggests that both motor and non-motor PD deficits may be treated by targeting PF thalamic circuits.

Although levodopa and STN DBS are effective treatments for a range of motor symptoms in PD, slower motor learning and subsequent retention deficits do not respond well to these approaches[5]. In this study, we demonstrated that strengthening the PF→STN circuit in PD mice was sufficient to restore long-term motor learning. Further experiments aimed at understanding the cellular basis of this rescue in PD mice revealed that a *Pvalb*$^+$ excitatory STN cell type was crucial. This observation suggests that STN, although generally considered to be homogeneous, contains distinct functional subpopulations[25]. In addition to our experiments showing that selective strengthening of PF inputs to *Pvalb*$^+$ STN neurons can rescue motor learning deficits, we showed that the majority of *Pvalb*$^+$ STN neurons express α7-nAChRs, which if activated in PD mice using an agonist led to the rescue of motor learning deficits in a *Pvalb*$^+$ STN neuron-dependent manner. Because we found that STN of macaques also contain excitatory projection *Pvalb*$^+$ neurons that co-express α7-nAChRs and previous work has reported the presence of *Pvalb*$^+$ STN neurons in human samples[30], our mechanistic findings in rodent STN may be conserved in higher species such as non-human primates and even in humans.

Finally, we identified molecular targets capable of modulating the three different PF circuits. Similar to our PF→STN α7-nAChR experiments, another group has reported that modulating α6-nAChRs in PF improves certain motor behaviours[44]. Building on their work, we showed that an α6-nAChR antagonist targeting PF_{CPu} neurons rescues locomotion. Furthermore, we found that PF inputs to D1 neurons in NAc are selectively weakened in PD mice. Using a β2-nAChR agonist, we were able to rescue the strength of PF inputs to NAc D1$^+$ neurons in PD mice and their depression-like behavioural deficits. Together, we not only identified circuit mechanisms responsible for motor and non-motor deficits in PD mice, but also propose that using nAChRs capable of regulating three distinct PF circuits offers an exciting therapeutic avenue for PD.

Online content

Any methods, additional references, Nature Research reporting summaries, source data, extended data, supplementary information, acknowledgements, peer review information; details of author contributions and competing interests; and statements of data and code availability are available at https://doi.org/10.1038/s41586-022-04806-x.

1. Albin, R. L., Young, A. B. & Penney, J. B. The functional anatomy of basal ganglia disorders. *Trends Neurosci.* **12**, 366–375 (1989).
2. The Parkinson Study Group. Levodopa and the progression of Parkinson's disease. *N. Engl. J. Med.* **351**, 2498–2508 (2004).
3. Hamani, C., Saint-Cyr, J. A., Fraser, J., Kaplitt, M. & Lozano, A. M. The subthalamic nucleus in the context of movement disorders. *Brain* **127**, 4–20 (2004).
4. Smiley-Oyen, A. L., Worringham, C. J. & Cross, C. L. Motor learning processes in a movement-scaling task in olivopontocerebellar atrophy and Parkinson's disease. *Exp. Brain Res.* **152**, 453–465 (2003).
5. Marinelli, L., Quartarone, A., Hallett, M., Frazzitta, G. & Ghilardi, M. F. The many facets of motor learning and their relevance for Parkinson's disease. *Clin. Neurophysiol.* **128**, 1127–1141 (2017).
6. Poewe, W. Non-motor symptoms in Parkinson's disease. *Eur. J. Neurol.* **15**, 14–20 (2008).
7. Saalmann, Y. B. Intralaminar and medial thalamic influence on cortical synchrony, information transmission, and cognition. *Front. Syst. Neurosci.* **8**, 83 (2014).
8. Smith, Y., Raju, D. V., Pare, J. F. & Sidibe, M. The thalamostriatal sytem: a highly specific network of the basal ganglia circuitry. *Trends Neurosci.* **27**, 520–527 (2004).
9. Brown, H. D., Baker, P. M. & Ragozzino, M. E. The parafascicular thalamic nucleus concomitantly influences behavioral flexibility and dorsomedial striatal acetylcholine output in rats. *J. Neurosci.* **30**, 14390–14398 (2010).
10. Diaz-Hernandez, E. et al. The thalamostriatal projections contribute to the initiation and execution of a sequence of movements. *Neuron* **100**, 739–752 (2018).
11. Jouve, L., Salin, P., Melon, C. & Kerkerian-Le Goff, L. Deep brain stimulation of the center median-parafascicular complex of the thalamus has efficient anti-parkinsonian action associated with widespread cellular responses in the basal ganglia network in a rat model of Parkinson's disease. *J. Neurosci.* **30**, 9919–9928 (2010).
12. Berendse, H. W. & Groenewegen, H. J. Organization of the thalamostriatal projections in the rat, with special emphasis on the ventral striatum. *J. Comp. Neurol.* **299**, 187–228 (1990).
13. Heshmati, M. & Russo, S. J. Anhedonia and the brain reward circuitry in depression. *Curr. Behav. Neurosci. Rep.* **2**, 146–153 (2015).
14. Smith, Y. & Parent, A. Differential connections of caudate nucleus and putamen in the squirrel monkey (*Saimiri sciureus*). *Neuroscience* **18**, 347–371 (1986).
15. Kita, T., Shigematsu, N. & Kita, H. Intralaminar and tectal projections to the subthalamus in the rat. *Eur. J. Neurosci.* **44**, 2899–2908 (2016).
16. Mouroux, M., Hassani, O. K. & Feger, J. Electrophysiological study of the excitatory parafascicular projection to the subthalamic nucleus and evidence for ipsi- and contralateral controls. *Neuroscience* **67**, 399–407 (1995).
17. Wickersham, I. R., Sullivan, H. A. & Seung, H. S. Axonal and subcellular labelling using modified rabies viral vectors. *Nat. Commun.* **4**, 2332–2332 (2013).
18. Chatterjee, S. et al. Nontoxic, double-deletion-mutant rabies viral vectors for retrograde targeting of projection neurons. *Nat. Neurosci.* **21**, 638–646 (2018).
19. Thompson, K. J. et al. DREADD agonist 21 is an effective agonist for muscarinic-based DREADDs in vitro and in vivo. *ACS Pharmacol. Transl. Sci.* **1**, 61–72 (2018).
20. Parker, P. R. L., Lalive, A. L. & Kreitzer, A. C. Pathway-specific remodeling of thalamostriatal synapses in parkinsonian mice. *Neuron* **89**, 734–740 (2016).
21. Luh, L. M., Das, I. & Bertolotti, A. qMotor, a set of rules for sensitive, robust and quantitative measurements of motor performances in mice. *Nat. Protoc.* **12**, 1451–1457 (2017).
22. Voorn, P., Vanderschuren, L. J., Groenewegen, H. J., Robbins, T. W. & Pennartz, C. M. Putting a spin on the dorsal-ventral divide of the striatum. *Trends Neurosci.* **27**, 468–474 (2004).
23. Wickersham, I. R. et al. Monosynaptic restriction of transsynaptic tracing from single, genetically targeted neurons. *Neuron* **53**, 639–647 (2007).
24. Barroso-Chinea, P. et al. Expression of the mRNAs encoding for the vesicular glutamate transporters 1 and 2 in the rat thalamus. *J. Comp. Neurol.* **5**, 703–715 (2007).
25. Parolari, L., Schneeberger, M., Heintz, N. & Friedman, J. M. Functional analysis of distinct populations of subthalamic nucleus neurons on Parkinson's disease and OCD-like behaviors in mice. Preprint at *bioRxiv* https://doi.org/10.1038/s41380-021-01162-6 (2020).
26. Hontanilla, B., Parent, A. & Gimenez-Amaya, J. M. Parvalbumin and calbindin D-28k in the entopeduncular nucleus, subthalamic nucleus, and substantia nigra of the rat as revealed by double-immunohistochemical methods. *Synapse* **4**, 359–367 (1997).
27. Levesque, J. C. & Parent, A. GABAergic interneurons in human subthalamic nucleus. *Mov. Disord.* **5**, 574–584 (2005).
28. Ferguson, B. R. & Gao, W. J. PV interneurons: Critical regulators of E/I balances for prefrontal cortex-dependent behavior and psychiatric disorders. *Front. Neural Circuits* **12**, 37 (2018).
29. Smith, Y. & Parent, A. Neurons of the subthalamic nucleus in primates display glutamate but not GABA immunoreactivity. *Brain Res.* **453**, 353–356 (1988).
30. Emmi, A., Antonini, A., Macchi, V., Porzionato, A. & De Caro, R. Anatomy and connectivity of the subthalamic nucleus in humans and non-human primates. *Front. Neuroanat.* **14**, 13 (2020).
31. Zhang, Y. et al. MeCP2 in cholinergic interneurons of nucleus accumbens regulates fear learning. *eLife* **9**, e55342 (2020).
32. Deumens, R., Blokland, A. & Prickaerts, J. Modeling Parkinson's disease in rats: an evaluation of 6-OHDA lesions of the nigrostriatal pathway. *Exp. Neurol.* **175**, 303–317 (2002).
33. Carvalho, M. M. et al. Behavioral characterization of the 6-hydroxydopamine model of Parkinson's disease and pharmacological rescuing of non-motor deficits. *Mol. Neurodegener.* **8**, 14 (2013).
34. Nabavi, S. et al. Engineering a memory with LTD and LTP. *Nature* **511**, 348–352 (2014).
35. Roy, D. S. et al. Memory retrieval by activating engram cells in mouse models of early Alzheimer's disease. *Nature* **531**, 508–512 (2016).
36. Gong, X. et al. An ultra-sensitive step-function opsin for minimally invasive optogenetic stimulation in mice and macaques. *Neuron* **107**, 38–51 (2020).
37. Lein, E. S. et al. Genome-wide atlas of gene expression in the adult mouse brain. *Nature* **445**, 168–176 (2007).
38. Feduccia, A. A., Chatterjee, S. & Bartlett, S. E. Neuronal nicotinic acetylcholine receptors: neuroplastic changes underlying alcohol and nicotine addictions. *Front. Mol. Neurosci.* **5**, 83 (2012).

39. Pettorossi, V. E. & Grassi, S. Different contributions of platelet-activating factor and nitric oxide in long-term potentiation of the rat medial vestibular nuclei. *Acta Otolaryngol. Suppl.* **545**, 160–165 (2001).
40. Pitcher, G. M., Beggs, S., Woo, R. S., Mei, L. & Salter, M. W. ErbB4 is a suppressor of long-term potentiation in the adult hippocampus. *Neuroreport* **19**, 139–143 (2008).
41. Derrick, B. E. & Martinez, J. L. Opioid receptor activation is one factor underlying the frequency dependence of mossy fiber LTP induction. *J. Neurosci.* **14**, 4359–4367 (1994).
42. Hajos, M. et al. The selective α7 nicotinic acetylcholine receptor agonist PNU-282987 [*N*-[(3R)-1-Azabicyclo[2.2.2]oct-3-yl]-4-chlorobenzamide hydrochloride] enhances GABAergic synaptic activity in brain slices and restores auditory gating deficits in anesthetized rats. *J. Pharmacol. Exp. Ther.* **312**, 1213–1222 (2005).
43. Roy, D. S. et al. Anterior thalamic dysfunction underlies cognitive deficits in a subset of neuropsychiatric disease models. *Neuron* **109**, 2590–2603 (2021).
44. Tanimura, A., Du, Y., Kondapalli, J., Wokosin, D. L. & Surmeier, D. J. Cholinergic interneurons amplify thalamostriatal excitation of striatal indirect pathway neurons in Parkinson's disease models. *Neuron* **101**, 444–458 (2019).
45. McIntosh, J. M. et al. Analogs of alpha-conotoxin MII are selective for α_6-containing nicotinic acetylcholine receptors. *Mol. Pharmacol.* **65**, 944–952 (2004).
46. Beatty, J. A., Sylwestrak, E. L. & Cox, C. L. Two distinct populations of projection neurons in the rat lateral parafascicular thalamic nucleus and their cholinergic responsiveness. *Neuroscience* **162**, 155–173 (2009).
47. Mandelbaum, G. et al. Distinct cortical–thalamic–striatal circuits through the parafascicular nucleus. *Neuron* **102**, 636–652 (2019).
48. Klawonn, A. M. & Malenka, R. C. Nucleus accumbens modulation in reward and aversion. *Cold Spring Harb. Symp. Quant. Biol.* **83**, 119–129 (2018).
49. Nelson, A. B. & Kreitzer, A. C. Reassessing models of basal ganglia function and dysfunction. *Annu. Rev. Neurosci.* **37**, 117–135 (2014).
50. Watson, G. D. R. et al. Thalamic projections to the subthalamic nucleus contribute to movement initiation and rescue of parkinsonian symptoms. *Sci. Adv.* **7**, eabe9192 (2021).

Publisher's note Springer Nature remains neutral with regard to jurisdictional claims in published maps and institutional affiliations.

© The Author(s), under exclusive licence to Springer Nature Limited 2022

Methods

Subjects

Mice. C57BL/6J wild-type, *Vglut2-cre* (stock no. 028863), *Pvalb-cre* (stock no. 017320), D2-eGFP (stock no. 030255), *Pvalb-Flp* (stock no. 022730), and D1-Cre (stock no. 030329) mice were obtained from Jackson Laboratory. D2-cre (*Drd2-cre*) mice were imported from the GENSAT Project at Rockefeller University. All mice were housed in a facility with a light cycle running from 07:00 to 19:00 with a temperature of 18–23 °C and humidity maintained between 40 and 60%. Food andwater were available ad libitum. Adult mice were housed in groups (2 to 5 mice per cage) before surgery. Following surgery, mice were single housed. Male mice at 9–20 weeks of age were used for all experiments. All experimental procedures were conducted in accordance with the U.S. National Institutes of Health (NIH) guidelines and the Massachusetts Institute of Technology Department of Comparative Medicine and Committee of Animal Care.

Monkeys. Cynomolgus monkeys (*Macaca fascicularis*) (male, 2–3 years old, weight 2.0–2.3 kg) were housed in an environmentally controlled facility (temperature: 22 ± 1 °C, humidity: 50 ± 5% relative humidity). All monkeys were fed with commercial monkey food twice per day, plus one meal of seasonal fruits daily, and had free access to water. Monkeys were under careful veterinary monitoring twice per day to evaluate and ensure their health status. The primate facility used was accredited by the Association for Assessment and Accreditation of Laboratory Animal Care (AAALAC) and therefore followed their guidelines closely.

Fluorescent in situ hybridization in mice

Mouse brain samples were carefully extracted, embedded in OCT compound (Tissue-Tek) and flash frozen. Coronal sections (16 µm thickness) were prepared on a cryostat (Leica) and stored at −80°C until staining. ACD RNAScope multiplex fluorescent protocol was applied for mRNA FISH staining using fresh frozen tissues. In brief, charged slides with slices were fixed in pre-chilled paraformaldehyde (PFA) for 30 min, followed by a series of dehydration steps using 50%, 70% and 100% ethanol. Sections were then permeabilized with ACD protease IV for 30 min, followed by probe hybridization for 2 h at 40 °C. Fluorescent labelling of up to 3 probes per section was performed using four steps of Amp 1-FL to Amp 4-FL. Sections were stained with DAPI and stored at 4 °C. Mouse ACD probes for *Vglut2* (cat. no. 319171), *Pvalb* (cat. no. 421931), *GFP* (cat. no. 409011), mCherry (cat. no. 431201), *eYFP* (cat. no. 312131), *Chrna7* (cat. no. 465161), *Chrna6* (cat. no. 467711), *Vglut3* (cat. no. 431261), *Chrnb2* (cat. no. 449231), *Drd1* (cat. no. 406491), *Drd2* (cat. no. 406501), *Oprm1* (cat. no. 315841), *Gucd1* (cat. no. 870431) and *ErbB4* (cat. no. 318721) were used. To increase the signal for *Vglut2*, *Pvalb* and *Vglut3* in neuronal cell bodies, mice were treated with an intracerebroventricular injection of colchicine (6 µg in 1 µl, Sigma) 48 h before tissue collection. Stained sections were imaged with a 20× magnification objective on a Leica confocal microscope.

FISH in macaque

Coding region fragments of macaque *Gad1, Gad2, Vglut3, Chrna7*, *Chrna6*, *Chrnb2* and *Drd1* were isolated from monkey brain cDNA using PCR amplification. The amplified fragments were cloned into the pCR4 Topo vector (Thermo Fisher). Hybridization was performed as previously described with minor modifications[51]. In brief, digoxigenin (DIG)-labelled cRNA probes (riboprobes) were prepared using the DIG RNA labelling mix (Roche). Brains were frozen in OCT (Tissue-Tek), and coronal cryostat sections of 50 µm thickness were hybridized to DIG-labelled cRNA probes at 56 °C for 15-18 h. After hybridization, sections were washed twice in 0.2× SSC at 62 °C for 30 min, incubated with peroxidase-conjugated anti-DIG antibodies (1:500, Roche, cat. no. 1207733910) at 37 °C for 2 h, and then treated with the TSA-plus kit (Perkin Elmer).

Immunohistochemistry in mice

Mice were anaesthetized with isoflurane and transcardially perfused with PBS followed by 4% PFA. Brains were extracted and post-fixed with 4% PFA overnight. Next, brains were transferred to PBS and sectioned into 50 µm coronal sections using a vibratome. Sections were stored at 4 °C in PBS until they were processed. For immunohistochemistry, free-floating sections were washed with PBS 3 times (5 min each) and incubated with blocking buffer that contained 5% normal goat serum dissolved in 0.2% Triton X-100 in PBS (PBST) for 1 h. Sections were then incubated with primary antibody (diluted in blocking buffer) overnight at 4 °C. After primary labelling, sections were washed 3 times (10 min each) with PBST, followed by a 2 h incubation with the secondary antibody. After 3 washes (10 min each) with PBST, sections were transferred onto charged Super Frost slides and mounted under glass coverslips with mounting media. The tyramide signal amplification (TSA)-immunohistochemistry protocol was applied for STN and PF cFos staining experiments. Following primary antibody incubation as described above, sections were introduced to a secondary antibody working solution (Opal Polymer HRP Ms + Rb in blocking/Ab diluent, 1:100) for 30 min at room temperature. After 3 washes (10 min each) with PBST, sections were transferred to a TSA Plus working solution (Opal 520 or Opal 570 in 1× plus amplification diluent, 1:100) for 15 min at room temperature. After 3 more wash steps of 15 min each in PBST, slices were mounted on microscope slides and imaged with a 20× magnification objective on a Leica confocal microscope. Antibodies used for staining were as follows: chicken anti-GFP (1:1,000, Life Technologies) and anti-chicken Alexa-488 (1:1,000), rabbit anti-RFP (1:1,000, Rockland) and anti-rabbit Alexa-555 (1:500), mouse anti-NEUN (1:200, Millipore) and anti-mouse Alexa-555 (1:500), mouse anti-TH (1:1,000, Immunostar) and anti-mouse Alexa-488 (1:500), rabbit anti-cFos (1:500, Cell Signaling Technology), and all nuclei were stained with DAPI (1:3,000, Sigma) shown in the blue channel. To increase cFos signal in STN neuronal cell bodies, mice were treated with an intracerebroventricular injection of colchicine (6 µg in 1 µl, Sigma) 48 h before behaviour and perfusion fixation.

Cell counting in mice

Images were processed using ImageJ, and final quantifications were performed manually from 3–5 sections per mouse. Counting experiments were conducted blind to experimental group where researcher 1 prepared slices and performed staining experiments and researcher 2 performed quantification analyses. For experiments using virus-injected mice, researcher 1 started by verifying accurate viral targeting and only those samples that passed this checkpoint were included in further analyses. For each fluorescence channel, a threshold was carefully determined in ImageJ that permitted the automatic identification of putative fluorescently labelled neurons across 2–3 slices from at least 3 mice per experiment. This process allowed for a standardization of the fluorescence intensity threshold per channel. Because this automatic identification often labelled a single neuron with several maxima, it was necessary to use visual inspection and perform manual cell counting in order to obtain the most accurate number of neurons expressing each target protein. This approach was also used to quantify co-expression of multiple fluorescent proteins. To quantify the chance level at which retrograde tracing of CPu, STN or NAc using CTB results in non-overlapping PF populations, we performed NEUN staining and found that 35.99% of PF neurons project to CPu, 30.11% of PF neurons project to STN, and 18.52% of PF neurons project to NAc. Assuming the projections from PF to downstream nuclei arise from distinct populations, chance level for PF neurons that project to CPu only was calculated as $0.3599 \times (1 - 0.3011) \times (1 - 0.1852) = 0.2049$, chance level for PF neurons that project to STN only was calculated as $0.3011 \times (1 - 0.3599) \times (1 - 0.1852) = 0.157$, and chance level for PF neurons that project to NAc only was calculated as $0.1852 \times (1 - 0.3599) \times (1 - 0.3011) = 0.0828$.

Immunohistochemistry in macaque

Macaques were deeply anaesthetized with sodium pentobarbital (nembutal; 80 mg kg^{-1}, intraperitoneal injection) and perfused with PBS (0.1 M) and 4% paraformaldehyde in PBS (4% PFA/PBS, 4 °C, 500 ml). The dissected brains were post-fixed at 4 °C in 4% PFA/PBS and cryo-protected at 4 °C in 30% sucrose/PBS. Coronal sections (50 µm) were prepared using a vibrating blade microtome (Leica, CM1950). All sections were post-fixed for 20 min at 4 °C in 4% PFA/PBS. Sections were blocked and permeabilized for 1 h at room temperature in a PBS solution containing 5% bovine serum albumin (BSA) and 0.3% Triton X-100. The primary antibody incubation was performed by incubating the sections overnight at 4 °C in a PBS solution containing 5% BSA, polyclonal anti-RFP (1:500, Rockland, cat. no. 600-401-379), and anti-PV (1:500, Swant, cat. no. 235). The secondary antibody incubation was performed for 1 h using Alexa Fluor 594 donkey anti-rabbit IgG and Alexa Fluor 488 donkey anti-mouse IgG (1:500, Thermo Fisher cat. no. A32754 and cat. no. A21202, respectively). Nuclei were stained with DAPI (Sigma-Aldrich, cat. no. D9542) shown in the blue channel. Brain sections were mounted onto slides using Fluoromount-G mounting medium (SouthernBiotech, cat. no. 0100-01).

Cell counting in macaque

Images were acquired using a confocal microscope (LSM 800, Carl Zeiss) with a 20× magnification objective. Brain structures were identified microscopically and in digital photos using a monkey brain atlas. Quantifications were performed from three macaques. Three slices form rostral to caudal STN were analysed. Cell counting was done in ImageJ, and all measurements were made independently and blindly.

Virus preparation

AAV_9-EF1α-DIO-ChR2-eYFP (#20298, 7×10^{12} GC ml^{-1} viral titre), AAV_9-CaMKII-ChR2-eYFP (#26969, 1×10^{13} GC ml^{-1} viral titre), AAV_9-CaMKII-ChR2-mCherry (#26975, 7×10^{12} GC ml^{-1} viral titre), AAV_8-hSyn-DIO-hM4Di-mCherry (#44362, 1×10^{13} GC ml^{-1} viral titre), AAV_8-hSyn-DIO-mCherry (#50459, 7×10^{12} GC ml^{-1} viral titre), AAV_1-hSyn-Cre (#105553, 1×10^{13} GC ml^{-1} viral titre), AAV_8-EF1α-COn/FOn-NpHR3.3-eYFP (#137152, 1×10^{13} GC ml^{-1} viral titre), AAV_8-hSyn-COn/FOn-eYFP (#55650, 1×10^{13} GC ml^{-1} viral titre), AAVretro-hSyn-Cre (#105553, 7×10^{12} GC ml^{-1} viral titre), AAV_9-Syn-DIO-GCaMP6s (#100845, 1×10^{13} GC ml^{-1} viral titre), and AAV_8-DIO-hM4Di-mCitrine (#50455, 1×10^{13} GC ml^{-1} viral titre) viruses were purchased from Addgene. AAV constructs for AAV_8-CaMKII-eYFP (plasmid #105622), AAV_9-EF1α-DIO-ChR2-mCherry (plasmid #35508), AAV_8-EF1α-DO-NpHR3.0-eYFP (plasmid #37087), AAV_8-EF1α-DO-eYFP (plasmid #37085), AAV_8-CaMKII-oChIEF-mCherry (plasmid #51092), and AAV_8-Syn-oChIEF-mCherry (plasmid #50977) were obtained from Addgene and packaged by the Viral Core at Boston Children's Hospital (~3×10^{13} GC ml^{-1} viral titre). AAV_8-CaMKII-eArch3.0-eYFP virus (8×10^{12} GC ml^{-1} viral titre), AAV_8-EF1α-DIO-eArch3.0-eYFP (1.6×10^{13} GC ml^{-1} viral titre), and AAV_9-EF1α-DIO-eYFP (2×10^{13} GC ml^{-1} viral titre) were acquired from the University of North Carolina (UNC) at Chapel Hill Vector Core. For Cre-dependent anterograde circuit tracing, helper virus (AAV8-nef-DIO-mCherry-p2a-coUL6, 4.33×10^{13} GC ml^{-1}) and HSV virus (HSV-H129-LSL-TK-GFP dUL6, 3.8×10^{13} pfu ml^{-1}) were used. We generated the AAV_9-EF1α-DIO-SOUL-tdTomato construct and packaged this virus at the Boston Children's Hospital Viral Core (1×10^{13} GC ml^{-1} viral titre). For rabies virus-mediated transneuronal labelling, pAAV-Syn-FLEX-splitTVA-EGFP-tTA (Addgene #100798) and pAAV-TREtight-mTagBFP2-B19G (Addgene #100799)[52] were packaged in serotype 1 AAV capsids by the UNC Vector Core, with titres 8.48×10^{11} GC ml^{-1} and 6.50×10^{11} GC ml^{-1}, respectively, and combined in a 1:1 ratio by volume before injections, G-deleted EnvA-rabies-mCherry (8×10^9 GC ml^{-1} viral titre), G-deleted, mCherry-expressing rabies virus (RV-dG-mCherry, 7×10^9 GC ml^{-1} viral titre), G-deleted, GFP-expressing rabies virus (RV-dG-GFP, 7×10^9 GC ml^{-1} viral titre), and GL-deleted, Cre-expressing rabies virus (dGL-Cre, 8×10^9 GC ml^{-1} viral titre) were provided by the laboratory of I. Wickersham at Massachusetts Institute of Technology.

Mouse surgery

Mice were anaesthetized with isoflurane for stereotaxic injections. 1 mg kg^{-1} meloxicam was given as analgesic prior to incisions. Viral vectors, cholera toxin (CTB), nAChR modulators, or colchicine were injected with a glass pipette at a flow rate of 70 nl min^{-1}. The pipette was withdrawn 10 min after the end of the injection. For optical fibre implantation, single 200 µm fibre implants (Newdoon) were placed either above injection sites or terminals, and secured to the skull with two jewellery screws, adhesive cement (C&B Metabond), and dental cement. Mice were given 1–2 mg kg^{-1} sustained-release buprenorphine as analgesic after surgeries and allowed to recover for at least 2 weeks before behavioural experiments. All injection sites were verified histologically. As criteria, we only included mice with virus expression and fibre implantations limited to the targeted regions. Stereotaxic coordinates for injections/implantations were: PF (300 nl): anteroposterior (AP) −2.18 mm, mediolateral (ML) ±0.7 mm, dorsoventral (DV) −3.25 mm, CPu (400 nl): AP 0.3 mm, ML ±2.5 mm, DV −3.25 mm, STN (300 nl): AP −1.56 mm, ML ±1.4 mm, DV −4.8 mm, NAc (250 nl): AP 1.1 mm, ML ±1.25 mm, DV −4.3 mm, GP (350 nl): AP −0.46 mm, ML ±1.9 mm, DV −4 mm, and SNr (380 nl): AP −3.08 mm, ML ±1.5 mm, DV −4.8 mm. For 3-site CPu injections, coordinates were: CPu_1 (350 nl): AP 1.34 mm, ML ±1.5 mm, DV −3.25 mm, CPu_2 (350 nl): AP 0.62 mm, ML ±1.75 mm, DV −3.5 mm, and CPu_3 (350 nl): AP 0.3 mm, ML ±2.5 mm, DV −3.25 mm. For intracerebroventricular injection of colchicine (400 nl), the target coordinate was: AP −1.56 mm, ML ±2.5 mm, DV −4 mm. To characterize neuronal populations of PF based on downstream projection targets, we used CTB conjugated to Alexa-488, Alexa-555, or Alexa-633 diluted in PBS at a final concentration of 1% wt vol^{-1}. Mice were perfused for histology six days after CTB injections. For tracing experiments using different Cre mouse lines, AAV-FLEX^{loxP}-TVA-GFP-Rabies glycoprotein was injected unilaterally in CPu, STN, or NAc. One week later, G-deleted EnvA-rabies–mCherry was injected in CPu, STN, orNAc at the same coordinates. Six days after the second virus injection, mice were perfused for histology and imaging. Neurons that expressed both GFP (from helper virus) and mCherry (from rabies virus) were defined as starter cells. To label PF_{CPu}, PF_{STN} and PF_{NAc} neurons for ex vivo recordings, RV-dG-GFP was injected in CPu, STN or NAc, respectively. Slice recordings were performed four days after injections. For DREADDs-based neuronal inhibition during behaviour, PF subpopulations were labelled by injecting a retrograde RVdGL-Cre virus in CPu, STN or NAc combined with a Cre-dependent hM4Di-mCherry virus in PF. mCherry control mice received a Cre-dependent mCherry virus in PF in place of the hM4Di virus. DREADDs-based inhibition of *Pvalb*$^+$ or *Vglut2*$^+$ STN neurons used a Cre-dependent hM4Di virus injected into STN of *Vglut2-cre* or *Pvalb-cre* mice. For ex vivo recordings from D1 or D2 MSNs in CPu that receive PF input, ChR2-mCherry virus was injected in PF of D2-eGFP mice. For ex vivo recordings from *Pvalb*$^+$ or *Vglut2*$^+$ neurons in STN that receive PF input, ChR2-eYFP virus was injected in PF and Cre-dependent mCherry virus was injected into STN of *Pvalb-cre* mice. To visualize *Vglut2*$^+$ or *Pvalb*$^+$ neurons, Cre-dependent mCherry virus was injected into STN of *Vglut2-cre* or *Pvalb-cre* mice. For HSV-based anterograde tracing, a Cre-dependent HSV system was injected into STN of *Pvalb-cre* mice, resulting in HSV-GFP labelling in downstream neurons. For CPu manipulation studies in PD mice, PD mice were generated by injecting retrograde RVdGL-Cre in CPu, Cre-dependent hM4Di-mCherry (PD_{hM4Di}) or Cre-dependent mCherry (PD_{mCh}) in PF, and 6-OHDA in SNc. WT_{mCh} mice were generated by injecting retrograde RVdGL-Cre in CPu, Cre-dependent mCherry in PF, and saline in SNc. During these CPu manipulations in PD mice, at baseline, mice received saline injections 40 min before the test. For ex vivo recordings from the PF→STN

circuit in rescued PD mice, oChIEF–mCherry virus was injected in PF and Cre-dependent GFP virus into STN of PD model mice using *Pvalb-cre* mice. For ex vivo recordings from *D1*/*D2* in NAc that receive PF input, oChIEF–mCherry virus were injected into PF of D2-eGFP control and PD model mice. For ex vivo recordings that tested the effect of nAChR manipulations on the PF→CPu circuit in PD mice, oChIEF–mCherry virus was injected in PF and 6-OHDA in SNc of wild type mice. For ex vivo recordings that tested the effect of nAChR manipulations on the PF→NAc circuit in PD mice, oChIEF–mCherry virus was injected in PF and 6-OHDA in SNc of D2-eGFP mice. For AMPA/NMDA ratio recordings of the PF→STN circuit after rotarod in PD mice treated with a nAChR agonist, oChIEF–mCherry virus was injected in PF and Cre-dependent GFP virus into STN of PD model mice using *Pvalb-cre* mice. For nAChR manipulations without/with the chemogenetic inhibition of *Pvalb*$^{+}$ STN neurons during rotarod, Cre-dependent hM4Di virus was injected in STN and 6-OHDA in SNc of *Pvalb-cre* mice.

Macaque surgery

All neurosurgical procedures were performed using sterile methods while the subject was anaesthetized. For general anaesthesia, monkeys were administered atropine (0.05 mg kg^{-1}, intramuscular) to decrease bronchial secretions before giving ketamine (15 mg kg^{-1}, intramuscular), and then propofol (6 mg/kg, intravenously) was given to maintain anaesthesia. The anaesthesia level was adjusted to eliminate movement as assessed by toe pinches. Corneal reflexes were consistently absent. The subject was placed on a standard operating table with constant heating and the head of the subject was rigidly fixed on a stereotaxic frame (KOPF, 1430). Electrocardiography, heart rate, oxygen saturation (SpO_2) (range 95-100%) and rectal temperature (37.5–38.5 °C) were continuously monitored by a physiological monitor (Mindray, uMEC7). Coordinates for virus injection were guided by T1-weighted, magnetization prepared rapid gradient echo structural images (3T Tim Trio scanner, Siemens), and the standard monkey atlas. AAVretro-hSyn-mCherry was injected in nine sites covering the whole SNr, and a total volume of 27 µl virus was unilaterally injected in the SNr at the speed of 300 nl min^{-1}.

Mouse model of PD

6-OHDA injections were performed using the same methods as those for virus injections. 400 nl of 6-OHDA (3 mg ml^{-1}, Sigma) dissolved in sterile saline (0.9%) containing ascorbic acid (0.2%) was injected in the following coordinates: (SNc) AP −3.08 mm, ML ±1.2 mm, DV 4.5 mm. Control mice were injected with 400 nl of vehicle (i.e., saline with 0.02% ascorbic acid). A premedication of desipramine (25 mg kg^{-1}, Sigma) was administered to mice prior to injections of 6-OHDA, in order to increase the selectivity of 6-OHDA-induced lesions. Mice were supplemented with DietGel ($ClearH_2O$) for one-week post-surgery. All staining and behavioural experiments were performed at least 14 days following surgery, when the amount of dopamine depletion (based on immunostaining) was maximal and stable.

Brain slice preparation

Mice (8–12 weeks old) were anaesthetized with isoflurane, decapitated, and their brains were quickly removed. For AMPA/NMDA ratio recordings, coronal slices (300 µm thickness) were prepared in an oxygenated cutting solution at 4°C using a vibratome (Leica). The cutting solution contained (in mM): 30 NaCl, 4.5 KCl, 1.2 NaH_2PO_4, 194 sucrose, 26 $NaHCO_3$, 10 D-glucose, 0.2 $CaCl_2$, and 8 $MgSO_4$, saturated with 95% O_2–5% CO_2 (pH 7.3, osmolarity of 350 mOsm). Slices were recovered in ACSF at 33°C (±0.5 °C) for 15 min and then kept at room temperature for 1 h before recordings. ACSF contained (in mM): 119 NaCl, 2.3 KCl, 2.5 $CaCl_2$, 1.3 $MgSO_4$, 26.2 $NaHCO_3$, 1 NaH_2PO_4 and 11 D-glucose, saturated with 95% O_2, 5% CO_2 (pH 7.3, osmolarity of 300 mOsm). For all other recordings, brains were quickly removed and placed in ice-cold ACSF consisting of (in mM): 125 NaCl, 3 KCl, 1.25 NaH_2PO_4, 2 $MgSO_4$, 2 $CaCl_2$, 25 $NaHCO_3$ and 10 D-glucose. Slices were stored for 30 min at 33°C (±0.5 °C) and then kept at room temperature until recordings.

Ex vivo electrophysiological recordings

Whole cell recordings in current clamp- or voltage clamp-mode were performed using an IR-DIC microscope (Olympus) with a water immersion 40× objective (NA 0.8), equipped with four automatic manipulators (Luigs and Neumann), a CCD camera (Hamamatsu), and Clampex 10.7 software. For all recordings, borosilicate glass pipettes were fabricated (Sutter Instrument) with resistances of 3.5 to 5 MΩ. The AMPA/NMDA ratio measurements were performed by adding 100 µM picrotoxin (Tocris) in the extracellular solution, and voltage clamp recordings were performed using the following intracellular solution (in mM): 120 caesium methansulfonate, 10 HEPES, 1.1 EGTA, 5 NaCl, 1.1 TEA-Cl, 4 Mg-ATP, 0.3 Na-GTP, 4 QX314, and 0.5% biocytin. The osmolarity of this intracellular solution was 298 mOsm and the pH was 7.2. AMPA/NMDA ratio is defined as the ratio of the EPSC peak at −70 mV to the EPSC magnitude at +40 mV (50 ms following stimulation). For other recordings, pipettes were filled with the following intracellular solution (in mM): 110 potassium gluconate, 40 KCl, 10 HEPES, 3 ATP, 0.5 GTP, 0.2 EGTA, and 0.5% biocytin. The osmolarity of this intracellular solution was 290 mOsm and the pH was 7.25. For light-induced synaptic current (eEPSCs) recordings, to avoid contamination with IPSCs, neurons were clamped at −70 mV, which is close to the chloride current reversal potential in our intracellular solution protocol. ACSF with the AMPA receptor blocker CNQX (10 µM, Tocris) or $GABA_A$ receptor blocker picrotoxin (100 µM) was perfused onto the GP or SNr-containing slices to pharmacologically examine the postsynaptic current receptor type. The monosynaptic nature of PF→CPu, PF→STN, and PF→NAc circuits were confirmed by sequential bath application of 1 µM TTX, 100 µM 4AP, and then 10 µM CNQX. A series of 500 ms suprathreshold currents were used to quantify the excitability with holding at −55 mV for PF neurons, and −70 mV for STN. Membrane time constant (tau) was measured with a single exponential fit of the voltage deflection produced by a small hyperpolarizing current injection from the holding potential (−70 mV). Input resistance (R_{in}) was calculated as the slope of linear fits of current-voltage plots generated from a series of increasing current injection steps. Shape parameters were measured from the first action potential with 200 ms current injection (from a holding potential of −70 mV). Recordings were amplified using up to two dual channel amplifiers (Molecular Devices), filtered at 2 kHz, digitized (20 kHz), and acquired through an ADC/DAC data acquisition unit (Instrutech) running on Igor Pro (Wavemetrics). Access resistance (RA) was monitored throughout the duration of the experiment, and data acquisition was suspended whenever RA was beyond 20 MΩ. Optogenetic stimulation was achieved through Polygon400 (Mightex) with built-in LED sources (470, 570 and 600 nm). Light power on the sample was 20 mW mm^{-2} except for recordings reported in Fig. 1d, which employed a range of intensities from 0-30 mW mm^{-2} in 5 mW steps. Also, in Fig. 1d, all three PF circuits (i.e., PF→CPu, PF→STN, PF→NAc) were examined from each individual virus-expressing mouse. To test ChR2 expression, slices were stimulated with 5 Hz blue light pulses. To test eArch function, continuous yellow light was delivered to the slices. To test SOUL function, a 2 s blue light pulse was delivered for activation followed by a delay and then a 2 s orange light pulse was delivered for inactivation. To test synaptic connections, slices were stimulated with a single light pulse of 5 ms, repeated 10 times every 5 s, after which the average response was computed. Optical HFS protocol: baseline AMPA/NMDA ratio was acquired before the onset of the HFS protocol (100 blue light pulses of 2 ms each at a frequency of 100 Hz, repeated 5 times every 3 min) and the effect on synaptic strength was recorded. To test the effect of different molecular targets on synaptic plasticity in the PF→STN circuit of PD model mice, PNU282987[42] (1 µM, catalogue no. P6499, Sigma), DAMGO[41] (30 µM, catalogue no. E7384, Sigma), SNP[53] (10^{-4} M, catalogue no. 1614501, Sigma), and AG1478[54] (5 µM, catalogue no. T4182, Sigma)

were bath applied throughout the recordings. To test the effect of an α6-nAChR antagonist on PF→CPu circuit strength in PD model mice, evoked EPSCs of PF→CPu circuit was measured before and after bath application of α-Ctx MII[44] (100 nM, catalogue no. 1340, Tocris). To test the effect of different molecular targets on the strength of PF inputs to *Drd1*$^+$ neurons in NAc in PD model mice, evoked EPSCs of PF→NAc circuit was measured before and after bath application of epibatidine[55] (1 μM, catalogue no. E1145, Sigma), UB165[56] (1 μM, catalogue no. 1348, Tocris), CC4[57] (10 μM, catalogue no. 5236, Tocris), and PNU282987[42] (1 μM, catalogue no. P6499, Sigma).

In vivo genome editing

CRISPR-mediated in vivo genome editing experiments were performed as previously described[43]. In brief, single guide RNA (sgRNA) candidates targeting *Chrna6*, *Chrna7*, and *Chrnb2* with high specificity and high efficiency were computationally identified from sgRNA libraries for genome-wide CRISPR knockout screening. Three U6-sgRNA(FE) gene fragments with the F+E tracrRNA backbone were synthesized by Integrated DNA Technologies (sequences are provided below, spacer sequences are capitalized). These fragments were cloned into the pX552-mCherry plasmid (EGFP in pX552 plasmid was replaced with mCherry, pX552 was obtained from Addgene, plasmid #60958) by Gibson assembly (NEB E2621X) to construct pX552-3xsgRNA(FE)-mCherry. These constructs were functionally validated in Neuro2A cells. The AAV vector was serotyped with AAV_9 coat proteins and packaged in house (~8×10^{12} genome copy (GC) ml^{-1} viral titres). Each sgRNA AAV was combined with a Cre-dependent *SpCas9* AAV to restrict manipulations to Cre$^+$ neurons (that is, using *Pvalb-cre* mice for *Chrna7* knockdown in STN *Pvalb*$^+$ cells, D1-Cre mice for *Chrnb2* knockdown in NAc *Drd1*$^+$ cells, mice with AAVretro-Cre injections in CPu for *Chrna6* knockdown in PF_{CPu} neurons). The AAV-DIO-SpCas9 plasmid was serotyped with AAV_9 coat proteins and packaged by the Viral Core at Boston Children's Hospital (2×10^{13} GC ml^{-1} viral titre). For these in vivo genome editing experiments, a 1:1 mix of AAV_9-sgRNA-mCherry:AAV_9-DIO-SpCas9 was injected into the target brain regions. Target gene knockdown was validated by FISH staining.

U6-sgChrna6-1(FE) sequence: agtggccaactccatcactaggggttcctgcggccgcacgcgtaaggtcgggcaggaagagggcctatttcccatgattccttcatatttgcatatacgatacaaggctgttagagagataattagaattaatttgactgtaaacacaaagatattagtacaaaatacgtgacgtagaaagtaataatttcttgggtagtttgcagttttaaaattatgttttaaaatggactatcatatgcttaccgtaacttgaaagtatttcgatttcttggctttatatatcttgtggaaaggacgaaacaccgCAACCGCTTCATCCGGCCGGgtttaagagctatgctggaaacagcatagcaagtttaaataaggctagtccgttatcaacttgaaaaagtggcaccgagtcggtgctttttttcccagtcacgacgttgtaaaacgacggccagtgagcgcgcgtaatacgactcactatagg.

U6-sgChrna6-2(FE) sequence: cccagtcacgacgttgtaaaacgacggccagtgagcgcgcgtaatacgactcactataggaaggtcgggcaggaagagggcctatttcccatgattccttcatatttgcatatacgatacaaggctgttagagagataattagaattaatttgactgtaaacacaaagatattagtacaaaatacgtgacgtagaaagtaataatttcttgggtagtttgcagttttaaaattatgttttaaaatggactatcatatgcttaccgtaacttgaaagtatttcgatttcttggctttatatatcttgtggaaaggacgaaacaccgCTTTAAGAGCTCCTGCCCAAgtttaagagctatgctggaaacagcatagcaagtttaaataaggctagtccgttatcaacttgaaaaagtggcaccgagtcggtgctttttttagcggataacaatttcacacaggaaacagctatgaccatgattacgccaagcgcgc.

U6-sgChrna6-3(FE) sequence: agcggataacaatttcacacaggaaacagctatgaccatgattacgccaagcgcgcaaggtcgggcaggaagagggcctatttcccatgattccttcatatttgcatatacgatacaaggctgttagagagataattagaattaatttgactgtaaacacaaagatattagtacaaaatacgtgacgtagaaagtaataatttcttgggtagtttgcagttttaaaattatgttttaaaatggactatcatatgcttaccgtaacttgaaagtatttcgatttcttggcttatatatcttgtggaaaggacgaaacaccgAGGTTGATGGTGTAAAACATgtttaagagctatgctggaaacagcatagcaagtttaaataaggctagtccgttatcaacttgaaaaagtggcaccgagtcggtgctttttttctagactgcagagggccctgcgtatgagtgcaagtgggttttaggaccaggatgaggcggggtg.

U6-sgChrna7-1(FE) sequence: agtggccaactccatcactaggggttcctgcggccgcacgcgtaaggtcgggcaggaagagggcctatttcccatgattccttcatatttgcatatacgatacaaggctgttagagagataattagaattaatttgactgtaaacacaaagatattagtacaaaatacgtgacgtagaaagtaataatttcttgggtagtttgcagttttaaaattatgttttaaaatggactatcatatgcttaccgtaacttgaaagtatttcgatttcttggctttatatatcttgtggaaaggacgaaacaccgCAAGACGTTGGTGTGGAATGgtttaagagctatgctggaaacagcatagcaagtttaaataaggctagtccgttatcaacttgaaaaagtggcaccgagtcggtgctttttttagcggataacaatttcacacaggaaacagctatgaccatgattacgccaagcgcgc.

U6-sgChrna7-3(FE) sequence: agcggataacaatttcacacaggaaacagctatgaccatgattacgccaagcgcgcaaggtcgggcaggaagagggcctatttcccatgattccttcatatttgcatatacgatacaaggctgttagagagataattagaattaatttgactgtaaacacaaagatattagtacaaaatacgtgacgtagaaagtaataatttcttgggtagtttgcagttttaaaattatgttttaaaatggactatcatatgcttaccgtaacttgaaagtatttcgatttcttggctttatatatcttgtggaaaggacgaaacaccgGATCATCGTGGGCCTCTCAGgtttaagagctatgctggaaacagcatagcaagtttaaataaggctagtccgttatcaacttgaaaaagtggcaccgagtcggtgctttttttctagactgcagagggccctgcgtatgagtgcaagtgggttttaggaccaggatgaggcggggtg.

U6-sgChrnb2-1(FE) sequence: agtggccaactccatcactaggggttcctgcggccgcacgcgtaaggtcgggcaggaagagggcctatttcccatgattccttcatatttgcatatacgatacaaggctgttagagagataattagaattaatttgactgtaaacacaaagatattagtacaaaatacgtgacgtagaaagtaataatttcttgggtagtttgcagttttaaaattatgttttaaaatgactatcatatgcttaccgtaacttgaaagtatttcgatttcttggctttatatatcttgtggaaaggacgaaacaccgACGGATCAGCTTGTTATAGCgtttaagagctatgctggaaacagcatagcaagtttaaataaggctagtccgttatcaacttgaaaaagtggcaccgagtcggtgctttttttcccagtcacgacgttgtaaaacgacggccagtgagcgcgcgtaatacgactcactatagg.

U6-sgChrnb2-2(FE) sequence: cccagtcacgacgttgtaaaacgacggccagtgagcgcgcgtaatacgactcactataggaaggtcgggcaggaagagggcctatttcccatgattccttcatatttgcatatacgatacaaggctgttagagagataattagaattaatttgactgtaaacacaaagatattagtacaaaatacgtgacgtagaaagtaataatttcttgggtagtttgcagttttaaaattatgttttaaaatggactatcatatgcttaccgtaacttgaaagtatttcgatttcttggctttatatatcttgtggaaaggacgaaacaccgGCGAGGTGATGAGTACGCAGgtttaagagctatgctggaaacagcatagcaagtttaaataaggctagtccgttatcaacttgaaaaatggcaccgagtcggtgctttttttagcggataacaatttcacacaggaaacagctatgaccatgattacgccaagcgcgc.

U6-sgChrnb2-3(FE) sequence: agcggataacaatttcacacaggaaacagctatgaccatgattacgccaagcgcgcaaggtcgggcaggaagagggcctatttcccatgattcctcatatttgcatatacgatacaaggctgttagagagataattagaattaatttgactgtaaacacaaagatattagtacaaaatacgtgacgtagaaagtaataatttcttgggtagtttgcagttttaaaattatgttttaaaatggactatcatatgcttaccgtaacttgaaagtatttcgatttcttggctttatatatcttgtggaaaggacgaaacaccgTGTGCGTGGTAGGCGAACGGgtttaagagctatgctggaaacagcatagcaagtttaaataaggctagtccgttatcaacttgaaaaagtggcaccgagtcggtgctttttttctagactgcagagggccctgcgtatgagtgcaagtgggttttaggaccaggatgaggcggggtg.

Behaviour assays

Experiments were conducted during the light cycle (07:00 to 19:00). Mice were randomly assigned to experimental groups for specific behaviours immediately after surgery. Mice were habituated to investigator handling for 1–2 min on 3 consecutive days. Handling took place in the holding room where the mice were housed. Prior to each handling session, mice were transported by wheeled cart to and from the vicinity of the behaviour rooms to habituate them to the journey. All behaviour experiments were analysed blind to experimental group. Given behavioural variability, initial assays were performed using a minimum of 7–10 mice per group to ensure adequate power for any observed differences. Following behavioural protocols, brain sections were prepared to confirm efficient viral labelling in target areas. Mice

lacking adequate labelling were excluded prior to behaviour quantification. For oChIEF-mediated stimulation or eArch, NpHR-mediated inhibition experiments, optical fibres were connected to a 473 nm blue laser or a 570 nm yellow laser, respectively. For SOUL-mediated stimulation experiments, optical fibres were connected to a 473 nm blue laser for activation and a 600 nm orange laser for inactivation. Laser power was adjusted to 10-15 mW before each experiment. oChIEF-based optical LTP was induced with continuous 20 Hz blue light during trials combined with 100 Hz blue light (5 trains of 100 pulses, repeated 5 times every 3 min) between trials on the first day of training. For the forced swim and tail suspension tests, SOUL in PF thalamus was activated using a 60 s blue laser light source (activation) connected to the skull just before the start of the experiment, after this, optical fibres were disconnected, and following the completion of the behaviour mice were reconnected via optical fibres to a 90 s orange laser light source (inactivation). For sucrose preference tests, SOUL in PF thalamus was activated similar to the forced swim and tail suspension tests, except that mice remained plugged in to the optical fibres for the entire duration of the behaviour and SOUL activation was performed for 5 min, followed by 5 min of inactivation, repeated for the session. For the PD_{SOUL} control group, orange light was delivered in vivo immediately after blue light application. For optogenetic and chemogenetic inhibition experiments on the rotarod setup, yellow light or C21 were applied on the first training day. For hM4Di-mediated chemogenetic inhibition experiments, compound 21 (C21, Hello Bio) was injected intraperitoneally 40 min before each behaviour test, at a dose of 2 mg kg^{-1}. For activation of α7-nAChRs in rotarod learning, PNU282987 was applied intraperitoneally (1.5 mg kg^{-1}) or locally infused into bilateral STN (1 μM, 250 nl per hemisphere) 40 min before training on the first day. For the inactivation of α6-nAChRs in open field tests, α-Ctx MII (100 nM, 1 μl per hemisphere, Tocris) was locally infused into bilateral CPu 40 min before behaviour. For the activation of β2-nAChRs in depression-like behaviours, epibatidine (1 μM, 250 nl per hemisphere, Sigma) was locally infused into bilateral NAc 40 min before behaviours.

Open field test. Motor activity was measured in an open field arena (40 × 40 × 30 cm) for 20 min. Mice were transferred to the testing room and acclimatized for 30 min before the test session. During the testing period, lighting in the room was turned off. The apparatus was cleaned with quatricide before and between runs. Movement of each mouse in the arena was detected using an automated infrared detection system (Omnitech Digiscan, AccuScan Instruments). Raw data were extracted using Microsoft Excel. For repeated open field tests with PF_{CPu} manipulations, mice were habituated to the arena for 3 consecutive days (1 h per day) before the first test. Z-scores for fraction of time spent moving, total distance travelled, and number of movements were calculated as $z = (x_i - \overline{x})/(\sigma_x - n)$, where x_i is the value for each mouse, $\overline{x}$ is the mean value across all mice, σ_x is the standard deviation across all mice. *Z*-score for each mouse and each measure has been plotted with density clouds for each group overlaid. For distance travelled, number of movements, and moving time variables, we performed an ANOVA using group assignment (WT or PD) and time points (baseline, day 7, day 10) as predictors in a full linear model, including an interaction term between group assignment and time point. For all three variables individually, the ANOVA resulted in a significant interaction between group assignment and time point. Post hoc two-sided *t*-tests were performed between WT, PD_{mCh}, and PD_{hM4Di} groups at each time point. *P* values were corrected for multiple comparisons using the Holm-Sidak method. For distance travelled, WT_{mCh} vs PD_{hM4Di} group (Baseline: $P < 0.001$, day 7: NS, day 10: NS). For number of movements, WT_{mCh} vs PD_{hM4Di} groups (Baseline: $P < 0.01$, day 7: NS, day 10: NS). For moving time, WT_{mCh} vs PD_{hM4Di} groups (Baseline: $P < 0.01$, day 7: NS, day 10: NS). For distance travelled, PD_{mCh} vs PD_{hM4Di} group (Baseline: NS, day 7: $P < 0.01$, day 10: $P < 0.05$). For number of movements, PD_{mCh} vs PD_{hM4Di} groups (Baseline: NS, day 7: $P < 0.01$, day 10: $P < 0.01$). For moving time, PD_{mCh} vs PD_{hM4Di} groups (Baseline: NS, day 7: $P < 0.05$, day 10: $P < 0.01$).

Rotarod test. Mice were transferred to the testing room and acclimatized for 15 min before the test session. Mice were placed on the rod (Med Associates) with the apparatus set to accelerating mode (4–40 rpm). Latency to fall for each trial was automatically recorded by the apparatus. Each mouse was tested for 3 trials in a single day over 2 consecutive days, with a minimum of 15 min between trials. Raw data were recorded and analysed using Microsoft Excel. Fall latency was averaged across 3 trials within each day, and then normalized to day 1 for each mouse. For rotarod-induced STN cFos labelling or synaptic changes (measured using ex vivo electrophysiology), mice were euthanized for immunohistochemistry or slice recordings 1 h after behaviour training on day 1.

Zero maze test. The elevated zero maze apparatus had four equally divided quadrants, specifically two open and two closed arms, and the setup was elevated ~2.5 ft above the floor. Using indirect lighting, the open arms were at 60 lux and the closed arms were at 10 lux. Mice were placed in the centre of the closed arm and allowed to explore the arena for 5 min. Mouse placement was counterbalanced. Anxiety-like behaviour was assessed based on percentage of time spent in the open arms. Automated analysis was performed using the Noldus Observer software.

Forced swim test. Mice were placed in cylindrical glass beakers (12 cm in diameter, 25 cm in height) filled with water at ~25 °C, in which they could not touch the bottom of the beakers. Video recording was performed from the side view 2 min after mice were placed in the water, serving as a habituation period. Immobility time was measured for 4 min by blind manual scoring. After testing, mice were placed in a pre-warmed cage for 30 min after which they were returned to their home cages.

Tail suspension test. Mice were gently suspended using autoclaved tape to secure their tail to a horizontal bar 60 cm from the floor. We made sure that the mouse could not make any contact or climb during testing. Video recording was performed 1 min after mice were inverted and taped, serving as a habituation period. Time spent struggling was measured for 5 min by blind manual scoring.

Sucrose preference test. In the home cage, single housed mice were habituated to two identical bottles containing 1.5% sucrose solution for 2 days, followed by two identical water bottles for 1 day. Mice were water deprived for 1 day and then on the test day exposed to two bottles, one with water and the other containing 1.5% sucrose solution. The test duration was 4 h in the dark, during which we switched the bottle locations at the 2 h time point. Total consumption of water and sucrose solution was measured at the end of the session by weighing the bottles. Sucrose preference was defined as the ratio of the consumption of sucrose solution versus the consumption of both water and sucrose solution. Testing was performed over 3 consecutive days. For chemogenetic experiments, mice were injected with C21 30 min before testing.

Contextual fear conditioning test. The conditioning context was a 29 × 25 × 22 cm chamber with grid floors, dim white lighting, and scented with 0.25% benzaldehyde. All mice were conditioned (120 s exploration, one 0.65 mA shock of 2 s duration at 120 s, 60 s post-shock period, second 0.65 mA shock of 2 s duration at 180 s, 60 s post-shock period), and tested (3 min) one day later. Floors of chambers were cleaned with quatricide before and between runs. Mice were transported to and from the experimental room in their home cages using a wheeled cart.

Real-time place preference test. We placed mice in a custom-made behavioural arena (40 × 15 cm) for 10 min. We assigned one counterbalanced side of the chamber as the stimulation side (+light). We placed the mouse in the non-stimulation side (-light) at the onset of the experiment and each time the mouse crossed over to the stimulation side of the chamber, we delivered 20-Hz blue laser stimulation until the mouse crossed back into the non-stimulation side.

Cocaine-induced conditioned place preference test. The conditioned place preference (CPP) behaviour chamber was a rectangular arena (40 × 15 cm), divided into 3 quadrants (left, middle, right). The left and right quadrants were 15 cm long, while the middle quadrant was 13 cm long. The left quadrant had grid floors and a pattern (series of parallel lines) on the wall. The right quadrant had smooth polypropylene floors and a pattern (series of circles) on the wall. On day 1 (pre-exposure), mice were allowed to explore the entire arena for 30 min. Experiments showed no preference to any one quadrant. On day 2 (training), mice were confined to the left or right quadrants for 20 min following cocaine (20 mg kg^{-1}) or saline intraperitoneal administration. On days 3-7 (training continued), mice were conditioned in opposite quadrants in an alternating manner (that is, cocaine left–saline right–cocaine left, etc.) until every mouse received 3 cocaine and 3 saline pairings. For every behavioural cohort, half the mice were conditioned with cocaine in the left quadrant, while the remaining mice received cocaine in the right quadrant. On day 8, memory recall was measured by preference to the left or right quadrant (10 min). All sessions were performed with dim white lighting. Mouse behaviour, specifically position tracking and duration, was recorded using an automated infrared (IR) detection system (EthoVision XT, Noldus). The tracking software plotted heat maps for each mouse, which was averaged to create representative heat maps for each group. Raw data were extracted and analysed using Microsoft Excel. For neuronal inhibition of PF_{NAc}, we injected C21 40 min before each training session.

Fibre photometry

For in vivo imaging experiments, 250 nl of AAVretro-Cre virus was injected in CPu, STN, or NAc combined with a Cre-dependent GCaMP6s virus injected in PF (300 nl). After ~4 weeks of virus expression, an optical fibre (outer diameter of 200 μm, numerical aperture of 0.37, Inper) was implanted 200 μm above the PF injection site. Following another 1.5 weeks of recovery, imaging during behavioural paradigms was performed using the commercial Inper Fiber Photometry System (China). behaviour videos were collected using a driver-free camera, which was automatically driven by the InperStudio 3.1.1 software installed together with the Basler camera driver. Calcium signal acquisition and video recordings were synchronized with the same start/stop button in the InperStudio software. Each group experienced 3 different behaviours in the following order: open field (one 10 min session), rotarod (3 trials on one day), and tail suspension (one 5 min session). 470 and 405 nm LEDs were used for GCaMP6s excitation and control signals, respectively. Power of the 470 nm LED was between 10–20 μW, and the 405 nm LED power was adjusted to approximately match the GCaMP fluorescence signal. Emitted signals were captured at 120 Hz with alternating pulses of 470 and 405 nm light resulting in frame rates of 60 Hz for GCaMP and control signals. Calcium activity data were analysed using the InperDataProcess 3.1.1 software. To account for the effect of photobleaching caused by prolonged recording sessions, calcium signals were baseline corrected using the InperDataProcess software. Polynomial least squared regression was used to obtain the corrected calcium signals. Fitting the original data through the polynomial method generated a regression line, and signal correction was then conducted according to the predicted values from the regression line. In order to minimize motion-related artifacts, calcium signals were motion corrected using the InperDataProcess software. The 405 nm signal was scaled using least-squares regression and then subtracted from the 470 nm signal to generate the corrected 470 nm signal.

Event markers were manually labelled in the software using the synchronized behavioural videos. For the open field test, immobility start was defined by at least 2 s of complete immobility and immobility end was defined by at least 2 s of complete immobility followed by at least 2 s of movement. For the onset of immobility, we detected 75 epochs (10 + 13 + 20 + 13 + 19 from 5 mice) for the PF_{CPu} group, 59 epochs (12 + 14 + 9 + 14 + 10 from 5 mice) for the PF_{STN} group, and 68 epochs (14 + 14 + 13 + 13 + 14 from 5 mice) for the PF_{NAc} group. For the end of immobility, we detected 71 epochs (10 + 12 + 19 + 12 + 18 from 5 mice) for the PF_{CPu} group, 58 epochs (11 + 14 + 9 + 14 + 10 from 5 mice) for the PF_{STN} group, and 63 epochs (13 + 13 + 12 + 12 + 13 from 5 mice) for the PF_{NAc} group. For the rotarod test, mice were placed on the rod rotating at a constant speed of 4 rpm during habituation. Acceleration start was defined as the initiation of the rotarod test. As the acceleration of the rod increased from 4 rpm, the time point at which mice dropped from the rod was defined as the end of acceleration. Each group experienced three trials on the same day. Thus, 15 epochs with 3 trials per mouse were recorded for both onset and end of acceleration for each PF population. For the tail suspension test, struggling start was defined as at least 2 s of struggling followed by at least 2 s of complete immobility. Struggling end was defined as at least 2 s of immobility followed by at least 2 s of struggling. For the onset of struggling, we detected 45 epochs (9 + 12 + 9 + 7 + 8 from 5 mice) for the PF_{CPu} group, 50 epochs (12 + 5 + 11 + 13 + 9 from 5 mice) for the PF_{STN} group, and 52 epochs (14 + 9 + 13 + 9 + 7 from 5 mice) for the PF_{NAc} group. For the end of struggling, we detected 45 epochs (9 + 12 + 9 + 7 + 8 from 5 mice) for the PF_{CPu} group, 52 epochs (12 + 5 + 12 + 14 + 9 from 5 mice) for the PF_{STN} group, and 52 epochs (13 + 8 + 14 + 10 + 7 from 5 mice) for the PF_{NAc} group.

$\Delta F/F$ was calculated as the relative change of the GCaMP signal ($F(t)$) during the designated epochs as compared to the mean value of the GCaMP signal during baseline (F_0): $\Delta F/F = \frac{F(t) - F_0}{F_0}$. For area under the curve (AUC) calculations, we used the following. For the open field test, baseline was set as a 4 s period prior to the onset of immobility (onset) and a 4 s period after the end of immobility (end); for the rotarod test, baseline was set as a 2 s period prior to the onset of acceleration (onset) and a 2 s period after the end of acceleration (end); for the tail suspension test, baseline was set as a 2 s period prior to the onset of struggling (onset) and a 2 s period after the end of struggling (end). AUC was calculated during the 4 s period after the onset or the 4 s period before the end of each epoch for open field, rotarod, and tail suspension tests. For the correlation plot of GCaMP intensity and mouse velocity in the open field test, baseline was calculated for each mouse using the averaged GCaMP signal during the immobile period (velocity = 0 cm/s detected with ANY-maze 6.35 software). For the correlation plot of GCaMP intensity and mouse velocity in the rotarod test, baseline was calculated for each mouse using the GCaMP signal 2 s prior to the onset of acceleration.

Statistics and reproducibility

All experiments and data analyses were conducted blind to experimental groups. The number of replicates (n) is indicated in figure legends and refers to the number of experimental subjects independently treated in each experimental condition. Data are presented as mean values accompanied by SEM. Statistical comparisons were performed using Microsoft Excel with the Statplus plug-in, Python, and Prism 6 software. One-way ANOVA followed by Bonferroni post hoc tests, two-way ANOVA with repeated measures followed by Bonferroni post hoc tests, two-way ANOVA followed by post hoc two-sided t-tests, unpaired t-test and paired t-test were used to test for statistical significance when appropriate. No statistical methods were used to pre-determine sample sizes. Statistical significance threshold was set at $\alpha = 0.05$ (NS, $P > 0.05$; $^*P < 0.05$; $^{**}P < 0.01$; $^{***}P < 0.001$). P values are

provided in all figure legends. Experiments were replicated in at least two independent batches that yielded consistent results.

Reporting summary

Further information on research design is available in the Nature Research Reporting Summary linked to this paper.

Data availability

Reagents are available from the corresponding authors upon reasonable request. Source data are provided with this paper.

51. Kondoh, K. et al. A specific area of olfactory cortex involved in stress hormone responses to predator odours. *Nature* **532**, 103–106 (2016).
52. Liu, K. et al. Lhx6-positive GABA-releasing neurons of the zona incerta promote sleep. *Nature* **548**, 582–587 (2017).
53. Makara, J. K. et al. Involvement of nitric oxide in depolarization-induced suppression of inhibition in hippocampal pyramidal cells during activation of cholinergic receptors. *J. Neurosci.* **27**, 10211–10222 (2007).
54. Pitcher, G. M. et al. Schizophrenia susceptibility pathway neuregulin 1-ErbB4 suppresses Src upregulation of NMDA receptors. *Nat. Med.* **17**, 470–478 (2011).
55. Matsuyama, S. & Matsumoto, A. Epibatidine induces long-term potentiation (LTP) via activation of α4β2 nicotinic acetylcholine receptors (nAChRs) in vivo in the intact mouse dentate gyrus: both α7 and α4β2 nAChRs essential to nicotinic LTP. *J. Pharmacol. Sci.* **93**, 180–187 (2003).
56. Fu, W. & Jhamandas, J. H. Beta-amyloid peptide activates non-alpha7 nicotinic acetylcholine receptors in rat basal forebrain neurons. *J. Neurophysiol.* **90**, 3130–3136 (2003).
57. Sala, M. et al. CC4, a dimer of cytisine, is a selective partial agonist at α4β2/α6β2 nAChR with improved selectivity for tobacco smoking cessation. *Br. J. Pharmacol.* **168**, 835–849 (2013).

Acknowledgements We thank X. Gong and J. Ting for generating the Cre-dependent SOUL construct; C. Wang for viral packaging; M. Fleishman, B. Clear, J. Kim, and H. Zaniewski for technical assistance; Z. Yang and W. Chen for data analysis; and all members of the Feng laboratory for their support. The J. Douglas Tan Fellowship supported Y. Zhang. The Warren Alpert Distinguished Scholar Award and NIH 1K99NS125121-01 supported D.S.R. This work was supported by the Stanley Center for Psychiatric Research at the Broad Institute of MIT and Harvard, Hock E. Tan and K. Lisa Yang Center for Autism Research at MIT, James and Patricia Poitras Center for Psychiatric Disorders Research at MIT, and NIH BRAIN Initiative (U01MH114819) (to G.F.).

Author contributions Y. Zhang, D.S.R., and G.F. contributed to study design. Y. Zhang, D.S.R., T.A., C.S., M.E.S. and K.M.S. contributed to data collection and analysis. Y. Zhang, D.S.R., Y.H. and N.E.L. conducted surgeries and histological analyses. Y. Zhu and X.-M.L. conducted all in vivo calcium imaging experiments. Y.C., J.D. and Z.L. conducted all macaque experiments. H.A.S. and I.R.W. provided all rabies viruses. K.B.F. and E.M.C. provided the anterograde HSV viruses. Y. Zhang, D.S.R., and G.F. wrote the paper. All authors discussed and commented on the manuscript.

Competing interests The authors declare no competing interests.

Additional information

Supplementary information The online version contains supplementary material available at https://doi.org/10.1038/s41586-022-04806-x.

Correspondence and requests for materials should be addressed to Ying Zhang, Dheeraj S. Roy or Guoping Feng.

Peer review information *Nature* thanks Tianyi Mao and the other, anonymous, reviewers for their contribution to the peer review of this work.

Reprints and permissions information is available at http://www.nature.com/reprints.

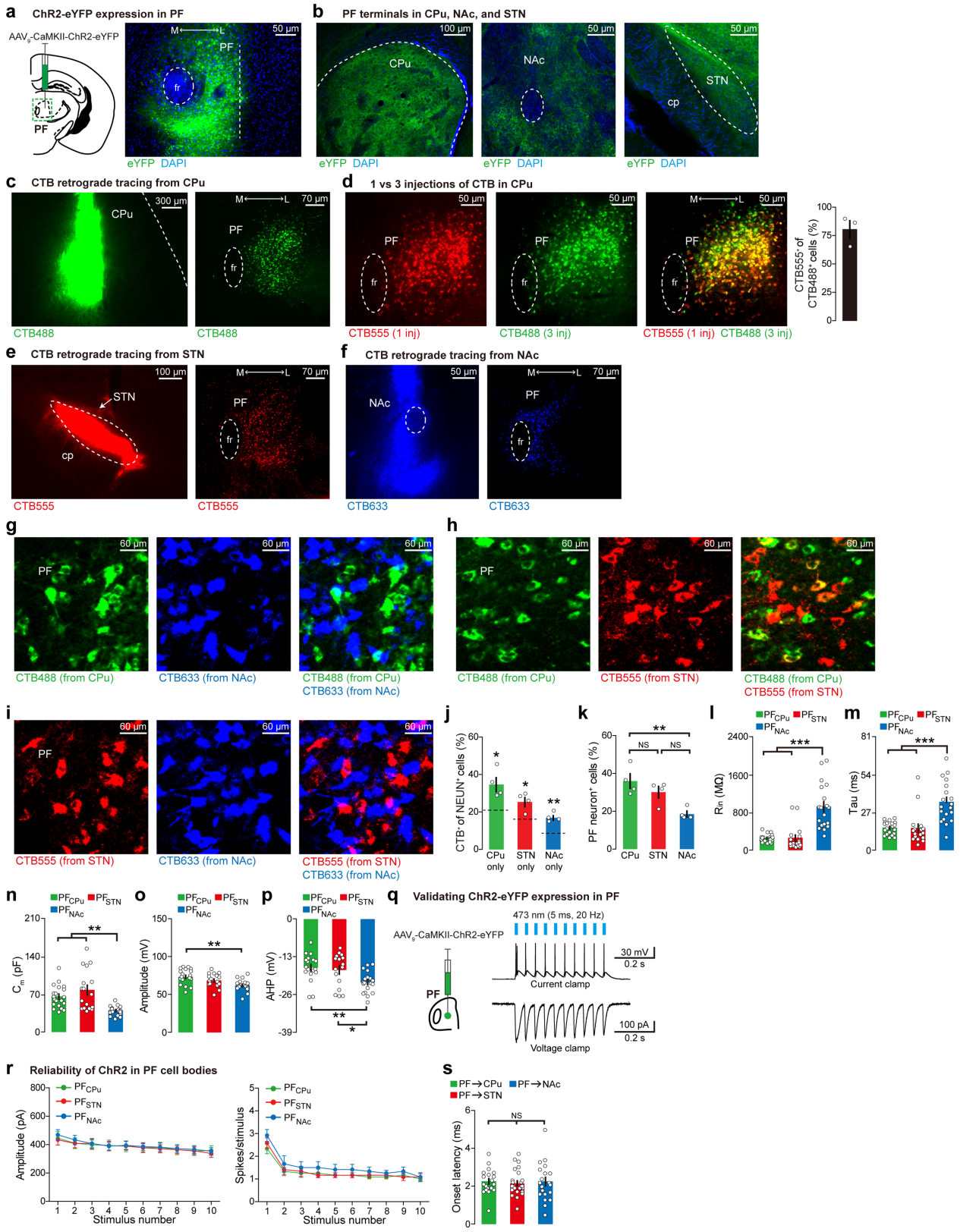

Extended Data Fig. 1 | See next page for caption.

Extended Data Fig. 1 | PF projections to CPu, NAc, and STN, and PF_{NAc} neurons have distinct electrophysiological properties as compared to PF_{CPu} and PF_{STN} populations. a-b, Anterograde tracing from mouse PF, ChR2-eYFP virus injection site (**a**), and PF terminals in CPu, NAc, and STN (**b**). DAPI staining (blue). **c**, CTB488 injection site in CPu (left) along with corresponding upstream PF labeling (lower magnification image relative to Fig. 1a, right). **d**, Upstream labeling in PF with 1 (CTB555) vs. 3 (CTB488) injections in CPu. 80.5% of CPu-projecting PF neurons (i.e., CTB488) are labeled by a single injection of CTB555 in CPu ($n = 3$ mice). **e-f**, Injection sites of CTB555 in STN (left) (**e**) and CTB633 in NAc (left) (**f**) along with corresponding upstream PF labeling images (lower magnification relative to Fig. 1a, both right panels). **g-i**, Representative high magnification images from Fig. 1a, showing low overlap between CPu- and NAc-projecting PF neurons (**g**), CPu- and STN-projecting PF neurons (**h**), and STN- and NAc-projecting PF neurons (**i**). **j**, Percentage of $CTB488^+$ only (CPu only), $CTB555^+$ only (STN only), and $CTB633^+$ only (NAc only) in PF. Dashed lines indicate chance level (20.49% for CPu only, 15.7% for STN only, 8.28% for NAc only) calculated using *NEUN* staining ($n = 4$ mice per group). **k**, Percentage of $NEUN^+$ PF neurons projecting to the three different targets ($n = 4$ mice per group). **l-p**, Electrophysiological properties of PF_{CPu}, PF_{NAc}, and PF_{STN} neurons, which were labeled using retrograde RV injected into CPu, NAc, and STN respectively. Input resistance (R_{in}) (**l**), membrane time constant (tau) (m), membrane capacitance (C_m) (**n**), action potential amplitude (**o**), and action potential afterhyperpolarization (AHP) amplitude (**p**) (For R_{in}, tau, and C_m, PF_{CPu}: $n = 20$ neurons (7, 7, 6), PF_{STN}: $n = 17$ neurons (6, 5, 6), PF_{NAc}: $n = 19$ neurons (6, 7, 6) from 3 mice each. For amplitude and AHP, PF_{CPu}: $n = 18$ neurons (5, 5, 8), PF_{STN}: $n = 16$ neurons (6, 5, 5), PF_{NAc}: $n = 19$ neurons (6, 7, 6) from 3 mice each). **q**, ChR2-eYFP virus was injected in PF and *ex vivo* recordings were performed at PF cell bodies to validate virus expression (left), light responses in ChR2-labeled PF neurons were evoked by a 473 nm pulse train, shown in both current and voltage clamp modes (right). **r**, Reliability of ChR2 was compared across PF populations by recording from retrogradely-labeled CTB^+ neurons that also expressed ChR2 ($n = 12$ neurons (4, 4, 4) from 3 mice for each group). **s**, Onset latency of evoked EPSCs recorded in postsynaptic neurons receiving PF input (PF→CPu: $n = 19$ neurons (7, 6, 6), PF→STN: $n = 26$ neurons (10, 9, 7), PF→NAc: $n = 20$ neurons (7, 7, 6) from 3 mice each). Data are presented as mean ± SEM; $^*P < 0.05$, $^{**}P < 0.01$, $^{***}P < 0.001$. NS, not significant. One-sample t test (**j**), one-way ANOVA followed by Bonferroni post-hoc test (**k-p**, **s**), and two-way ANOVA with repeated measures followed by Bonferroni post-hoc test (**r**). CPu only $P = 0.033$, STN only $P = 0.028$, NAc only $P = 0.006$ (**j**), $F = 8.88$, $P = 0.007$, CPu vs. STN $t = 1.4$, STN vs. NAc $t = 2.74$, CPu vs. NAc $t = 4.14$ (**k**), $F = 27.71$, $P < 0.0001$, PF_{CPu} vs. PF_{NAc} $t = 6.57$, PF_{STN} vs. PF_{NAc} $t = 6.28$ (**l**), $F = 17.48$, $P < 0.0001$, PF_{CPu} vs. PF_{NAc} $t = 5.17$, PF_{STN} vs. PF_{NAc} $t = 5.04$ (**m**), $F = 11.76$, $P < 0.0001$, PF_{CPu} vs. PF_{NAc} $t = 3.37$, PF_{STN} vs. PF_{NAc} $t = 4.69$ (**n**), $F = 7.19$, $P = 0.0018$, PF_{CPu} vs. PF_{NAc} $t = 3.78$ (**o**), $F = 6.11$, $P = 0.0042$, PF_{CPu} vs. PF_{NAc} $t = 3.26$, PF_{STN} vs. PF_{NAc} $t = 2.65$ (**p**), Amplitude: $F = 0.03$, DFn = 2, DFd = 297, $P = 0.97$, spikes/stimulus: $F = 0.68$, DFn = 2, DFd = 297, $P = 0.51$ (**r**), $F = 0.11$, $P = 0.89$ (**s**).

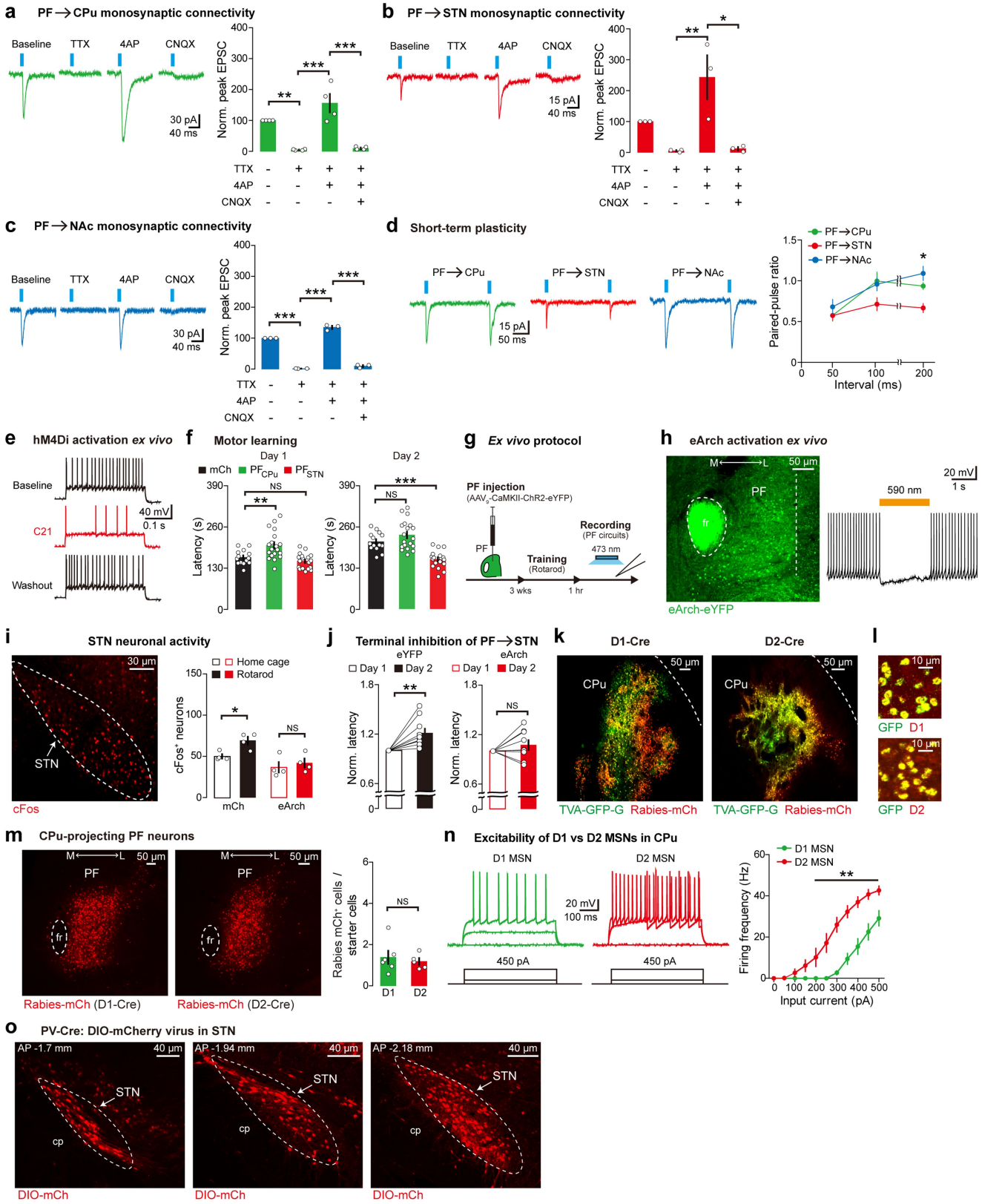

Extended Data Fig. 2 | See next page for caption.

Extended Data Fig. 2 | PF circuit electrophysiology, PF→STN terminal inhibition during motor learning, and cell type-specific tracing for the PF→CPu circuit. a-c, Representative traces and quantification of evoked EPSCs in the presence of tetrodotoxin (TTX), 4-aminopyridine (4AP), and 6-cyano-7-nitroquinovaline-2,3-dione (CNQX) for PF→CPu (**a**), PF→STN (**b**), and PF→NAc (**c**) circuits (PF→CPu: $n = 4$ neurons (2, 1, 1), PF→STN: $n = 3$ neurons (1, 1, 1), PF→NAc: $n = 3$ neurons (1, 1, 1) from 3 mice each). Norm. peak EPSC amplitude plotted. **d**, Representative traces and quantification of paired-pulse ratio (also referred to as short-term plasticity) recordings in PF circuits (PF→CPu: $n = 20$ neurons (7, 6, 7), PF→STN: $n = 23$ neurons (8, 7, 8), PF→NAc: $n = 20$ neurons (7, 6, 7) from 3 mice each). **e**, C21-induced, reversible neuronal inhibition of a PF neuron expressing hM4Di *ex vivo*, using a step current injection protocol. **f**, C21-induced inhibition of PF_{CPu} or PF_{STN} neurons during rotarod tests ($n = 14$ mCh, $n = 19$ PF_{CPu}, $n = 18$ PF_{STN} mice). **g**, Experimental protocol for AMPA/NMDA ratio recordings. CaMKII-ChR2-eYFP virus was injected in PF, 3 weeks later animals were trained on the rotarod paradigm, and 1 hr after the end of training *ex vivo* recordings were performed. **h**, CaMKII-eArch3.0-eYFP virus was injected in PF and fibers were implanted above STN. eArch-eYFP virus expression in PF (left), and light-induced neuronal inhibition *ex vivo* (right). **i**, PF→STN terminal inhibition followed by *cFos* staining in STN using home cage or rotarod mice validated effective *in vivo* terminal inhibition ($n = 4$ mice per group). cFos was stained using a 633 secondary antibody (pseudocolored red). **j**, PF→STN terminal inhibition during rotarod. *eYFP* control mice received a CaMKII-eYFP virus in PF in place of the *eArch* virus. Norm. latency plotted relative to day 1 ($n = 10$ eYFP, $n = 9$ eArch mice). **k-m**, Monosynaptic retrograde RV tracing from $D1^+$ or $D2^+$ MSNs in CPu. Images show starter cells (**k**), FISH co-staining of *GFP* with *D1* or *D2* (**l**), and corresponding PF labeling (**m**) ($n = 6$ D1-Cre, $n = 5$ D2-Cre mice). **n**, Representative traces (left) and current-frequency curves (right) of *ex vivo* recordings from $D2^-$ (putative $D1^+$) or $D2^+$ MSNs in CPu (*D1*: $n = 14$ neurons (5, 4, 5), *D2*: $n = 12$ neurons (4, 5, 3) from 3 mice each). **o**, Anterior to posterior (AP) distribution of *PV* neurons in STN. Cre-dependent mCh virus was injected into STN of PV-Cre mice. Data are presented as mean ± SEM; $^*P < 0.05$, $^{**}P < 0.01$, $^{***}P < 0.001$. NS, not significant. One-way ANOVA followed by Bonferroni post-hoc test (**a-c**, **f**), two-way ANOVA with repeated measures followed by Bonferroni post-hoc test (**d**, **n**), unpaired *t* test (**i**, **m**), and two-tailed paired *t* test (**j**). $F = 24.64$, $P < 0.0001$, Baseline vs. TTX $t = 4.56$, TTX vs. TTX + 4AP $t = 7.23$, TTX + 4AP vs. TTX + 4AP + CNQX $t = 6.99$ (**a**), $F = 9.59$, $P = 0.005$, TTX vs. TTX + 4AP $t = 4.71$, TTX + 4AP vs. TTX + 4AP + CNQX $t = 4.57$ (**b**), $F = 468.7$, $P < 0.0001$, Baseline vs. TTX $t = 22.74$, TTX vs. TTX + 4AP $t = 30.83$, TTX + 4AP vs. TTX + 4AP + CNQX $t = 28.97$ (**c**), $F = 6.41$, DFn = 2, DFd = 120, $P = 0.003$ (**d**), Day 1: $F = 11.30$, $P < 0.0001$, mCh vs. PF_{CPu} $t = 3.25$, mCh vs. PF_{STN} $t = 1.00$, Day 2: $F = 22.58$, $P < 0.0001$, mCh vs. PF_{CPu} $t = 1.70$, mCh vs. PF_{STN} $t = 4.38$ (**f**), mCh $P = 0.012$, eArch $P = 0.55$ (**i**), eYFP $P = 0.0032$, eArch $P = 0.24$ (**j**), $P = 0.61$ (**m**), $F = 28.31$, DFn = 1, DFd = 240, $P < 0.0001$ (**n**).

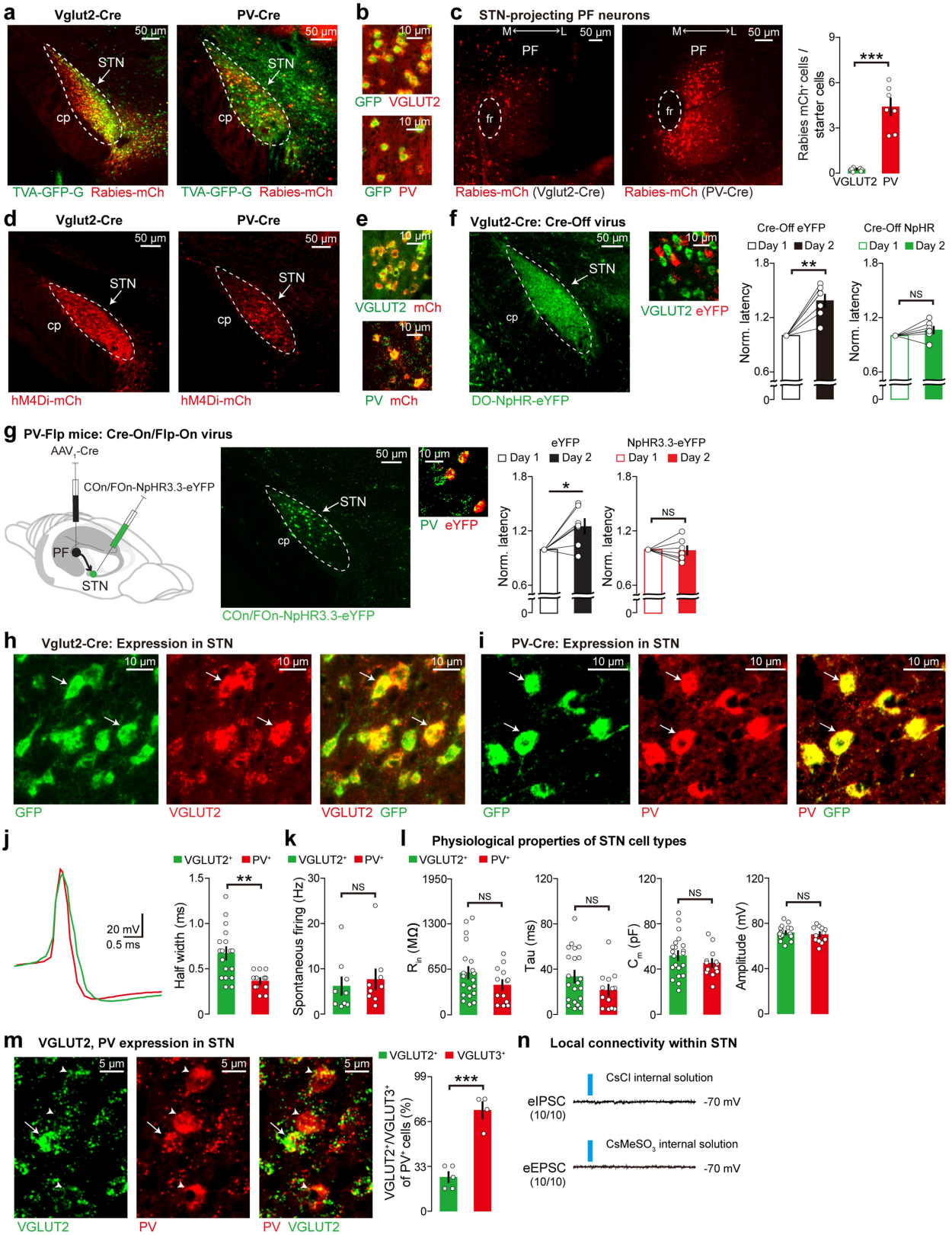

Extended Data Fig. 3 | See next page for caption.

Extended Data Fig. 3 | Cell type-specific tracing for the PF→STN circuit, and *PV*$^+$ STN neurons are critical for motor learning, are excitatory in nature, and lack local STN connectivity. a-**c**, Monosynaptic retrograde RV tracing from *VGLUT2*$^+$ or *PV*$^+$ STN neurons. Images show starter cells in STN (**a**), FISH co-staining of *GFP* with *VGLUT2* or *PV* (**b**), and corresponding PF labeling (**c**, lower magnification image relative to Fig. 2h) ($n = 7$ mice per group). **d**-**e**, Expression of a Cre-dependent hM4Di-mCh virus in STN (**d**), FISH co-staining of *mCh* with *VGLUT2* or *PV* (**e**) in Vglut2-Cre or PV-Cre mice, related to experiments in Fig. 2j, k. **f**, Inhibition of STN *VGLUT2*$^-$ neurons during rotarod using a Cre-Off virus (DO-NpHR-eYFP) injected in STN of Vglut2-Cre mice. *eYFP* mice received a control Cre-Off virus (DO-eYFP) in place of the NpHR virus ($n = 7$ mice per group). FISH co-staining of *VGLUT2* with *eYFP* (used a red fluorophore to visualize the *eYFP* probe). **g**, Inhibition of STN *PV*$^+$ neurons that receive PF inputs during rotarod using an anterograde AAV expressing Cre injected in PF, and a Cre-On/Flp-On virus (COn/FOn-NpHR3.3-eYFP) injected in STN of PV-Flp mice. *eYFP* mice received a control Cre-On/Flp-On virus (COn/FOn-eYFP) in place of the NpHR3.3 virus ($n = 7$ mice per group). FISH co-staining of *PV* with *eYFP* (used a red fluorophore to visualize the *eYFP* probe). **h**-**i**, FISH staining of GFP-labeled *VGLUT2*$^+$ neurons and endogenous *VGLUT2* expression (**h**) or GFP-labeled *PV*$^+$ neurons and endogenous *PV* expression (**i**) showed a high degree of overlap for each of these mouse lines. *GFP* labeling was achieved by injecting a Cre-dependent AAV in STN of Vglut2-Cre or PV-Cre mice. **j**-**k**, Half width (**j**) and spontaneous firing (**k**) measured in *ex vivo* recordings from STN *VGLUT2*$^+$ and *PV*$^+$ neurons. To visualize *VGLUT2*$^+$ and *PV*$^+$ neurons, a Cre-dependent *mCh* virus was injected in STN of Vglut2-Cre or PV-Cre mice (Half width, *VGLUT2*$^+$: $n = 18$ neurons (6, 5, 7), *PV*$^+$: $n = 12$ neurons (4, 4, 4) from 3 mice each; Spontaneous firing, *VGLUT2*$^+$: $n = 9$ neurons (3, 3, 3), *PV*$^+$: $n = 9$ neurons (3, 3, 3) from 3 mice each). **l**, Input resistance (R_{in}), membrane time constant (tau), membrane capacitance (C_m), and action potential amplitude of STN *VGLUT2*$^+$ and *PV*$^+$ neurons. To visualize *VGLUT2*$^+$ and *PV*$^+$ neurons, a Cre-dependent *mCh* virus was injected in STN of Vglut2-Cre or PV-Cre mice (R_{in}, tau, and C_m, *VGLUT2*$^+$: $n = 21$ neurons (8, 8, 5), *PV*$^+$: $n = 13$ neurons (5, 5, 3) from 3 mice each; Amplitude, *VGLUT2*$^+$: $n = 18$ neurons (6, 5, 7), *PV*$^+$: $n = 12$ neurons (4, 4, 4) from 3 mice each). **m**, *VGLUT2*, *PV* FISH staining in wild type STN sections. Plot (right) shows the proportion of *VGLUT2*$^+$ or *VGLUT3*$^+$ neurons among the total number of *PV*$^+$ STN neurons ($n = 5$ *VGLUT2*$^+$, $n = 4$ *VGLUT3*$^+$ mice). **n**, Representative traces of evoked IPSCs ($n = 10$ neurons (3, 4, 3) from 3 mice) and evoked EPSCs ($n = 10$ neurons (2, 4, 4) from 3 mice) recorded in STN neurons during activation of ChR2-eYFP-expressing *PV*$^+$ STN neurons. PV-Cre mice were injected with a Cre-dependent ChR2-eYFP virus in STN. Data are presented as mean ± SEM; $^*P < 0.05$, $^{**}P < 0.01$, $^{***}P < 0.001$. NS, not significant. Two-tailed unpaired *t* test (**c**, **j**-**m**) and two-tailed paired *t* test (**f**, **g**). $P < 0.0001$ (**c**), Cre-Off eYFP $P = 0.001$, Cre-Off NpHR $P = 0.12$ (**f**), eYFP $P = 0.019$, NpHR3.3 $P = 0.85$ (**g**), $P = 0.0012$ (**j**), $P = 0.62$ (**k**), R_{in} $P = 0.14$, Tau $P = 0.11$, C_m $P = 0.26$, Amplitude $P = 0.51$ (**l**), $P = 0.0001$ (**m**).

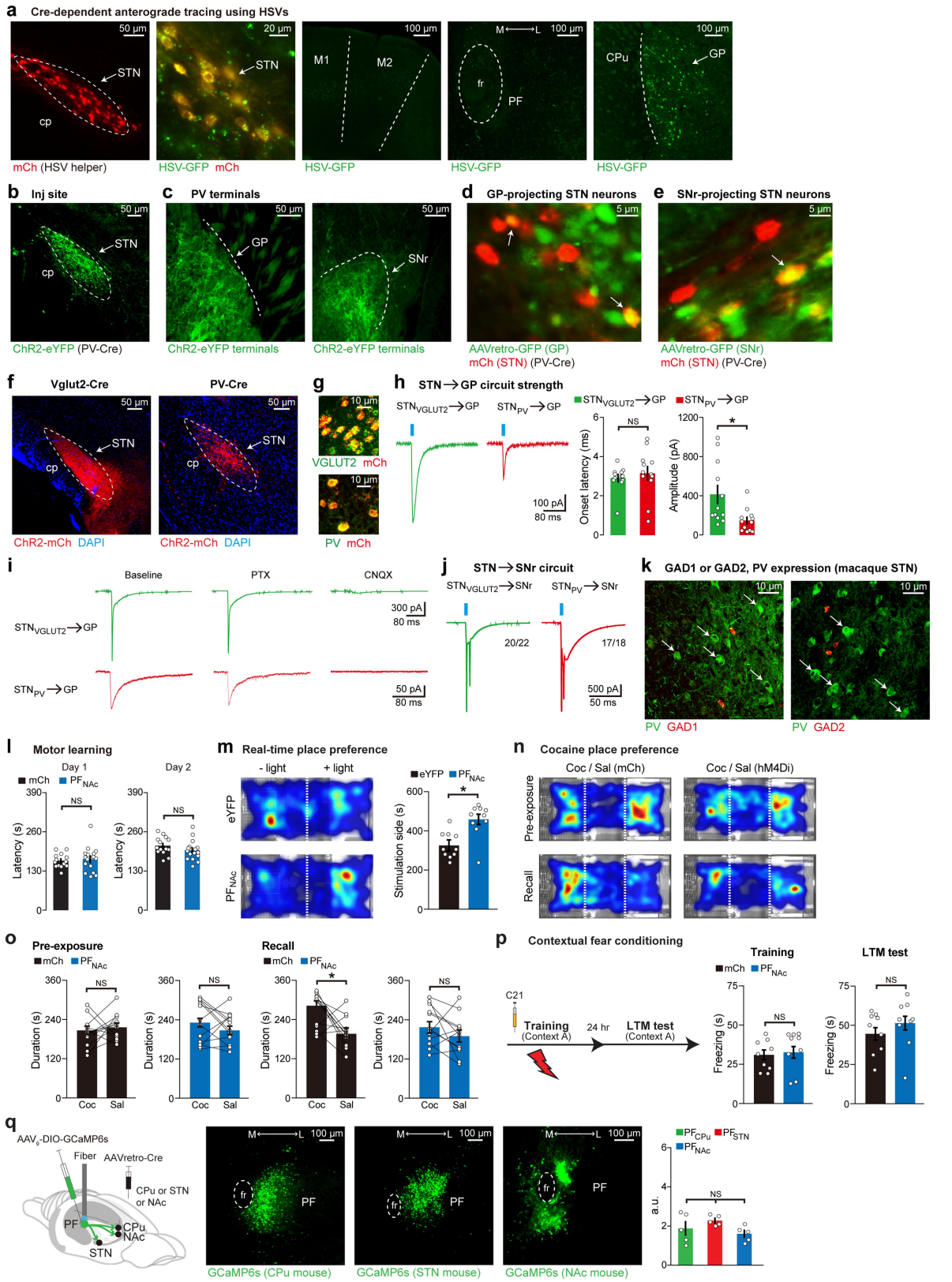

Extended Data Fig. 4 | See next page for caption.

Extended Data Fig. 4 | *PV*$^+$ STN neurons send excitatory projections to GP and SNr, and PF_{NAc} manipulations in motor, positive valence, and negative valence behaviors. a, Monosynaptic HSV anterograde tracing from *PV*$^+$ neurons in STN, using PV-Cre mice. Images show HSV helper cells (red) in STN overlapping with HSV-GFP-expressing cells (green) (i.e., starter cells), lack of labeling in known input brain regions (motor cortex, M1/M2 or PF thalamus) indicating that this virus does not travel retrogradely, and anterograde labeling in GP. **b**-**c**, Cre-dependent ChR2-eYFP virus injection (inj) site of PV-Cre mice (**b**), and representative images showing eYFP$^+$ axonal terminals in GP and SNr (**c**). **d**-**e**, Retrogradely-labeled neurons (green) from GP (**d**) or SNr (**e**) colocalized with *PV*$^+$ neurons in STN. Retrograde labeling was achieved by injecting AAVretro-GFP in GP or SNr. *PV* neurons were labeled by injecting a Cre-dependent *mCh* virus in STN of PV-Cre mice. **f**-**g**, Expression of Cre-dependent ChR2-mCh virus in STN of Vglut2-Cre or PV-Cre mice (**f**), FISH co-staining of *mCh* with *VGLUT2* or *PV* (**g**). DAPI staining (blue). **h**, Representative traces, onset latency, and amplitude of evoked EPSCs recorded in GP neurons during terminal activation of STN *VGLUT2*$^+$ or *PV*$^+$ neurons (STN_{VGLUT2}→GP: $n = 12$ neurons (4, 5, 3), STN_{PV}→GP: $n = 12$ neurons (4, 4, 4) from 3 mice each). **i**, Representative traces of evoked EPSCs in the presence of picrotoxin (PTX) and 6-cyano-7-nitroquinovaline-2,3-dione (CNQX) for the STN_{VGLUT2}→GP and STN_{PV}→GP circuits. **j**, Representative traces of evoked EPSCs recorded in SNr neurons during activation of STN *VGLUT2*$^+$ or *PV*$^+$ neuronal terminals (STN_{VGLUT2}→SNr: $n = 22$ neurons (6, 8, 8), STN_{PV}→SNr: $n = 18$ neurons (6, 6, 6) from 3 mice each). **k**, *GAD1* or *GAD2* FISH with *PV* immunostaining in STN sections of cynomolgus macaques. **l**, C21-induced inhibition of PF_{NAc} neurons during rotarod tests. *mCh* control mice data from Extended Data Fig. 2f ($n = 14$ mCh, $n = 16$ PF_{NAc} mice). **m**, Real-time place preference behavior. NAc-projecting PF neurons were labeled by injecting RVdGL-Cre in NAc and Cre-dependent ChR2-eYFP in PF. Control group received the same injections except with Cre-dependent *eYFP* in PF. Blue light activation was performed at 20 Hz, only in the right side of the chamber (10 mW at patch cord) ($n = 10$ mice per group). **n**-**o**, Cocaine-induced conditioned place preference behavior, heat maps (**n**), quantification (**o**). NAc-projecting PF neurons were labeled by injecting RVdGL-Cre in NAc and Cre-dependent hM4Di-mCh in PF (referred to as hM4Di or PF_{NAc} groups). Control group received the same injections except with Cre-dependent *mCh* in PF (mCh group). Baseline preference in the 3-chamber arena referred to as pre-exposure. After cocaine-induced training was completed (left side for cocaine, right side for saline), recall tests demonstrated conditioned place preference. C21-induced inhibition of PF_{NAc} neurons was performed during the training phase ($n = 12$ mice per group). **p**, Contextual fear conditioning behavior. Mice were prepared similar to panel n. C21-induced inhibition was performed by injecting C21 40 min before the training day, followed by a long-term memory (LTM) test 24 hr later ($n = 9$ mice per group). **q**, Fiber photometry recordings from PF_{CPu}, PF_{STN}, or PF_{NAc} neurons by injecting a retrograde AAV expressing Cre in CPu, STN, or NAc, and Cre-dependent GCaMP6s in PF, followed by fibers placed above PF (left). Representative images (middle). Baseline *in vivo* GCaMP expression level (arbitrary units or a.u.) (right). Data are presented as mean ± SEM; $^*P < 0.05$. NS, not significant. Two-tailed unpaired *t* test (**h**, **l**, **m**, **p**), two-tailed paired *t* test (**d**), and one-way ANOVA followed by Bonferroni post-hoc test (**q**). Onset latency $P = 0.56$, amplitude $P = 0.012$ (**h**), Day 1 $P = 0.69$, Day 2 $P = 0.20$ (**l**), $P = 0.01$ (**m**), Pre-exposure: mCh $P = 0.46$, PF_{NAc} $P = 0.34$, Recall: mCh $P = 0.02$, PF_{NAc} $P = 0.21$ (**o**), Training $P = 0.89$, LTM test $P = 0.38$ (**p**), $F = 2.17$, $P = 0.16$ (**q**).

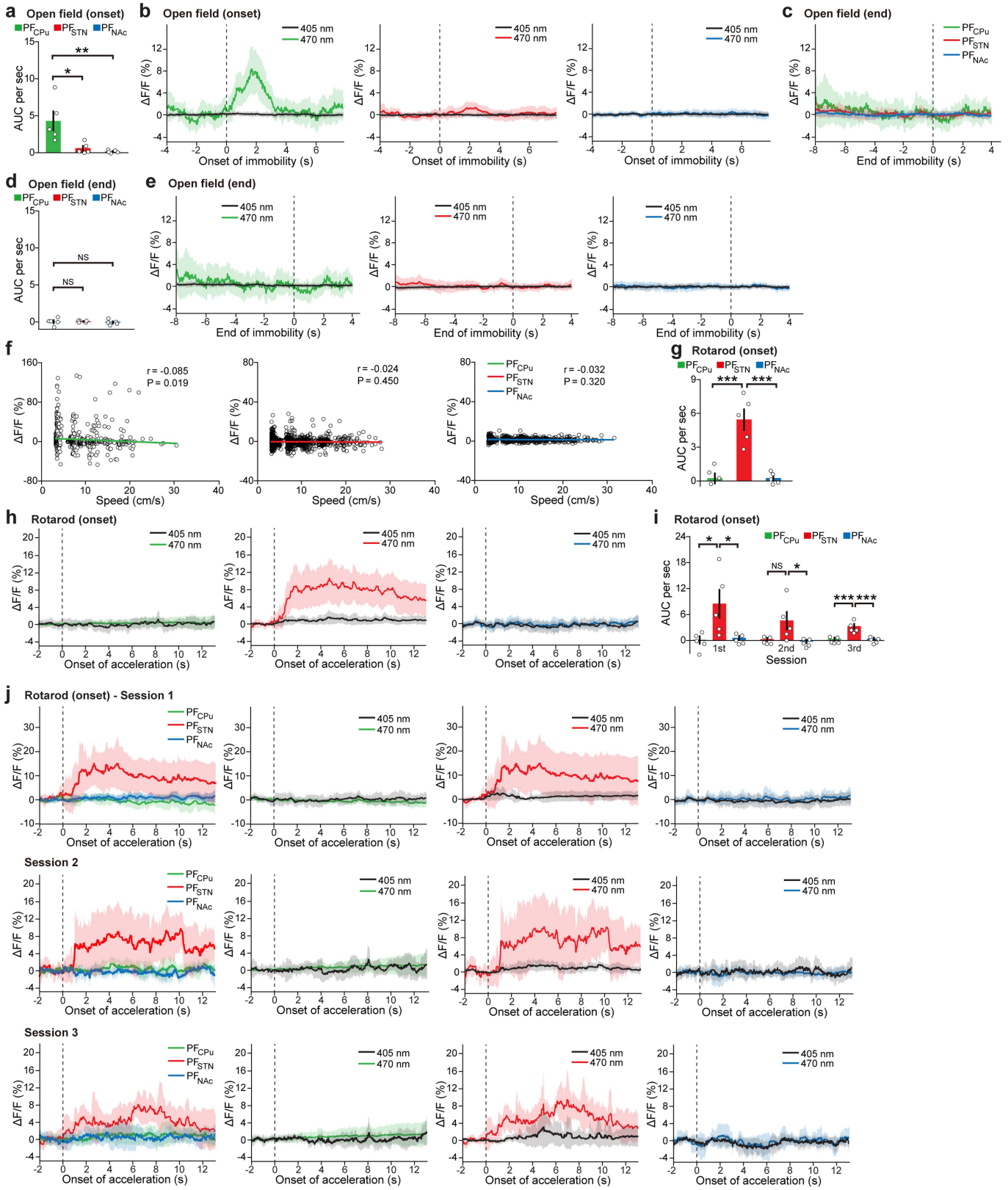

Extended Data Fig. 5 | See next page for caption.

Extended Data Fig. 5 | *In vivo* fiber photometry analyses for open field and rotarod recordings. a-**f**, Area under the curve (AUC) per sec for open field aligned to the onset of immobility (0 to 4 s compared to baseline −4 to 0 s) (**a**), 405 and 470 nm traces for each PF population for open field recordings aligned to the onset of immobility (**b**), averaged fluorescence change aligned to the end of immobility (**c**), AUC per sec for open field aligned to the end of immobility (−4 to 0 s compared to baseline 0 to 4 s) (**d**), 405 and 470 nm traces for each PF population for open field recordings aligned to the end of immobility (**e**), correlation between fluorescence change and mouse speed in the open field (r, correlation coefficient) ($n = 5$ mice per group) (**f**). **g**-**j**, AUC per sec for rotarod aligned to the onset of acceleration (0 to 4 s compared to baseline −2 to 0 s) (**g**), 405 and 470 nm traces for each PF population for rotarod recordings aligned to the onset of acceleration (**h**), AUC per sec for rotarod aligned to the onset of acceleration (0 to 4 s compared to baseline −2 to 0 s) for each individual session (**i**), 405 and 470 nm traces for each PF population for rotarod recordings aligned to the onset of acceleration showing individual session data ($n = 5$ mice per group) (**j**). Data are presented as mean ± SEM; $^{*}P < 0.05$, $^{**}P < 0.01$, $^{***}P < 0.001$. NS, not significant. One-way ANOVA followed by Bonferroni post-hoc test (**a**, **d**, **g**, **i**) and correlation analysis (**f**). $F = 8.83$, $P = 0.004$, PF_{CPu} vs. PF_{STN} $t = 3.42$, PF_{CPu} vs. PF_{NAc} $t = 3.83$ (**a**), $F = 0.168$, $P = 0.84$, PF_{CPu} vs. PF_{STN} $t = 0.19$, PF_{CPu} vs. PF_{NAc} $t = 0.38$ (**d**), $F = 24.49$, $P < 0.0001$, PF_{CPu} vs. PF_{STN} $t = 6.07$, PF_{STN} vs. PF_{NAc} $t = 6.05$ (**g**), 1st: $F = 5.75$, $P = 0.02$, PF_{CPu} vs. PF_{STN} $t = 3.02$, PF_{STN} vs. PF_{NAc} $t = 2.85$, 2nd: $F = 4.816$, $P = 0.03$, PF_{CPu} vs. PF_{STN} $t = 2.54$, PF_{STN} vs. PF_{NAc} $t = 2.82$, 3rd: $F = 17.28$, $P = 0.0003$, PF_{CPu} vs. PF_{STN} $t = 5.13$, PF_{STN} vs. PF_{NAc} $t = 5.05$ (**i**).

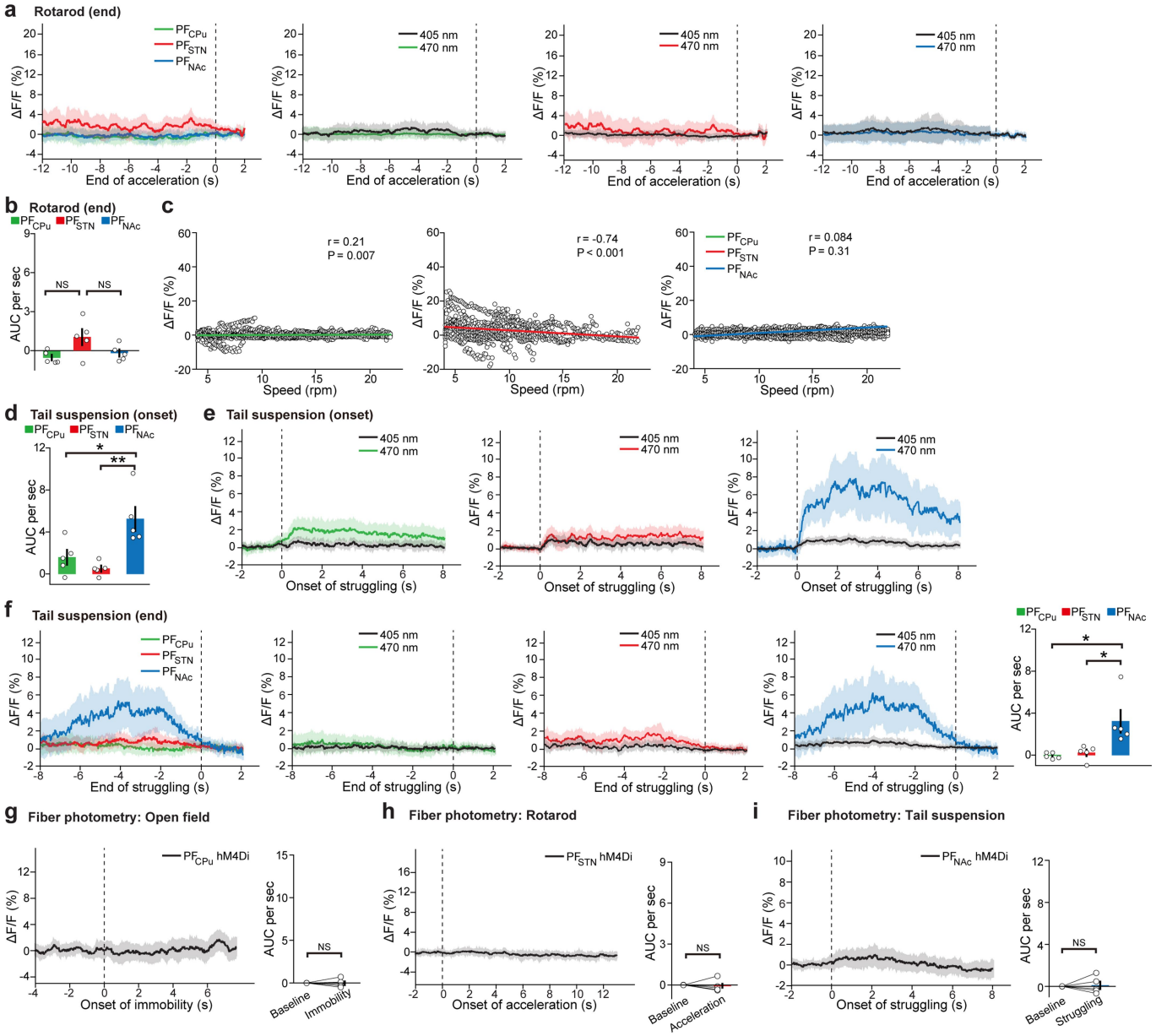

Extended Data Fig. 6 | *In vivo* fiber photometry analyses for the end of the acceleration epoch in rotarod and tail suspension recordings. a-c, Averaged fluorescence change and 405/470 nm traces for each PF population for rotarod recordings aligned to the end of acceleration (**a**), AUC per sec for rotarod aligned to the end of acceleration (−4 to 0 s compared to baseline 0 to 2 s) (**b**), correlation between fluorescence change and mouse speed (computed based on the speed of the rod) in the rotarod test (r, correlation coefficient) ($n = 5$ mice per group) (**c**). **d-f**, AUC per sec for tail suspension aligned to the onset of struggling (0 to 4 s compared to baseline −2 to 0 s) (**d**), 405 and 470 nm traces for each PF population for tail suspension recordings aligned to the onset of struggling (**e**), averaged fluorescence change and 405/470 nm traces aligned to the end of struggling, AUC per sec for tail suspension aligned to the end of struggling (−4 to 0 s compared to baseline 0 to 2 s) ($n = 5$ mice per group) (**f**). **g-i**, Averaged fluorescence change and AUC per sec for PF_{CPu} hM4Di mice during open field (**g**), PF_{STN} hM4Di mice during rotarod (**h**), and PF_{NAc} hM4Di mice during tail suspension ($n = 5$ mice per group) (**i**). PF_{CPu} hM4Di, PF_{STN} hM4Di, and PF_{NAc} hM4Di mice received a retrograde AAV expressing Cre in CPu, STN, or NAc, Cre-dependent GCaMP6s and hM4Di viruses in PF, followed by fibers placed above PF. Data are presented as mean ± SEM; $^{*}P < 0.05$, $^{**}P < 0.01$. NS, not significant. One-way ANOVA followed by Bonferroni post-hoc test (**b**, **d**, **f**) and two-tailed paired *t* test (**g-i**). $F = 3.95$, $P = 0.048$, PF_{CPu} vs. PF_{STN} $t = 2.68$, PF_{STN} vs. PF_{NAc} $t = 2.07$ (**b**), $F = 9.73$, $P = 0.003$, PF_{CPu} vs. PF_{NAc} $t = 3.25$, PF_{STN} vs. PF_{NAc} $t = 4.21$ (**d**), $F = 7.8$, $P = 0.0068$, PF_{CPu} vs. PF_{NAc} $t = 3.563$, PF_{STN} vs. PF_{NAc} $t = 3.258$ (**f**), $P = 0.87$ (**g**), $P = 0.74$ (**h**), $P = 0.8$ (**i**).

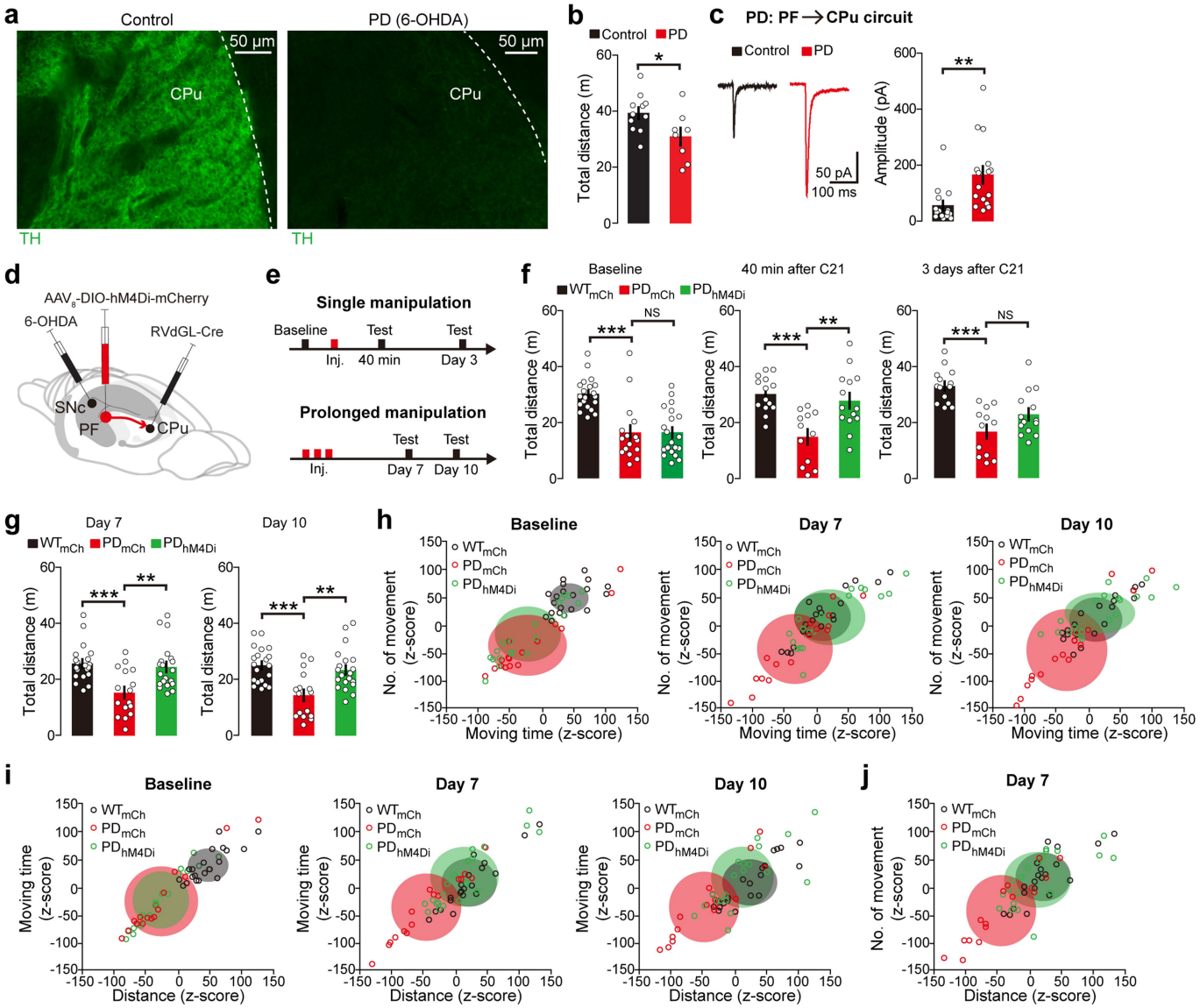

Extended Data Fig. 7 | Prolonged chemogenetic inhibition of PF_{CPu} neurons rescued locomotion in PD model mice up to 10 days later. a, *TH* staining in CPu of saline control (left) or 6-OHDA-injected PD model (right) mice. **b**, Open field test using saline control and PD model mice 30 days after 6-OHDA injections ($n = 11$ saline, $n = 8$ PD model mice). **c**, Representative traces and evoked EPSC amplitudes recorded in CPu neurons receiving PF input from control and PD model mice (Control: $n = 15$ neurons (5, 5, 5), PD: $n = 16$ neurons (5, 6, 5) from 3 mice each). **d**, PF_{CPu} inhibition in PD model mice by injecting a retrograde RVdGL-Cre in CPu, Cre-dependent hM4Di-mCh in PF, and 6-OHDA in SNc. **e-j**, Open arena behavior protocol using two different manipulation strategies starting from 14 days after 6-OHDA injections (**e**). For single manipulation experiments, total distance during a 20-min open arena test was measured prior to the C21 injection (Baseline), or 40 min and 3 days after one C21 injection (Test) (Baseline: $n = 20$ WT_{mCh}, $n = 16$ PD_{mCh}, $n = 20$ PD_{hM4Di} mice; 40 min and 3 days: $n = 14$ WT_{mCh}, $n = 12$ PD_{mCh}, $n = 14$ PD_{hM4Di} mice) (**f**). Saline was injected 40 min before the baseline session. For prolonged manipulation experiments, total distance, number of movements, and moving time (**g-j**) during tests were measured 7 days and 10 days after the 3-day prolonged C21 protocol (Day 7 and Day 10: $n = 20$ WT_{mCh}, $n = 16$ PD_{mCh}, $n = 20$ PD_{hM4Di} mice). In panels **h** and **i**, baseline data plotted from panel **f**. WT_{mCh} mice were injected with a retrograde RVdGL-Cre injected in CPu, Cre-dependent mCh in PF, and saline in SNc. Day 7 data related to Fig. 4b (**j**). Data are presented as mean ± SEM; $^{**}P < 0.01$, $^{***}P < 0.001$. NS, not significant. Two-tailed unpaired *t* test (**b**, **c**), and one-way ANOVA followed by Bonferroni post-hoc test (**f**, **g**). $P = 0.033$ (**b**), $P = 0.004$ (**c**), Baseline: $F = 17.77$, $P < 0.0001$, WT_{mCh} vs. PD_{mCh} $t = 5.26$, PD_{mCh} vs. PD_{hM4Di} $t = 0.006$, 40 min after C21: $F = 10.7$, $P = 0.0002$, WT_{mCh} vs. PD_{mCh} $t = 4.35$, PD_{mCh} vs. PD_{hM4Di} $t = 3.67$, 3 days after C21: $F = 15.35$, $P < 0.0001$, WT_{mCh} vs. PD_{mCh} $t = 5.44$, PD_{mCh} vs. PD_{hM4Di} $t = 2.06$ (**f**), Day 7: $F = 9.46$, $P = 0.0003$, WT_{mCh} vs. PD_{mCh} $t = 4.05$, PD_{mCh} vs. PD_{hM4Di} $t = 3.57$, Day 10: $F = 10.72$, $P = 0.0001$, WT_{mCh} vs. PD_{mCh} $t = 4.37$, PD_{mCh} vs. PD_{hM4Di} $t = 3.69$ (**g**).

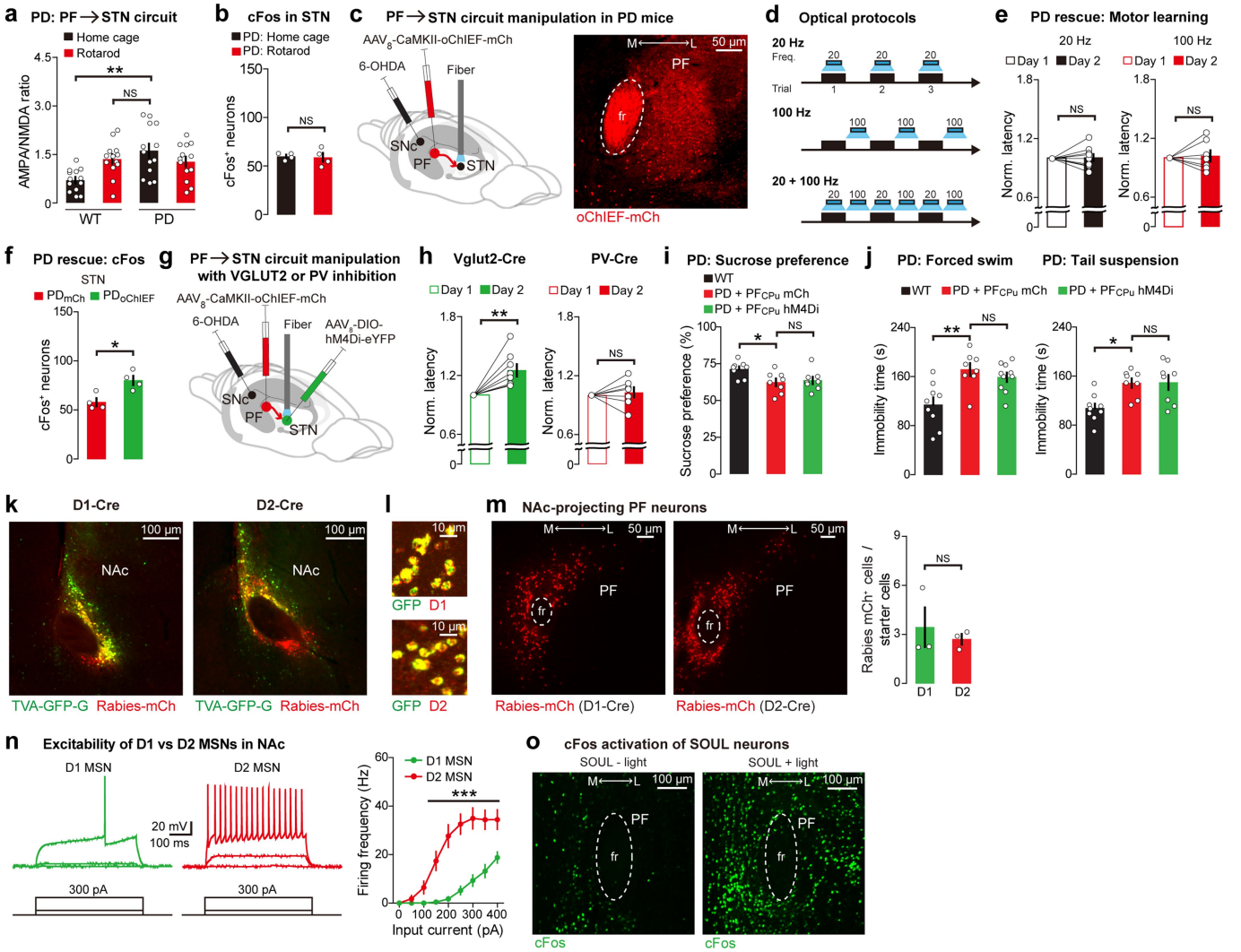

Extended Data Fig. 8 | Strengthening the PF→STN circuit restores motor learning in PD model mice through *PV*$^+$ STN neurons, and PD model mice show depression-like phenotypes. a, AMPA/NMDA ratio recordings of PF→STN circuit from WT and PD model mice in home cage and rotarod conditions (WT data from Fig. 2e, PD data from Fig. 4d). **b**, *cFos* activation of STN neurons using home cage and rotarod PD model mice ($n = 4$ mice per group). **c**, PF→STN circuit manipulation in PD model mice by injecting CaMKII-oChIEF-mCh virus in PF, optic fibers above STN, and 6-OHDA injections in SNc (left). Expression of oChIEF-mCh in PF (right). **d**, Optical protocols including 20 Hz- and 100 Hz-only protocols. 20 Hz blue light was delivered during trials whereas 100 Hz blue light was delivered between trials. **e**, Activation of the PF→STN circuit in PD model mice using the 20 Hz or 100 Hz protocol during rotarod behavior (20 Hz: $n = 9$, 100 Hz: $n = 7$ mice). **f**, STN *cFos* activation in PD model mice ($n = 4$ mice per group) following PF→STN circuit activation with the 20 + 100 Hz protocol during rotarod. Control PD model mice (PD_{mCh}) was prepared similar to the PD_{oChIEF} mice except that a mCh virus was injected in PF. **g**-**h**, PF→STN circuit strengthening with *VGLUT2* or *PV* inhibition in STN during rotarod, using PD model mice. CaMKII-oChIEF-mCh virus was injected in PF, Cre-dependent hM4Di virus in STN, 6-OHDA in SNc, and fibers targeted STN of Vglut2-Cre or PV-Cre mice (**g**). Rotarod behavior ($n = 8$ Vglut2-Cre, $n = 7$ PV-Cre mice) (**h**). **i**-**j**, Sucrose preference ($n = 8$ mice per group) (**i**) and total immobility time in forced swim ($n = 9$ WT, $n = 8$ PD + PF_{CPu} mCh, $n = 10$ PD + PF_{CPu} hM4Di mice) and tail suspension ($n = 9$ WT, $n = 8$ PD + PF_{CPu} mCh, $n = 8$ PD + PF_{CPu} hM4Di mice) tests in PD (**j**). To rule out the possibility that decreased locomotion of PD model mice resulted in their performance in these assays, a retrograde RVdGL-Cre was injected in CPu and Cre-dependent hM4Di-mCh was injected in PF of PD model mice (PD + PF_{CPu} hM4Di group). For WT and PD + PF_{CPu} mCh groups, Cre-dependent mCh was injected in PF in place of the hM4Di virus. C21 was injected 40 min before tests to rescue locomotion deficits in PD model mice by manipulating the PF→CPu circuit. **k**-**m**, Monosynaptic retrograde RV tracing from *D1*$^+$ or *D2*$^+$ NAc neurons. Images show starter cells in NAc (**k**), FISH co-staining of *GFP* with *D1* or *D2* (l), and corresponding PF labeling ($n = 3$ mice per group) (**m**). **n**, Representative traces (left) and current-frequency curves (right) of *ex vivo* recordings from *D2*$^-$ (putative *D1*$^+$) or *D2*$^+$ MSNs in NAc using D2-eGFP mice (*D1*: $n = 20$ neurons (6, 7, 7), *D2*: $n = 16$ neurons (6, 4, 6) from 3 mice each). **o**, Representative images of PF sections stained with *cFos* from mice expressing SOUL in PF neurons, including a no light group (SOUL - light) and a 5 min light activated group (SOUL + light) in the home cage. Data are presented as mean ± SEM; $^*P < 0.05$, $^{**}P < 0.01$, $^{***}P < 0.001$. NS, not significant. One-way ANOVA followed by Bonferroni post-hoc test (**a**), two-tailed unpaired *t* test (**b**, **f**, **m**), two-tailed paired *t* test (**e**, **h**), and two-way ANOVA with repeated measures followed by Bonferroni post-hoc test (**n**). $F = 5.81$, $P = 0.0018$, Home cage WT vs. home cage PD $t = 4.04$, Rotarod WT vs. Home cage PD $t = 1.15$ (**a**), $P = 0.84$ (**b**), 20 Hz $P = 0.87$, 100 Hz $P = 0.72$ (**e**), $P = 0.012$ (f), Vglut2-Cre $P = 0.005$, PV-Cre $P = 0.59$ (**h**), $F = 4.28$, $P = 0.028$, WT vs. PD + PF_{CPu} mCh $t = 2.71$, PD + PF_{CPu} mCh vs. PD + PF_{CPu} hM4Di $t = 0.39$ (**i**), Forced swim: $F = 8.92$, $P = 0.0013$, WT vs. PD + PF_{CPu} mCh $t = 3.95$, PD + PF_{CPu} mCh vs. PD + PF_{CPu} hM4Di $t = 0.88$, Tail suspension: $F = 7.18$, $P = 0.004$, WT vs. PD + PF_{CPu} mCh $t = 3.21$, PD + PF_{CPu} mCh vs. PD + PF_{CPu} hM4Di $t = 0.07$ (**j**), $P = 0.58$ (**m**), $F = 38.34$, DFn = 1, DFd = 272, $P < 0.0001$ (**n**).

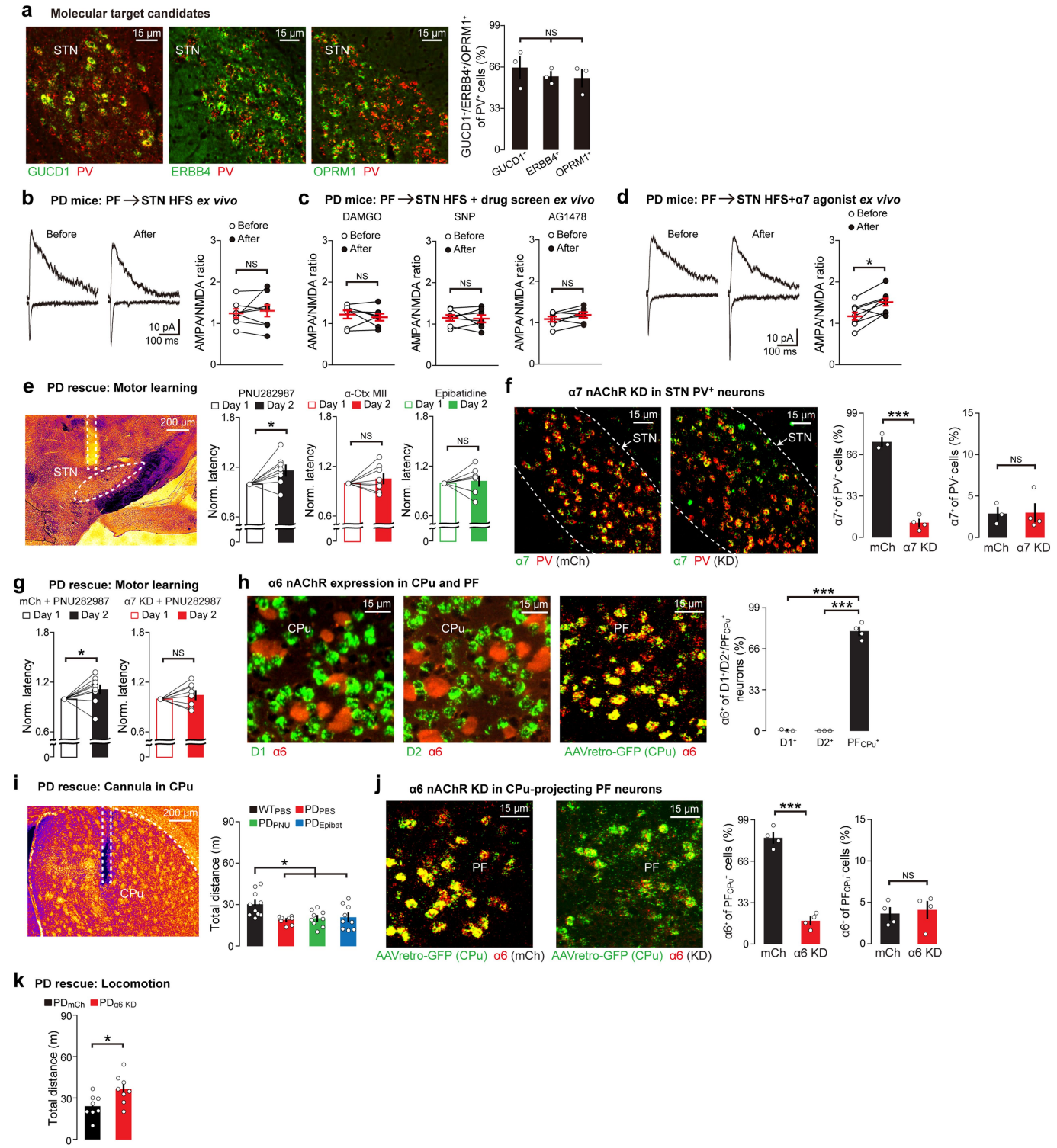

Extended Data Fig. 9 | See next page for caption.

Extended Data Fig. 9 | Testing molecular target candidates in the PF→STN and PF→CPu circuits. a, *GUCD1* (guanylyl cyclase gene, the *NO* receptor), *ERBB4*, and *OPRM1* (μ-opioid receptor gene) FISH staining with *PV* in STN sections. 65.6% of all *PV*$^+$ neurons were *GUCD1*$^+$, 58.5% of all *PV*$^+$ neurons were *ERBB4*$^+$, 57.2% of all *PV*$^+$ neurons were *OPRM1*$^+$ ($n = 3$ mice per group). **b**, AMPA/NMDA ratio recordings of the PF→STN circuit, specifically *PV*$^+$ STN neurons, before and after optical high frequency stimulation (HFS) in PD model mice ($n = 8$ neurons (2, 3, 3) from 3 mice). oChIEF-mCh virus was injected in PF, Cre-dependent eYFP virus in STN, and 6-OHDA in SNc of PV-Cre mice. **c**-**d**, With DAMGO (μ-opioid receptor agonist), SNP (*NO* receptor agonist), AG1478 (*ERBB4* receptor antagonist) (**c**) or PNU282987 (*α7* agonist) (**d**) bath application, AMPA/NMDA ratio recordings of the PF→STN$_{PV}$ circuit before and after optical HFS in PD model mice (DAMGO: $n = 7$ neurons (2, 2, 3), SNP: $n = 7$ neurons (3, 2, 2), AG1478: $n = 7$ neurons (2, 2, 3), PNU282987: $n = 8$ neurons (2, 3, 3) from 3 mice each). oChIEF-mCh virus was injected in PF, Cre-dependent eYFP virus in STN, and 6-OHDA in SNc of PV-Cre mice. **e**, Local bilateral infusion of PNU282987, α-Ctx MII, or epibatidine into STN of PD model mice prior to rotarod behavior assays ($n = 8$ mice per group). **f**, *α7* nAChRs FISH staining with *PV* in STN sections from mCh and KD mice, *α7* in *PV*$^+$ cells is decreased by 84% in KD mice as compared to mCh controls ($n = 3$ mCh, $n = 4$ *α7* KD mice). **g**, Activating *α7* nAChRs without (left) or with (right) *α7* KD from *PV*$^+$ STN neurons during rotarod, using PD model mice ($n = 10$ mCh, $n = 8$ *α7* KD mice). PD$_{\alpha7\,KD}$ received a Cre-dependent Cas9 and gRNA viruses (for knockdown of *α7* nAChRs) and cannula implants above STN, and 6-OHDA in SNc of PV-Cre mice. **h**, *α6* nAChRs FISH staining with *D1* or *D2* in mouse CPu sections and with PF$_{CPu}$ neurons in mouse PF sections. PF$_{CPu}$ neurons were labeled by injecting AAVretro-GFP in CPu ($n = 3$ *D1*$^+$, $n = 3$ *D2*$^+$, $n = 4$ PF$_{CPu}^+$ mice). **i**, Representative cannula implant targeting CPu for local infusion experiments (left), local bilateral infusion of PBS, PNU282987, or epibatidine into CPu of PD model mice and infusion of PBS into CPu of WT mice prior to open field behavior ($n = 10$ WT$_{PBS}$, 9 PD$_{PBS}$, 9 PD$_{PNU}$, 9 PD$_{Epibat}$ mice) (right). WT$_{PBS}$ and PD$_{PBS}$ data from Fig. 5e. **j**, *α6* nAChRs FISH staining with PF$_{CPu}$ neurons in PF sections from mCh and KD mice, *α6* in PF$_{CPu}^+$ cells is decreased by 78% in KD mice as compared to mCh controls ($n = 4$ mice per group). **k**, Total distance mice travelled in the open field after KD of *α6* in PF$_{CPu}$ neurons of PD model mice ($n = 8$ mice per group). PD$_{\alpha6\,KD}$ received a retrograde RVdGL-Cre in CPu, Cre-dependent Cas9 and gRNA viruses (for knockdown of *α6* nAChRs) in PF$_{CPu}$ neurons, and 6-OHDA in SNc. Data are presented as mean ± SEM; $^*P < 0.05$, $^{***}P < 0.001$. NS, not significant. One-way ANOVA followed by Bonferroni post-hoc test (**a**, **h**, **i**), two-tailed paired *t* test (**b**-**e**, **g**), and two-tailed unpaired *t* test (**f**, **j**, **k**). $F = 0.45$, $P = 0.13$ (**a**), $P = 0.60$ (**b**), DAMGO $P = 0.48$, SNP $P = 0.82$, AG1478 $P = 0.12$ (**c**), $P = 0.011$ (**d**), PNU282987 $P = 0.034$, α-Ctx MII $P = 0.34$, Epibatidine $P = 0.66$ (**e**), $P < 0.0001$ (**f**), mCh + PNU282987 $P = 0.04$, *α7* KD + PNU282987 $P = 0.37$ (**g**), $F = 456.9$, $P < 0.0001$, *D1*$^+$ vs. PF$_{CPu}^+$ $t = 25.49$, *D2*$^+$ vs. PF$_{CPu}^+$ $t = 25.6$ (**h**), $F = 5.16$, $P = 0.0049$, WT$_{PBS}$ vs. PD$_{PBS}$ $t = 3.45$, WT$_{PBS}$ vs. PD$_{PNU}$ $t = 3.09$, WT$_{PBS}$ vs. PD$_{Epibat}$ $t = 2.86$ (**i**), $P < 0.0001$ (**j**), $P = 0.02$ (**k**).

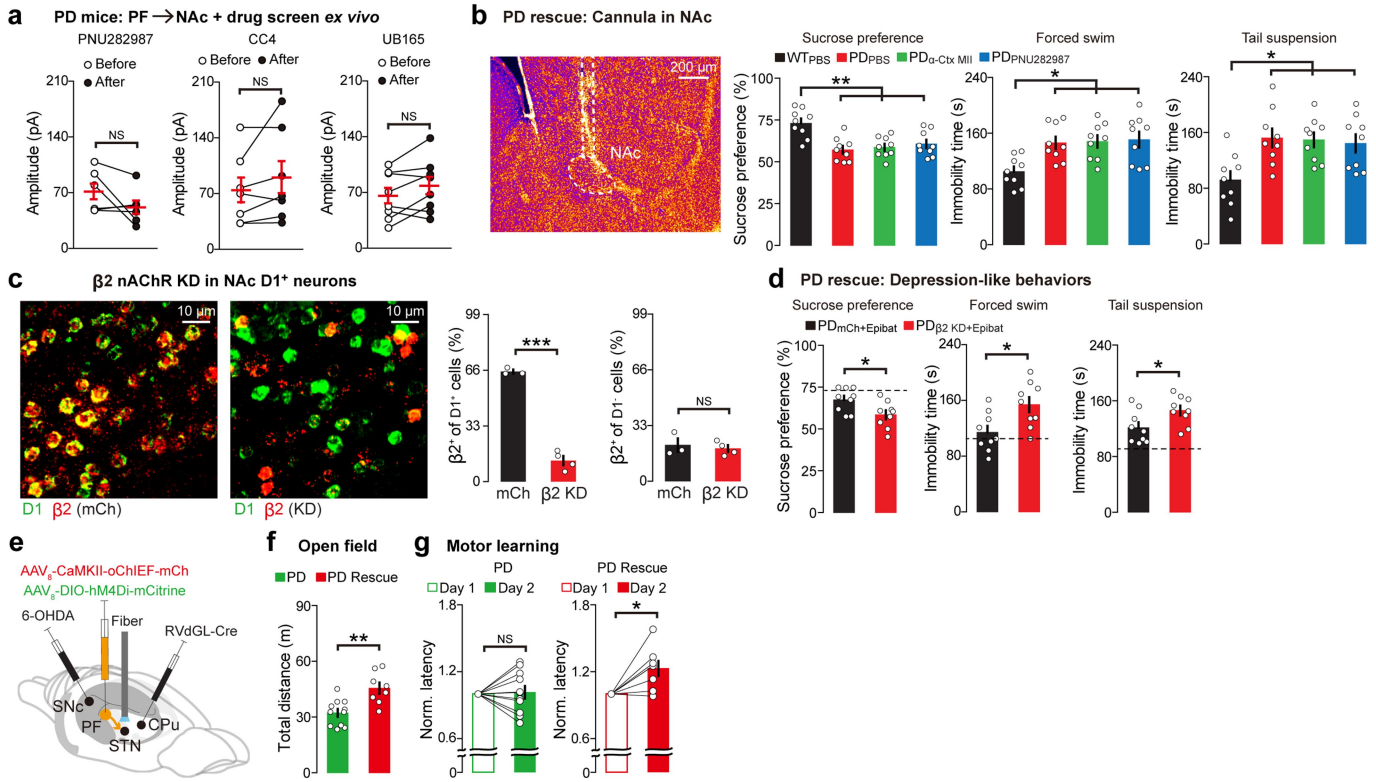

Extended Data Fig. 10 | Testing molecular target candidates in the PF→NAc circuit, and rescue of motor phenotypes in the same mice using PF_{CPu} cell body and PF→STN circuit manipulations *in vivo*. **a**, Before and after bath application of PNU282987 (*α7* agonist), CC4 (*α6* agonist), and UB165 (*α3* agonist), evoked EPSCs were recorded from *D1* MSNs in NAc of PD model mice. oChIEF-mCh virus was injected in PF and 6-OHDA in SNc of D2-eGFP mice (PNU282987: $n = 6$ neurons (1, 2, 1, 1, 1), CC4: $n = 7$ neurons (1, 2, 1, 1, 2), UB165: $n = 8$ neurons (2, 2, 1, 2, 1) from 5 mice each). **b**, Representative cannula implant targeting NAc for local infusion experiments (left), local bilateral infusion of PBS, α-Ctx MII, or PNU282987 into NAc of PD model mice and infusion of PBS into NAc of WT mice prior to depression-like behavior tests ($n = 9$ mice per group) (right). WT_{PBS} and PD_{PBS} data from Fig. 5h. **c**, *β2* nAChRs FISH staining with *D1* in NAc sections from mCh and KD mice, *β2* in $D1^+$ cells is decreased by 80% in KD mice as compared to mCh controls ($n = 3$ mCh, $n = 4$ *β2* KD mice). **d**, Activating *β2* nAChRs without ($PD_{mCh+Epibat}$) or with ($PD_{β2\,KD+Epibat}$) *β2* KD from $D1^+$ NAc neurons during depression-like behaviors, using PD model mice ($n = 9$ mice per group). Dashed line indicates WT level from Fig. 5h. $PD_{β2\,KD}$ received a Cre-dependent Cas9 and gRNA viruses (for knockdown of *β2* nAChRs), cannula implants in NAc, and 6-OHDA in SNc of D1-Cre mice. **e**, A retrograde RVdGL-Cre was injected in CPu, Cre-dependent hM4Di-mCitrine (for PF_{CPu} labeling), and CaMKII-oChIEF-mCh (for STN terminal manipulations) in PF, optic fibers targeting STN, and 6-OHDA injected in SNc. **f**, Total distance in the open field was measured 40 min after C21 injections. PD model mice that received 6-OHDA injections in SNc without any subsequent PF manipulation was the baseline group (labeled PD). PD model mice with PF_{CPu} manipulations are referred to as PD Rescue ($n = 11$ PD, $n = 8$ PD Rescue mice). **g**, Rotarod tests were performed after the open field paradigm. For rotarod, PF→STN circuit strengthening using our optical LTP protocol (20 + 100 Hz) was performed ($n = 11$ PD, $n = 8$ PD Rescue mice). Data are presented as mean ± SEM; $^*P < 0.05$, $^{**}P < 0.01$, $^{***}P < 0.001$. NS, not significant. Two-tailed paired *t* test (**a**, **g**), one-way ANOVA followed by Bonferroni post-hoc test (**b**), and two-tailed unpaired *t* test (**c**, **d**, f). PNU282987 $P = 0.14$, CC4 $P = 0.17$, UB165 $P = 0.10$ (**a**), Sucrose preference: $F = 8.71$, $P = 0.0002$, WT_{PBS} vs. PD_{PBS} $t = 4.57$, WT_{PBS} vs. $PD_{α\text{-}Ctx\,MII}$ $t = 4.14$, WT_{PBS} vs. $PD_{PNU282987}$ $t = 3.57$, Forced swim: $F = 5.59$, $P = 0.0034$, WT_{PBS} vs. PD_{PBS} $t = 3.16$, WT_{PBS} vs. $PD_{α\text{-}Ctx\,MII}$ $t = 3.32$, WT_{PBS} vs. $PD_{PNU282987}$ $t = 3.52$, Tail suspension: $F = 5.32$, $P = 0.0044$, WT_{PBS} vs. PD_{PBS} $t = 3.44$, WT_{PBS} vs. $PD_{α\text{-}Ctx\,MII}$ $t = 3.28$, WT_{PBS} vs. $PD_{PNU282987}$ $t = 2.99$ (**b**), $P < 0.0001$ (**c**), Sucrose preference $P = 0.022$, Forced swim $P = 0.012$, Tail suspension $P = 0.029$ (**d**), $P = 0.0017$ (**f**), PD $P = 0.78$, PD Rescue $P = 0.011$ (**g**).

nature research

Corresponding author(s): Feng G, Zhang Y, Roy DS

Last updated by author(s): Mar 30, 2022

Reporting Summary

Nature Research wishes to improve the reproducibility of the work that we publish. This form provides structure for consistency and transparency in reporting. For further information on Nature Research policies, see our Editorial Policies and the Editorial Policy Checklist.

Statistics

For all statistical analyses, confirm that the following items are present in the figure legend, table legend, main text, or Methods section.

n/a	Confirmed	
☐	☒	The exact sample size (*n*) for each experimental group/condition, given as a discrete number and unit of measurement
☐	☒	A statement on whether measurements were taken from distinct samples or whether the same sample was measured repeatedly
☐	☒	The statistical test(s) used AND whether they are one- or two-sided *Only common tests should be described solely by name; describe more complex techniques in the Methods section.*
☒	☐	A description of all covariates tested
☐	☒	A description of any assumptions or corrections, such as tests of normality and adjustment for multiple comparisons
☐	☒	A full description of the statistical parameters including central tendency (e.g. means) or other basic estimates (e.g. regression coefficient) AND variation (e.g. standard deviation) or associated estimates of uncertainty (e.g. confidence intervals)
☐	☒	For null hypothesis testing, the test statistic (e.g. *F*, *t*, *r*) with confidence intervals, effect sizes, degrees of freedom and *P* value noted *Give P values as exact values whenever suitable.*
☒	☐	For Bayesian analysis, information on the choice of priors and Markov chain Monte Carlo settings
☒	☐	For hierarchical and complex designs, identification of the appropriate level for tests and full reporting of outcomes
☒	☐	Estimates of effect sizes (e.g. Cohen's *d*, Pearson's *r*), indicating how they were calculated

Our web collection on statistics for biologists contains articles on many of the points above.

Software and code

Policy information about availability of computer code

Data collection	Some behavioral data were collected using the Ethovision Noldus Observer software, ex vivo electrophysiology data were collected using the Clampex 10.7 software, and fiber photometry data were collected using the InperStudio 3.1.1 software.
Data analysis	Prism 6 and Microsoft Excel with Statplus plug-in were used for statistical analysis. InperDataProcess 3.1.1 software was used to analyze fiber photometry data. ANY-maze 6.35 was used to analyze animals' speed in the open field test.

For manuscripts utilizing custom algorithms or software that are central to the research but not yet described in published literature, software must be made available to editors and reviewers. We strongly encourage code deposition in a community repository (e.g. GitHub). See the Nature Research guidelines for submitting code & software for further information.

Data

Policy information about availability of data

All manuscripts must include a data availability statement. This statement should provide the following information, where applicable:

- Accession codes, unique identifiers, or web links for publicly available datasets
- A list of figures that have associated raw data
- A description of any restrictions on data availability

All figures in which statistical comparisons are indicated in the legend and/or methods include individual biological data points reported for each main and extended data figure panel along with P values. For the entire manuscript, a source data file has been provided. Reagents are available from the corresponding authors upon reasonable request.

Field-specific reporting

Please select the one below that is the best fit for your research. If you are not sure, read the appropriate sections before making your selection.

☒ Life sciences ☐ Behavioural & social sciences ☐ Ecological, evolutionary & environmental sciences

For a reference copy of the document with all sections, see nature.com/documents/nr-reporting-summary-flat.pdf

Life sciences study design

All studies must disclose on these points even when the disclosure is negative.

Sample size	No statistical calculations were used to pre-determine sample size, but our reported sample sizes for electrophysiology, cell counting, and behavior are comparable to those found in previous publications (e.g., Hong et al., Cell 2014; Roy et al., Cell 2017). This is stated in the Methods section, under the 'Statistics and reproducibility' subheading.
Data exclusions	For all behavioral data points that required virus-injected mice, we pre-established a criteria that only mice with viruses localized to the intended target brain regions were included for summary data analyses. This is in agreement with other publications in this field.
Replication	All experiments were performed in at least two separate batches to confirm that the observed phenotypes in any one batch can be replicated. These attempts were successful.
Randomization	Randomization of animals and groups were applied for all cell counting, physiology, and behavioral experiments in this study.
Blinding	Trained researchers were blind to the animal details and group allocation for cell counting, physiology, and behavioral data collection and analyses.

Reporting for specific materials, systems and methods

We require information from authors about some types of materials, experimental systems and methods used in many studies. Here, indicate whether each material, system or method listed is relevant to your study. If you are not sure if a list item applies to your research, read the appropriate section before selecting a response.

Materials & experimental systems

n/a	Involved in the study
☐	☒ Antibodies
☒	☐ Eukaryotic cell lines
☒	☐ Palaeontology and archaeology
☐	☒ Animals and other organisms
☒	☐ Human research participants
☒	☐ Clinical data
☒	☐ Dual use research of concern

Methods

n/a	Involved in the study
☒	☐ ChIP-seq
☒	☐ Flow cytometry
☒	☐ MRI-based neuroimaging

Antibodies

Antibodies used	For mouse experiments: Chicken anti-GFP (Life Technologies, A10262), anti-chicken Alexa-488 (Life Technologies, A11039), rabbit anti-RFP (Rockland, 600-401-379), anti-rabbit Alexa-555 (Life Technologies, A27039), mouse anti-NeuN (Millipore, MAB377, clone A60), anti-mouse Alexa-555 (Life Technologies, A28180), mouse anti-TH (Immunostar, 22941), anti-mouse Alexa-488 (Life Technologies, A28175),rabbit anti-cFos (Cell Signaling Technology, MAB2250, clone 9F6) and anti-rabbit Alexa-633 (Life Technologies, A21070). For macaque experiments: rabbit anti-RFP (Rockland, 600-401-379), mouse anti-PV (Swant, 235), anti-rabbit Alexa-594 (Thermo Fisher, A32754), anti-mouse Alexa-488 (Thermo Fisher, A21202), and peroxidase (POD)-conjugated anti-DIG antibodies (Roche, 1207733910).
Validation	We selected antibodies that were validated by the manufacturer and in previous publications. For each antibody staining, we made sure that the expression pattern matched what would be expected based on such validation information. Chicken anti-GFP has been validated by Thermo Fisher for immunostaining as well as by 173 publications as mentioned on their website, rabbit anti-RFP was previously validated by us (Roy et al., Neuron 2021), mouse anti-NeuN is routinely evaluated for immunostaining on brain tissue as mentioned on the Millipore website, mouse anti-TH was validated for immunostaining using rodent brain tissue as mentioned on the Immunostar website, rabbit anti-cFos has been validated by Cell Signaling for immunostaining as well as by 57 publications as mentioned on their website, and mouse anti-PV has been validated by Swant using knockout mice.

Animals and other organisms

Policy information about studies involving animals; ARRIVE guidelines recommended for reporting animal research

Laboratory animals	For mice: C57BL/6J wild type (Jackson Labs), Vglut2-Cre (Jackson Labs, Stock No. 028863), PV-Cre (Jackson Labs, Stock No. 017320), D2-eGFP (Jackson Labs, Stock No. 030255), PV-Flp (Stock No. 022730), and D1-Cre (Jackson Labs, Stock No. 030329). D2-Cre (i.e., Drd2-Cre) mice were imported from the GENSAT Project at Rockefeller University. Male mice at 9-20 weeks of age were used for all experiments. All mice were housed in a 7 am-7pm light on-off cycle facility with a temperature of 18-23 degrees C and humidity maintained between 40-60%. For macaques: Cynomolgus monkeys (Macaca fascicularis), males, 2-3 years old, 2.0-2.3 kg weight were used.
Wild animals	This study did not include any wild animals.
Field-collected samples	This study did not involve samples collected from the field.
Ethics oversight	For mouse research, all experimental procedures were conducted in accordance with the U.S. National Institutes of Health (NIH) guidelines and the Massachusetts Institute of Technology Department of Comparative Medicine and Committee of Animal Care. For macaque research, all guidelines followed the Association for Assessment and Accreditation of Laboratory Animal Care (AAALAC).

Note that full information on the approval of the study protocol must also be provided in the manuscript.